Broadband self-pulsating sources based on nonlinear effects

Thibault North

Department of Electrical & Computer Engineering
McGill University
Montréal, Canada

April 2014

A thesis report submitted to McGill University in partial fullfillment of the requirements for the degree of Doctor of Philosophy.

Contents

List of Figures

Acronyms

2R reshaping and reamplification.

APM additive pulse mode-locking.

ASE amplified spontaneous emission.

BER bit error ratio.

BPF band-pass filter.

CPM colliding pulse mode-locking.

CPU central processing unit.

CSM cascaded second-order mode-locking.

CW continuous-wave.

DM dispersion-managed.

EDFA erbium-doped fiber amplifier.

FBG fiber Bragg-grating.

FFT fast Fourier transform.

FROG frequency resolved optical gating.

FSR free spectral range.

FWHM full width at half maximum.

FWM four-wave mixing.

GNLSE generalized nonlinear Schrödinger equation.

GPGPU general-purpose processing on graphics processing units.

GPU graphics processing unit.

GUI graphical user interface.

GVD group velocity dispersion.

HDF hierarchical data format.

HNLF highly nonlinear fiber.

KLM Kerr lens mode-locking.

LASER light amplification by stimulated emission of radiation.

LIDAR light radar.

MASER microwave amplification by stimulated emission of radiation.

MI modulation instability.

MIR mid-infrared.

NALM nonlinear amplifying loop mirror.

NLP noise-like pulse.

NLSE nonlinear Schrödinger equation.

NOLM nonlinear optical loop mirror.

NPR nonlinear polarization rotation.

NWC nonlinear wavelength converter.

OCR output coupling ratio.

OCT optical coherence tomography.

OSA optical spectrum analyser.

PB pulse-buffering.

PBS polarization beam-splitter.

PC polarization controller.

PD photodiode.

PM polarization maintening.

PMT photo-multiplier tube.

PSD power spectral density.

QPS quadratic polarization switching.

RK4IP Runge-Kutta in the interaction picture.

RP Raman pump.

SBS stimulated Brillouin scattering.

SC supercontinuum.

SHG second harmonic generation.

SMF single-mode fiber.

SNR signal over noise ratio.

SP self-pulsating.

SPM self-phase modulation.

SPM-OF SPM spectral broadening and offset filtering.

SPM-SSFS self-phase modulation and offset filtering.

SRS stimulated Raman scattering.

SS self-steepening.

SSFS soliton self-frequency shift.

TPA two-photon absorption.

XPM cross-phase modulation.

ZDW zero-dispersion wavelength.

Abstract

In this thesis, three architectures of self-pulsating erbium laser sources are studied. Through experimental and numerical investigations, the generation of ultrashort and broadband pulses is enabled. In a first phase, a numerical analysis assesses the pulse ignition and steady-state operation of self-pulsating sources composed of self-phase modulation spectral broadening and offset filtering regenerators in closed loop. An experimental setup results from the conclusions of this analysis, and a multiwavelength source generating aperiodic light pulses in the range of the picosecond is presented. In a second phase, a new kind of self-pulsating source based on optical regeneration as well as soliton self-frequency shift is introduced. Via a numerical analysis as well as direct measurements, the role of modulation instability in the generation of femtosecond pulses is highlighted. This laser emits bursts of stochastic pulses at the repetition rate of the cavity, and results on the average in a flat supercontinuum, spreading beyond 1900 nm. Finally, the emission of pulses in the noiselike regime is studied in two different cavities. Via nonlinear polarization rotation, pulses spreading over tens of nanometers are generated. By means of stimulated Raman scattering, the production of noise pulses is demonstrated in the U-band (1625 nm to 1675 nm) and beyond. The bandwidth of such pulses spreads over 84 nm, from 1616 nm to 1700 nm. These three sources find applications in low-coherence interferometry for imagery, or the characterization of components. LIDAR applications for aerosols or distance measurements, as well as spectroscopy for the detection of chemicals are enabled by such lasers.

Résumé

Dans cette thèse, trois architectures de sources laser erbium auto-pulsantes et large bande sont étudiées. Au travers de ces architectures simulées et réalisées expérimentalement, la génération d'impulsions ultra courtes et large bande est rendue possible. Dans un premier temps, une analyse numérique s'intéresse au démarrage et au fonctionnement de sources auto-pulsantes composées de régénérateurs à étalement spectral par auto-modulation de phase et filtrage décalé, dans une configuration en boucle fermée. Un montage expérimental découle des conclusions de ces simulations, et une source multi-longueurs d'onde générant des impulsions apériodiques de l'ordre de la picoseconde est présentée. Dans un second temps, une nouvelle sorte de source auto-pulsante basée sur la régénération optique ainsi que l'auto-décalage fréquentiel de soliton est présentée. Par une analyse numérique ainsi que des mesures directes, le rôle de l'instabilité de modulation dans la génération des impulsions femtosecondes est mis en évidence. Ce laser émet des séquences d'impulsions stochastiques au taux de répétition de la cavité, et dispose en moyenne d'un continuum plat s'étendant au delà de 1900 nm. Finalement, l'émission d'impulsions en mode "noiselike" est étudié au travers de deux cavités. Via la rotation nonlinéaire de polarisation, des impulsions s'étendant sur plusieurs dizaines de nanomètres sont générées. Grâce à l'effet Raman stimulé, la production d'impulsions de bruit dans la bande U (1625 nm – 1675 nm) et au delà est démontrée. La bande passante de ces dernières peut s'étendre sur 84 nm, entre 1616 nm et 1700 nm. Ces trois sources trouvent des applications en interférométrie à faible cohérence pour l'imagerie ou la caractérisation de composants, pour l'estimation de distances ou aérosols dans les applications LIDAR, ainsi que pour la détection d'éléments chimiques.

Acknowledgements

I would like to express my gratitude to those who made this work possible. Foremost, I wish to thank Professor Rochette for his extensive guidance, kindness and support throughout this research. Many thanks for letting me pursue graduate studies in the Photonics System Group and giving me time, even before that, to answer questions over e-mail and phone calls: I learned a lot about nonlinear optics out of these communications, in which you were able to transmit your enthusiasm about the field.

Many thanks also go to the examiners of this thesis, Professor Michel Piché and Professor Odile Liboiron-Ladouceur for their interesting and extensive comments on the manuscript, ranging from typos to suggestions for future work. I am grateful to the members of my research committee, Professor Lawrence Chen and Professor Vamsy Chodavarapu for their time and comments during these three years.

I would also like to thank my colleagues from whom I had the pleasure to learn. In particular, I thanks Alaa Al-kadry for insightful discussions on nonlinear effects including supercontinuum generation, soliton self-frequency shift, etc. I thank Chams Baker, Raja Ahmad, and Ali Salehiomran for assisting me in my experiments by pre-tapering chalcogenide fibers, introducing me to the lab facilities in the beginning of this thesis, or providing pointers and comments on written material. Thanks to Derek Colley for his time reviewing the written manuscript, and for so many conversations and time in front of a game of chess. Thanks also go to my colleagues Mathieu Chagnon, Mina Spasojevic, Sandrine Filion Côté, and Kishor Ramaswamy for interesting discussions, occasionally related to optics, as well as unforgettable lunch and coffee breaks. I wish this could continue, but fear that there is no script for that.

Likewise, I wish to thank Martin Gorjan for the time spent in the lab and in the office, struggling with thulium-doped fibers or discussing their behavior; there was much rejoicing and geek references. Talking about that, I acknowledge the contribution of Philippe Moret, for so many remote discussions including hints and ideas about computer engineering, the life of a PhD student, among other essential topics.

Furthermore, I would like to express my gratitude to Professor Michel Kocher and Professor Stéphane Bourquin, former supervisors, for their support, encouragements and flexibility during my undergraduate and graduate studies. Without your help, this work would not have been possible.

I am grateful as well to the National Optics Institute (INO), in Quebec city, for their financial support during the years of this thesis, and for welcoming me every year at their head office. Many thanks to Dr. Pierre Galarneau from INO, who patiently followed the progress of this research in addition to providing interesting comments and questions.

My thanks also go to the Fonds Québécois de la Recherche sur la Nature et les Technologies (FQRNT) and the Natural Sciences and Engineering Research Council of Canada (NSERC) for their financial support via research grants. I thank the ECE department of McGill University for their financial support through travel and mobility awards.

Finally, I thank my friends and family, who have been of great support during these years; especially Joël & Cécile, Fred, and Caroline.

Statement of contributions

The work presented in this thesis results from the contributions of the author, as well as contributions from co-authors, as stated in Section 1.2.2. The National Optics Institute (INO) provided financial support for the author via research grants.

Chapter 1

Introduction

1.1 On pulsed lasers

The prediction of stimulated emission by Albert Einstein in 1917 has led to the creation of coherent sources of electromagnetic waves. An experimental confirmation of the existence of stimulated emission in 1928 by Rudolf Walter Ladenburg constituted the first step to the creation of microwave amplification by stimulated emission of radiations (MASERs) between 1952 and 1954. The Soviet physicist Nikolay Gennadiyevich Basov shared the 1964 Nobel Prize in Physics with Alexander Prokhorov and the american physicist Hard Townes for this work. Later, the american physicists Charles H. Townes and Arthur Leonard Schawlow described the first optical MASER, called light amplification by stimulated emission of radiation (LASER), which triggered laser science[1]. The first LASER is attributed to Gordon Gould in 1959, and demonstrated in 1960 by Theodore Maiman. Both were American Physicists.

In parallel, light guiding led to optical fibers, which now forms the backbone of nowadays optical communication systems. The first experiments of light guiding are reported in 1842 by the Swiss physicist Jean-Daniel Colladon and independently the French physicist Jacques Babinet: light guiding was achieved by total internal reflection in a water jet. It is likely, however, that such light guiding experiments were also performed in ancient times, since transparent glass dates back to 2500 years B.C. Glass fibers were first developed for their mechanical properties: being strong and thin, yet elastic; thus enabling the measurement of forces. Total internal reflection in glass fibers was used for various applications in the 1930s, but it is only in the 1950s that glass

fiber started to carry information.

In 1966, the French physicist Alfred Kastler was rewarded a Nobel price for his work from 1950 on optical pumping. Through the benefits of this technique and the progress on optical fibers, the first fiber lasers were presented in 1961. Fabry-Perot and ring architectures led to the design of lasers at various wavelengths. Modulated lasers also appeared in the 1960s, generating the first laser pulses, thereby reaching high peak powers or permitting data transmission with a succession of pulses representing binary zeros and ones.

Fiber lasers proved useful because of their multiple benefits: compactness, cost, ability to sustain powerful beams of high quality, good heat dissipation, and stability against environmental disturbances. Among them, several architectures for the creation of pulsed laser appeared, leading to the generation of pulses in the pico- and femtosecond range. To generate ultrashort pulses, the most common technique is mode-locking, which is caused by the additive interference of the cavity longitudinal modes. Triggering pulses in a laser cavity requires favouring the high intensities rather than the low ones, and this is achieved by the addition of a component featuring a nonlinear power transfer function. This function is such that the loss experienced by the high intensity light components is less important than the loss experienced by low intensity ones. By the Fourier transform properties, ultrashort pulses imply the formation of a broadband spectrum. With the addition of propagation in nonlinear media, pulses generated by ultrafast lasers are able to produce light covering a large wavelength range, which enables many applications.

1.1.1 Applications of pulsed lasers

Pulsed lasers have served as research and industrial tools in many domains for the last three decades. Building an exhaustive list of pulsed laser applications is difficult, but among them one can mention the following items. In chemistry, ultrafast lasers are used to trigger and monitor reactions [2]. In biology, two-photon microscopy facilitates the observation of molecules at low average power, thereby preserving the tissues [3], and imaging by optical coherence tomography (OCT) permits three-dimensional mapping of tissues, especially useful in ophthalmology. Frequency comb lasers led to the development of all-optical clocks and spectroscopy [4]. Distance measurement and chemical detection was demonstrated with light radars (LIDARs) [5]. Hole drilling, and other micro-machining applications have been performed with numerous benefits compared to other methods, enabling high precision and surface quality [6]. Ultrafast lasers also

enabled data transmission in our actual telecommunication systems [7]. Finally, energy research employs ultrafast lasers to trigger and observe nuclear reactions [8]. In Fig. 1.1, the domains of applications of lasers are indicated for given pulse peak powers and laser average power. Potential applications of lasers presented in this thesis are by design more likely to be used for biological, medical or imaging applications.

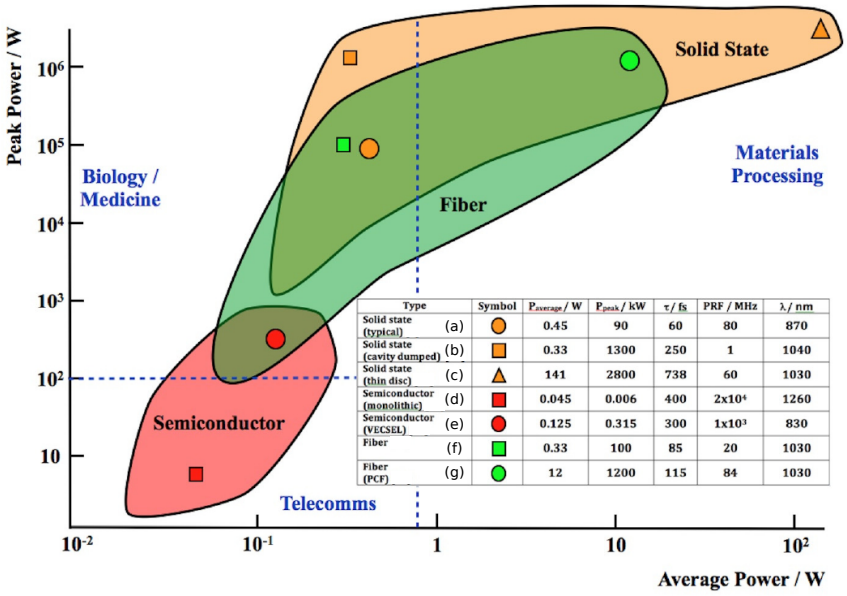

Type		Symbol	$P_{average}$ / W	P_{peak} / kW	τ / fs	PRF / MHz	λ / nm
Solid state (typical)	(a)	○	0.45	90	60	80	870
Solid state (cavity dumped)	(b)	□	0.33	1300	250	1	1040
Solid state (thin disc)	(c)	△	141	2800	738	60	1030
Semiconductor (monolithic)	(d)	■	0.045	0.006	400	$2x10^4$	1260
Semiconductor (VECSEL)	(e)	●	0.125	0.315	300	$1x10^3$	830
Fiber	(f)	■	0.33	100	85	20	1030
Fiber (PCF)	(g)	●	12	1200	115	84	1030

Figure 1.1 – *Peak power versus average power of several pulsed lasers, and indicative application areas. (a): [9], (b): [10], (c): [11], (d): [12], (e): [13], (f): [14]. From [15], reproduced with permission.*

The work reported in this thesis follows the introduction by Rochette et al. [16] of a new kind of self-pulsating laser based on a regenerative feedback loop. This new configuration enables the generation of short pulses by adequately balancing dispersion and nonlinearities, and it is likely that other cavities including nonlinear wavelength conversion stages may lead other means of pulse generation. Also, the uncommon pulsed regime of sources based on regeneration and its high degree of tunability still requires numerical and experimental analysis to fully grasp their operation, limits and benefits. The different sources presented in this work include that cavity, and reports other numerical and experimental results on self-pulsating cavities which all feature a broadband spectrum due to long nonlinear interactions. It is expected that these laser find applications in sensing as well as imaging, because of their wide bandwidth forming a smooth continuum instead of discrete spectral lines.

1.2 Main contributions

In this thesis, new broadband and self-pulsating laser architectures are reported and characterized.

After providing an overview of the concepts required for a good understanding of pulsed fiber lasers in Chapter 2, we present in Chapter 3 a cross-platform general-purpose processing on graphics processing units (GPGPU)-enabled software that was developed during this thesis, and which permits a fast yet accurate modelling of regenerative self-pulsating sources.

In Chapter 4, a numerical analysis focusing on pulse ignition in regenerative sources is presented. From the conclusions of this set of simulations follows an experimental demonstration of regenerative sources operating at large filter bandwidths.

Chapter 5 introduces a new kind of broadband self-pulsating laser based on soliton self-frequency shift (SSFS) and regenerative self-phase modulation (SPM). A numerical model, as well as experimental results indicate the predominance of modulation instability (MI) in the pulse ignition process. The source is therefore stochastic, and generates broadband bursts of pulses.

Finally, Chapter 6 presents new results regarding the noise-like pulse (NLP) regime. Ring cavities including a highly nonlinear chalcogenide or silica fiber are studied. An efficient broadband and dual-wavelength pulsed laser based on stimulated Raman scattering (SRS) is presented.

Each architecture has a particular behavior, adapted to different applications, which are described in the introductory section of each chapter. On top of the fact that the lasers reported in this thesis are broadband, their respective features include aperiodicity, ultrashort or noiselike pulse generation, multi-wavelength operation and tunability, depending on the underlying architecture. These operation regimes are described in Chapter 2. Applications which immediately follow are: sensing, low-coherence interferometry, communication systems, and chaotic LIDARs[5], among others.

1.2.1 Comparison with previous work

In this section, the sources developed in this thesis are briefly compared with previous work, and the contributions made to the three described architectures are highlighted.

Self-pulsating source based on cascaded SPM-OF regenerators

The initial report on the studied self-pulsating sources was performed at McGill by Rochette et al. [17] in 2008. This architecture is therefore relatively new, and and was just beginning to be investigated. Features of these sources are detailed in Chapter 4, and the work presented in this thesis highlights the operation domains of such sources, suggests and implements modifications to the architecture in order to sustain short and powerful pulses. The comparison with other pulsed sources is delicate because the latter do not share all features of regenerative sources based on SPM spectral broadening and offset filtering (SPM-OF) regenerators. Nevertheless, Chapter 4 presents improvements over the previous demonstration of these sources, increasing their efficiency, simplifying the experimental setup, and diminishing the pulse duration. In terms of pulse energy, the regenerative stages are inherently limiting, and the output pulses remain two or three orders of magnitude less energetic than self-similar or stretched pulse lasers.

Self-pulsating source based on regenerative SPM and SSFS

This source features a new design which has similarities with regenerative sources described above. However, the SSFS and offset filtering stage initiates a different operation regime, and there is no previous work on the matter.

Self-pulsating noiselike source

Since their initial report in 1997 [18], noiselike pulsed sources have been studied and reported frequently. Their stochastic behavior was recently confirmed by single-shot spectral measurements [19], and broadband pulses exceeding 100 nm were reported so far [20]. The approach presented in Chapter 6 does not extend the bandwidth of noiselike pulses beyond that value, but rather introduces dual-wavelength noiselike pulses initiated by SRS. To date, there was only one report of dual-wavelength noiselike pulses in the C-band and L-band, with bandwidths under 10 nm. In Chapter 6, dual-wavelength oscillation is reported with a wavelength offset of 100 nm. An efficient energy transfer from the pump to the first Stokes wavelength enables noiselike pulses of 84 nm full width at half maximum (FWHM), reaching 1700 nm. Finally, the use of chalcogenide fiber in the noiselike and solitonic regime is illustrated, and the potential of chalcogenide As_2S_3 fibers to generate ultrashort pulses at low pump power is investigated.

1.2.2 List of publications

Relevant journal publications

- T. North and M. Rochette. "Fabrication and characterization of a pulsed fiber ring laser based on As2S3". *Opt. Lett.* 37.4 (Feb. 2012), 716–718
  - T. North: Experimental demonstration, paper edition.
  - M. Rochette: Project supervision, paper edition.
- T. North and M. Rochette. "Broadband self-pulsating fiber laser based on soliton self-frequency shift and regenerative self-phase modulation". *Opt. Lett.* 37.14 (July 2012), 2799–2801
  - T. North: Experimental demonstration, paper edition.
  - M. Rochette: Project supervision, paper edition.
- T. North and M. Rochette. "Raman-induced noiselike pulses in a highly nonlinear and dispersive all-fiber ring laser". *Opt. Lett.* 38.6 (Mar. 2013), 890–892
  - T. North: Experimental demonstration, paper edition.
  - M. Rochette: Project supervision, paper edition.
- T. North and M. Rochette. "Analysis of Self-Pulsating Sources Based on Regenerative SPM: Ignition, Pulse Characteristics and Stability". *IEEE/OSA J. Lightw. Technol.* 31.23 (2013), 3700–3706
  - T. North: Experimental demonstration, paper edition.
  - M. Rochette: Project supervision, paper edition.
- T. North and M. Rochette. "Regenerative self-pulsating sources of large bandwidths". *Opt. Lett.* 39.1 (Jan. 2014), 174–177
  - T. North: Experimental demonstration, paper edition.
  - M. Rochette: Project supervision, paper edition.
- T. North, A. Al-kadry, and M. Rochette. "Analysis of self-pulsating sources based on cascaded regeneration and soliton self-frequency shifting". *IEEE J. Sel. Topics Quantum Electron.* PP.99 (2014), 1–1
  - T. North: Experimental demonstration, paper edition.
  - A. Al-kadry: paper edition.
  - M. Rochette: Project supervision, paper edition.

Other journals

- M. Gorjan, T. North, and M. Rochette. "Model of the amplified spontaneous emission generation in thulium-doped silica fibers". *J. Opt. Soc. Am. B* 29.10 (Oct. 2012), 2886–2890

- A. Velazquez-Benitez, R. Ahmad, T. North, M. Gorjan, J. Hernandez-Cordero, and M. Rochette. "All-Optical Broadband Variable Optical Attenuator Based on an As_2Se_3 Microwire". *IEEE Photon. Technol. Lett.* 25.7 (Apr. 2013), 697–700

Conferences

- T. North and M. Rochette. "Subpicosecond As2S3 fiber ring laser". In: *Photonics Conference (PHO), 2011 IEEE*. IEEE. 2011, 429–430
- T. North and M. Rochette. "Source Laser Auto-Pulsante via Auto-Décalage Fréquentiel de Solitons et l'Auto-Modulation de Phase". In: *Journées Nationales d'Optique Guidée (JNOG), 2012*. July 2012
- T. North and M. Rochette. "Dual-wavelength noiselike pulse generation via polarization rotation and stimulated Raman scattering in an erbium-doped fiber ring laser". In: *Proc. SPIE Photonics North 2013*. Vol. 8915. 2013, 891511–891511–6

In the conference papers above, the contributions are the following:

- T. North: Experimental demonstration, paper edition.
- M. Rochette: Project supervision, paper edition.

Chapter 2

Basic concepts

In this chapter, light propagation in optical fibers including nonlinear effects due to light-matter interaction are summarized, and illustrated by numerical simulations via the nonlinear Schrödinger equation (NLSE), which is introduced as well. Most techniques leading to the generation of ultrashort pulses are presented, with a focus on techniques that are enabled by all-fiber lasers. Finally, these techniques are classified by some of their output pulse properties, along with the year of their first demonstration.

2.1 Light propagation in fiber optics

Along with the numerous telecom applications that take advantage of light propagation on long distances, optical fibers exhibit interesting properties for the conception of lasers. To date, the fabrication of optical fibers, at least in silica, has been mastered and leads to ultra-low losses of about 0.2 dB per kilometer, and their handling and joining is easy. With a high beam quality insensitive to the diffraction effects observed in free-space, built-in amplification via various dopants, efficient heat dissipation and compactness, optical fibers have found applications in many domains.

In particular, all-fiber lasers operating at a wide range of average power in the kW range at 1µm were designed. In pulsed regimes, extremely high peak powers in the kilowatt range can be attained in all-fiber setups, with adequate pulse compression techniques at their output [32, 33]. All-optical setups provide a lot of flexibility to implement various laser architectures, including

ring lasers, loop mirrors, Fabry-Perot or regenerative sources, which are discussed in Section 2.4, and still reveal surprising and interesting operation regimes.

2.1.1 Design of optical fibers

Silica optical fibers enable the transmission of light over distances of hundreds or thousands of kilometers. Usually made of two concentric silica (SiO_2) cylinders, so-called "step-index" fibers ensure light guidance by a small change in their respective refractive indices, of typically 0.36% [1]. As illustrated by Fig. 2.1, each of these cylinders define the core and the cladding of the fiber, and the core has the largest refractive index n_1. Dopants such as Germanium (GeO_2), Phosphorus (P_2O_5) or alumina (Al_2O_3) are used to increase this refractive index in the fabrication process, while fluoride (F) or Boron (B_2O_3) can be used to decrease the refractive index n_c of the cladding [34], as shown in Fig. 2.2. In this case, the small index difference $\delta n = n_1 - n_c$ is characteristic of a weakly-guided waveguide, for which light transit time can be derived analytically [35, 36].

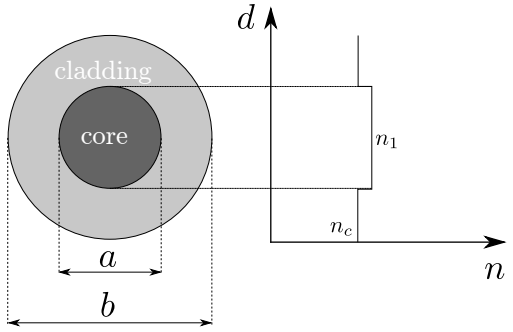

Figure 2.1 – *A step index fiber and its refractive index profile. The refractive index n_1 of the core is slightly larger than the cladding refractive index n_c.*

The core diameter a, the refractive indices and the wavelength of the input signal determine the number of modes that can travel in an optical fiber. The numerical aperture NA is used along with the normalized frequency, the V number, such that:

$$\mathrm{NA} = \sqrt{n_1^2 - n_c^2} \tag{2.1}$$

$$V = \frac{2\pi a}{\lambda}\mathrm{NA} \tag{2.2}$$

1. Corning SMF-28 fiber

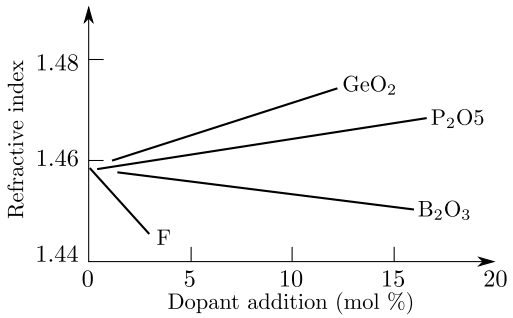

Figure 2.2 – *Effect of various dopants on the refractive index of a silica fiber. Figure adapted from [34].*

In particular, for $V < 2.405$, the fiber is said to be single-mode. If light propagation can be described by ray optics as a total internal reflection of the incident ray, one can describe it more precisely by considering it as a wave and solving the Maxwell equations in the linear case[37].

$$\nabla \cdot \mathbf{B} = 0 \quad \text{(Gauss' law for magnetism)} \tag{2.3}$$

$$\nabla \cdot \mathbf{D} = \rho \quad \text{(Gauss' law assuming low charges density)} \tag{2.4}$$

$$\nabla \times \mathbf{E} = -\frac{\partial}{\partial t}\mathbf{B} \quad \text{(Faraday's law of induction)} \tag{2.5}$$

$$\nabla \times \mathbf{H} = \mathbf{J} + \frac{\partial}{\partial t}\mathbf{D} \quad \text{(Maxwell-Ampere's equation)} \tag{2.6}$$

In Eq. (2.6), **B** is the magnetic flux density, **D** the electric flux density, **E** the electric field, **H** the magnetic field, and **J** the current density. Also:

$$\mathbf{B} = \mu_0 \mathbf{H} + \mathbf{M} \tag{2.7}$$

$$\mathbf{D} = \varepsilon_0 \mathbf{E} + \mathbf{P} \tag{2.8}$$

In a medium without free charges, $\mathbf{J} = 0$, $\rho = 0$, and in non-magnetic media, $\mathbf{M} = 0$, **B** and **D** can be replaced by their expression in function of **E** and **P** in Eqs. (2.5) and (2.6), leading to:

$$\nabla \times \mathbf{E} = -\frac{\partial}{\partial t}\left(\mu_0 \mathbf{H}\right) \tag{2.9}$$

$$\nabla \times \mathbf{H} = \frac{\partial}{\partial t}\left(\epsilon_0 \mathbf{E} + \mathbf{P}\right) \tag{2.10}$$

By replacing Eq. (2.10) in the curl of Eq. (2.9) and using the relation $\epsilon_0 = 1/(\mu_0 c^2)$, it follows that

$$\nabla \times \nabla \times \mathbf{E} = -\frac{1}{c^2}\frac{\partial^2 \mathbf{E}}{\partial t^2} - \mu_0 \frac{\partial^2 \mathbf{P}}{\partial t^2} \tag{2.11}$$

Eq. (2.11) leads to the pulse propagation equation described in Section 2.2.1, as the term accounting for polarization is split into a linear and nonlinear part [38]. The Maxwell equations also lead to the Helmholtz Eq. (2.12) which is more conveniently written in cylindrical coordinates ρ, ϕ, z, giving Eq. (2.13) with $k_0 = \omega/c$:

$$\nabla^2\tilde{\mathbf{E}} + n^2(\omega)\frac{\omega^2}{c^2}\tilde{\mathbf{E}} = 0 \tag{2.12}$$

$$\frac{\partial^2\tilde{\mathbf{E}}}{\partial\rho^2} + \frac{1}{\rho}\frac{\partial\tilde{\mathbf{E}}}{\partial\rho} + \frac{1}{\rho^2}\frac{\partial^2\tilde{\mathbf{E}}}{\partial\phi^2} + \frac{\partial^2\tilde{\mathbf{E}}}{\partial z^2} + n^2k_0^2\tilde{\mathbf{E}} = 0 \tag{2.13}$$

Where $\tilde{\mathbf{E}}$ is the Fourier transform of the electric field $\mathbf{E}$. The propagation is characterized by the eigenmode equation:

$$\left[\frac{J'_m(pa)}{pJ_m(pa)} + \frac{K'_m(qa)}{qK_m(qa)}\right]\left[\frac{J'_m(pa)}{pJ_m(pa)} + \frac{n_c^2}{n_1^2}\frac{K'_m(qa)}{qK_m(qa)}\right] = \left[\frac{m\beta k_0(n_1^2 - n_c^2)}{an_1p^2q^2}\right]^2 \tag{2.14}$$

With:

$$q = \sqrt{\beta^2 - n_c^2k_0^2} \tag{2.15}$$

$$p = \sqrt{n_1^2k_0^2 - \beta^2} \tag{2.16}$$

Where a is the core diameter, n_1 the wavelength-dependent core refractive index, and n_c the refractive index of the cladding. J_m are Bessel functions of order m, and K_m modified Bessel functions of order m. Each mode supported by the fiber is obtained by solving for β_{mn}. The intensity profile of the electric field therefore depends strongly of the refractive indices, the fiber geometry, and the input wavelength. Any combination of these will form a mode, which is defined by a propagation constant $\beta = n_{\text{eff}}\frac{2\pi}{\lambda}$. The effective refractive index n_{eff} describes the refractive index experienced by the mode, and is wavelength dependent.

2.1.2 Attenuation in optical fibers

Light input to an optical fiber inevitably experiences an exponential decrease of its power due to losses. At their origin, material absorption due to glass impurities including metal residues and OH^- ions. Linear scattering losses, induced by impurities smaller than the wavelength of the input light beam, result in Rayleigh scattering, proportional to the inverse of λ^4. Figure 2.3 depicts

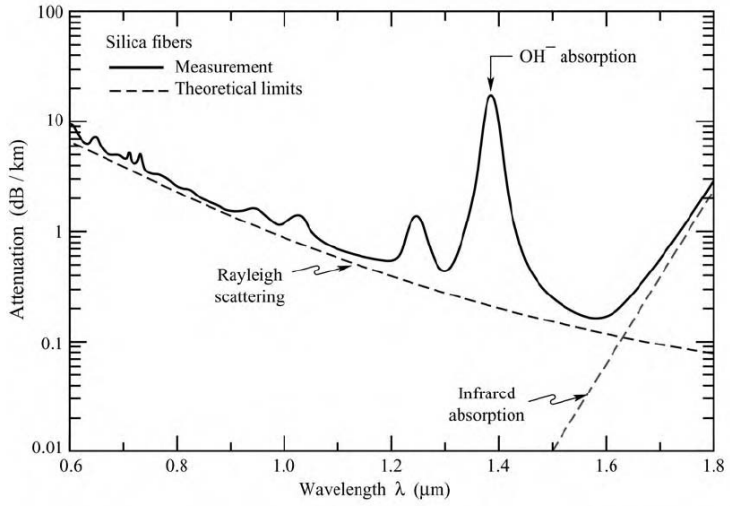

Figure 2.3 – *Transmission of silica optical fibers [39]. Copyright 2005 E. Fred Schubert. Reprinted with the permission of Cambridge University Press.*

the transmission of silica optical fibers, and shows an increasing loss at long wavelengths past 1.6 μm.

Bending losses also need to be taken into account: macro-bending occurs when the fiber is bent at an angle which does not ensure total internal reflection. Micro-bending losses, finally, are inhomogeneities at the core-cladding interface that are induced by mechanical stress.

2.1.3 Dispersion

A monochromatic light propagating in glass travels at a velocity $v_p = c/n(\omega)$, where $n(\omega)$ is the frequency-dependent refractive index of the glass. The frequency dependence of the refractive index is the origin of chromatic dispersion, where different frequency components travel at different velocities. The Sellmeier equation provides an expression for the refractive index as [40]:

$$n(\omega)^2 = 1 + \sum_{i=1}^{3} \frac{B_i \omega_i^2}{\omega_j^2 - \omega^2} \tag{2.17}$$

Parameters ω_i and B_i of Eq. (2.17) account for the i^{th} resonance frequency and its magnitude, respectively, according to Table 2.1. These coefficients are valid far from resonances for silica.

In an optical fiber, chromatic dispersion is induced by both its material properties and a waveguide contribution. Both of these contributions are accounted for in the effective refractive index

Resonance wavelength [µm]	Resonance amplitude
0.0684043	0.6961663
0.1162414	0.4079426
9.896161	0.894794

Table 2.1 – *Resonance wavelengths and amplitude coefficients.*

n_{eff} , that is derived from the properties of the propagating mode.

It is common to express chromatic dispersion as a series of coefficients around a central frequency ω_0, as a Taylor series :

$$\beta(\omega) = \beta_0 + \beta_1(\omega - \omega_0) + \frac{1}{2}\beta_2(\omega - \omega_0)^2 + \frac{1}{6}\beta_3(\omega - \omega_0)^3 + ... \tag{2.18}$$

For which β_k is:

$$\beta_k = \left(\frac{\partial^k \beta}{\partial \omega^k}\right)_{\omega=\omega_0} \tag{2.19}$$

In Eq. (2.18), β_0 corresponds to the wavenumber, β_1 is the inverse of the group velocity at the central wavelength, and β_2 is the chromatic dispersion coefficient. β_3, the third-order dispersion coefficient describes the variation of β_2. Higher order terms such as β_3 have to be included when $\beta_2 \approx 0$. The dispersion parameter D is defined as the derivative of β_1 with respect to the wavelength λ, and related to β_2 via Eq. (2.20). Their respective units are $\text{ps nm}^{-1}\,\text{km}^{-1}$ and $\text{ps}^2\,\text{km}^{-1}$.

$$D = \frac{d\beta_1}{d\lambda} = -\frac{2\pi c}{\lambda_0^2}\beta_2 \tag{2.20}$$

The dispersion slope is sometimes provided as $S = \beta_3 \left(\frac{2\pi c}{\lambda_0^2}\right)^2$ in $\text{ps nm}^{-2}\,\text{km}^{-1}$. The sign of the chromatic dispersion is of major importance in fiber optics, and defines which of the blue or red wavelengths travels faster. In so-called "normal dispersion" ($\beta_2 > 0$), longer wavelengths are faster than shorter ones, whereas it is the opposite in "anomalous-dispersion".

Silica single-mode fiber (SMF), for example, exhibits anomalous dispersion above 1310 nm. When other dispersion properties are required, the zero-dispersion wavelength (ZDW) of the fiber can be shifted via the conception of specialty fibers, mainly by altering the refractive index profile or the waveguide geometry.

2.1.4 Coherence

It is usual to define the temporal and spatial coherence as follows [41].

- Temporal coherence refers to the time duration over which a wave is coherent. Measured at different time intervals, the difference between the actual and the expected phase of the light beam describes its temporal coherence. Mathematically, the degree of coherence $\Gamma(t) \in [0, 1]$ and the coherence time in seconds are written:

$$\Gamma(t) = \frac{\langle \mathbf{E}^*(t)\mathbf{E}(t+\tau)\rangle}{\langle \mathbf{E}^*(t)\mathbf{E}(t)\rangle} \tag{2.21}$$

$$\tau_c = \int_{-\infty}^{\infty} |\Gamma(t)|^2 dt \tag{2.22}$$

  Here, $E(t)$ is the complex electric field at a given location, and $E^*(t)$ its conjugate.
- Similarly, the coherence length measures the degree of temporal coherence of a wave after some propagation, so that $\tau_l = c\tau_c$

Coherence time can also be related to the spectral width of the optical spectrum, and the coherence time τ_c is inversely proportional to the source spectral bandwidth:

$$\tau_c \sim \frac{1}{\Delta f} \tag{2.23}$$

In Eq. (2.23), Δf is the FWHM spectral width of the source. The coherence time therefore decreases with an increasing source bandwidth. An amplified spontaneous emission (ASE) source has a very low degree of coherence, while a continuous-wave (CW) laser of sharp linewidth has a high degree of coherence. The latter is therefore able to generate interference patterns in an interferometric setup.

2.1.4.1 Cross-coherence

Pulse-to-pulse coherence measurements, sometimes referred to as “cross-coherence”, quantify the relative phase differences between two consecutive pulses [42, 43]. The interferometric setup of Fig. 2.4 with a delay line provides a direct observation of interference fringes when the cross-coherence is high. In this setup, pulse $N + 1$ interferes with pulse N. If the relative phase of each spectral component is constant, a smooth interference pattern is observed, and constructive and destructive interference occurs at equal frequency intervals, as expected in a Michelson interferometer.

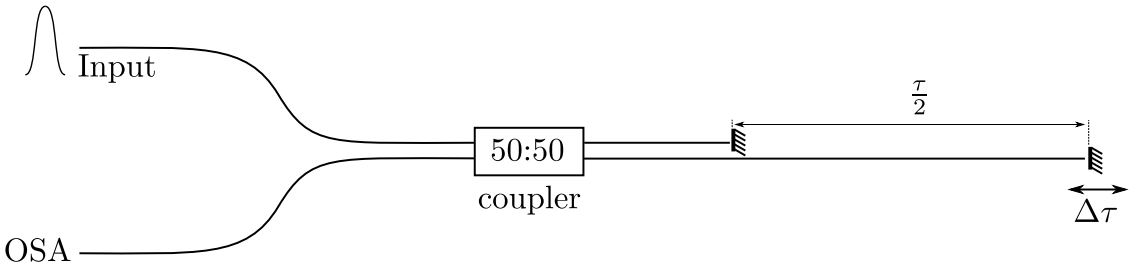

Figure 2.4 – *Setup for measuring cross-coherence of a pulsed source. OSA: optical spectrum analyzer.*

2.2 Nonlinear effects in optical fibers

Nonlinear optics considers that the interaction of light with light or matter alters its frequency via an intensity dependent change in the refractive index. Linear optics, as the name suggests, considers that the polarization density $\mathbf{P}$ has a linear relationship with the electric field $\mathbf{E}$, such that $\mathbf{P} = \epsilon_0 \chi \mathbf{E}$. This hypothesis holds for low intensities of $\mathbf{E}$, like the small angle approximation of a pendulum, for which that angle is expressed by a linear approximation corresponding to the first term of its Maclaurin series.

As light propagates in a medium, the polarization $\mathbf{P}$ is the resultant of all dipole contributions, and is not necessarily parallel with respect to $\mathbf{E}$. In the general case, the medium is anisotropic and χ is a tensor:

$$\mathbf{P} = \epsilon_0 \chi \mathbf{E} \ \text{, or:} \tag{2.24}$$

$$P_i = \epsilon_0 \sum_{j=1}^{3} \chi_{ij} E_j \ \ \forall i, j \in x, y, z \tag{2.25}$$

As indicated by Eq. (2.25), asymmetries in the host medium may induce cross-talk between the components of the electric field, and the x-component of the polarization, for instance, accounts as well for the y and z components of the electric field.

The nonlinear polarization $\mathbf{P}$ is expressed as a Taylor series, and introduces the $\chi^{(i)}$ coefficients, namely the i^{th} order susceptibilities:

$$\mathbf{P} = \epsilon_0 \left[\chi^{(1)} \cdot \mathbf{E} + \chi^{(2)} : \mathbf{EE} + \chi^{(3)} \mathbf{EEE} + \ldots \right] \tag{2.26}$$

The second order susceptibility $\chi^{(2)}$ requires a non-centrosymmetric medium, which is typical of crystals, for instance LiB_3O_5 or $CsLiB_6O_{10}$. Through such media, second harmonic generation (SHG) as well as the Pockels effect [first observed in 1893] are enabled [44], leading to many applications including measurement of ultrashort pulses or light modulation with Mach-Zender interferometers.

In fiber optics, the centrosymmetric nature of the host medium SiO_2, in a macroscopic scale, only features $\chi^{(3)}$ nonlinearity. The polarization term, in this case, is proportional to **EEE** rather than **EE**, and the refractive index changes with the square of the electric field, whereas it changes linearly with the electric field in the Pockels effect. As a result of $\chi^{(3)}$ nonlinearity, one also needs to account for an intensity-dependent attenuation, called two-photon absorption (TPA). Therefore, the effective nonlinear refractive index and nonlinear attenuation are written as functions of the wavelength and the nonlinear refractive and attenuation coefficients n_2 and α_2 [41]:

$$\tilde{n}(\omega, |E|^2) = n(\omega) + n_2|E|^2 \tag{2.27}$$

$$\tilde{\alpha}(\omega, |E|^2) = n(\omega) + \alpha_2|E|^2 \tag{2.28}$$

The Kerr effect leads to third harmonic generation, TPA, SPM, cross-phase modulation (XPM) and four-wave mixing (FWM). In fiber optics, it is convenient to introduce the nonlinear waveguide coefficient γ , in $W^{-1}\,m^{-1}$, as:

$$\gamma = \frac{n_2\omega_0}{cA_{\text{Eff}}} \tag{2.29}$$

which is related to the effective mode area A_{Eff}

$$A_{\text{Eff}} = \frac{\left[\iint_{-\infty}^{\infty} |F(x,y)|^2 dxdy\right]^2}{\iint_{-\infty}^{\infty} |F(x,y)|^4 dxdy} \tag{2.30}$$

with $F(x, y)$ the field distribution of the propagating mode.

Lastly, inelastic processes also occur during the propagation of light, and the SRS effect will be described in Section 2.2.6. In the next section, the NLSE is presented. It reveals the importance of nonlinear effects in optical fibers, and provides the basis for numerical simulation of pulse propagation.

2.2.1 Nonlinear Schrödinger equation

Starting from Eq. (2.11) of Section 2.1.1 (page 11),

$$\nabla \times \nabla \times \mathbf{E} = -\frac{1}{c^2}\frac{\partial^2 \mathbf{E}}{\partial t^2} - \mu_0 \frac{\partial^2 \mathbf{P}}{\partial t^2} \tag{2.31}$$

the polarization is decomposed into a linear part $\mathbf{P}_{\mathrm{L}}$ and a nonlinear part, $\mathbf{P}_{\mathrm{NL}}$.

$$\mathbf{P} = \mathbf{P}_{\mathrm{L}} + \mathbf{P}_{\mathrm{NL}} \tag{2.32}$$

Because $\nabla \times \nabla \times \mathbf{E} = \nabla(\nabla \cdot \mathbf{E}) - \nabla^2 \mathbf{E}$ and $\nabla \cdot (\nabla \mathbf{E}) = 0$, we obtain:

$$\nabla^2 \mathbf{E} = \frac{1}{c^2}\frac{\partial^2 \mathbf{E}}{\partial t^2} + \mu_0 \frac{\partial^2 \mathbf{P}_{\mathrm{L}}}{\partial t^2} + \mu_0 \frac{\partial^2 \mathbf{P}_{\mathrm{NL}}}{\partial t^2} \tag{2.33}$$

By perturbation analysis [38], the envelope of the electric field $A(z,t)$ is expressed via the generalized nonlinear Schrödinger equation (GNLSE). This equation takes several forms, including or excluding certain terms such as self-steepening (SS), SRS, XPM or FWM.

$$\frac{\partial A(z,t)}{\partial z} + \underbrace{\frac{\alpha}{2}A(z,T)}_{\text{losses}} + \underbrace{j\sum_{i=2}^{\infty}\frac{j^n}{n!}\frac{\partial^n}{\partial T^n}\beta_n}_{\text{dispersion}} = \underbrace{j(\gamma + j\gamma\frac{\partial}{\partial t})\left(A(z,T)\int_0^{\infty} R(t')|A(z,t-t')|^2 dt\right)}_{\text{nonlinearities, self-steepening and Raman}} \tag{2.34}$$

where T is a moving frame of reference such that $T = t - \beta_1 z$, $R(t)$ is the nonlinear Raman response of the medium, β_i are the dispersion coefficients, and α is the loss. Also, a positive carrier frequency is used, so that $E(t) = 1/2\exp(j\omega_0 t - j\beta z)$ +c.c. Self-steepening accounts for the intensity dependence of the group-velocity. This effect is typically weak for pulses longer than 100 fs. For pulses longer than 100 fs, the Raman response can be linearly approximated, and Eq. (2.34) becomes [38, p.40]:

$$\frac{\partial A(z,t)}{\partial z} + \frac{\alpha}{2}A(z,T) + j\sum_{i=2}^{\infty}\frac{j^n}{n!}\frac{\partial^n}{\partial T^n}\beta_n = j\gamma\left(|A|^2 A + \frac{j}{\omega_0}\frac{\partial}{\partial T}([|A|^2 A) - T_R A\frac{\partial |A|^2}{\partial T}\right) \tag{2.35}$$

The Raman response time T_R depends on the material, and for silica fibers it is common to use T_R =3 fs.

From the GNLSE, nonlinear effects can be studied separately by ignoring irrelevant terms. In the next subsections, we describe the SPM, XPM, FWM and SRS nonlinear effects, which serve as the basis for the generation of broadband pulses.

2.2.2 Self-phase modulation

First observed in 1967 in carbon disulfide and more than ten years later in silica optical fibers [45, 46], SPM is a manifestation of the Kerr effect, for which the propagating signal experiences a nonlinear phase shift that is proportional to its intensity [47]. By neglecting the dispersion terms and higher order nonlinear effects of the NLSE, the unary pulse envelope $U(z,t)$ is related with the nonlinear waveguide coefficient γ and the signal power P_0. The differential equation

$$\frac{\partial U}{\partial z} = j\gamma P_0 |U|^2 U \tag{2.36}$$

can be solved analytically with a solution of the form $U(z,t) = V(z,t)\exp(j\phi_{\text{NL}}(z,t))$, and Eq. (2.36) becomes

$$\frac{\partial V}{\partial z}\exp(j\phi_{\text{NL}}) + Vj\exp(j\phi_{\text{NL}})\frac{\partial \phi_{\text{NL}}}{\partial z} = j\gamma P_0 |V|^2 V \exp(j\phi_{\text{NL}}) \tag{2.37}$$

The real and imaginary part are equalled and lead to

$$\frac{\partial V}{\partial z} = 0 \text{ (no profile change in the time domain)} \tag{2.38}$$

$$\frac{\partial \phi_{\text{NL}}}{\partial z} = P_0\gamma |V|^2 \tag{2.39}$$

and hence:

$$\frac{\partial \phi_{\text{NL}}}{\partial z} = |U(0,t)|^2 \exp(j\phi_{\text{NL}}(z,t)) \text{ (intensity dependent phase shift)} \tag{2.40}$$

During propagation, the pulse undergoes an intensity dependent phase-shift on its temporal profile. Fig. 2.5 illustrates the time-dependent phase change (chirp) for a Gaussian and a Sech pulse. By the modulation properties of the Fourier transform, a phase-shift in the time-domain corresponds to a frequency shift in the frequency domain: new frequency components are generated continuously as the light beam propagates in the fiber. SPM leads to spectral broadening when the initial pulse is unchirped [2], as shown in Fig. 2.6. Because the pulse chirp has a pair of same values at two different times and because the pulse already has its intensity profile, the resulting spectral intensity for a given wavelength depends on the amplitude and phase differences of each contributing components. This leads to an oscillatory structure as ϕ_{NL} increases [48]. The pro-

2. In general, positively chirped pulse broaden, and negatively chirped pulses shrink in absence of chromatic dispersion.

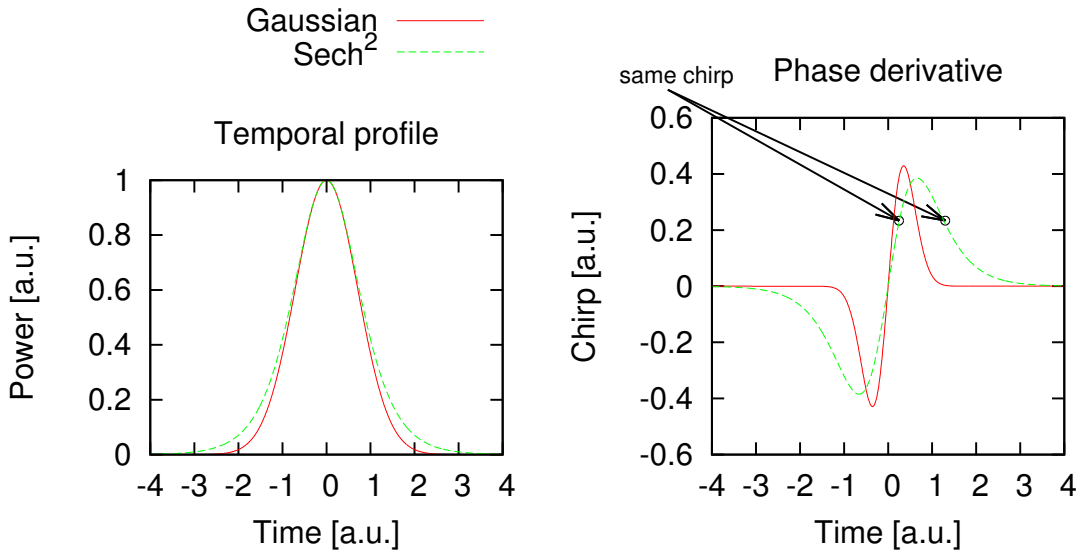

Figure 2.5 – *Left: pulse temporal profile, for gaussian and sech pulses. Right: Corresponding chirp. Temporal positions that correspond to a same chirp induce interferences, leading to the typical oscillatory structure of SPM broadening.*

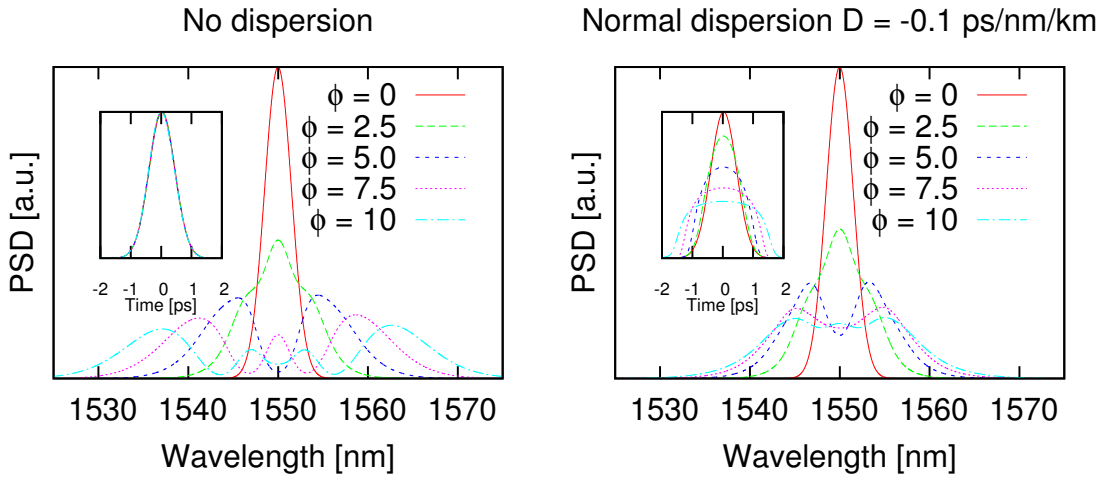

Figure 2.6 – *Propagation of a 1 ps gaussian pulse in a 1 km-long nonlinear fiber of* $\gamma = 10 \times 10^{-3}\ W^{-1}\ m^{-1}$. *The nonlinear phase shift is* $\phi = \gamma P_0 L$ *Left: No chromatic dispersion. Right: Normal dispersion. Insets: time-domain pulse shape.*

file of the SPM-induced spectral broadening is also affected by the chromatic dispersion of the medium, and can lead to optical wave-breaking in normal dispersion regime, as well as optical solitons, which are the subject of Section 2.3, page 23.

2.2.3 Cross-phase modulation

A nonlinear coupling between a set of optical fields of different frequencies or of different polarization axes occurs by the effect of XPM, when these fields overlap in time [49]. While SPM induces a phase shift on its own signal, XPM induces a phase shift that is proportional to the signal intensity on any overlapping signal.

The NLSE must therefore be written as a system of coupled equation, one per optical field

$$\frac{\partial A_k}{\partial z} + \frac{\alpha}{2}A(z,T) + \beta_{1,k}\frac{\partial A_k}{\partial t} + j\sum_{i=2}^{\infty}\frac{j^n}{n!}\frac{\partial^n}{\partial T^n}\beta_{n,k} = j\gamma\left(\underbrace{|A_k|^2}_{\text{SPM}} + \underbrace{B\sum_{m\neq j}(|A_m|^2)}_{\text{XPM}}\right)A_j \tag{2.41}$$

In Eq. (2.41), SRS and SS are ignored. The $\beta_{1,k}$ term accounts for the group-velocity of each optical field. In the case of XPM interaction between two polarization axes, $B = 2/3$, and it can be shown that for low birefringence, the FWM terms are cancelled. In the general case, FWM is expected when the phase-matching condition is required. This term becomes rather complex in the general case, and was ignored in Eq. (2.41). The reader can refer to [38, chapter 10] for a comprehensive and expended form of these equations for $k = 0 \ldots 3$.

In the degenerate case, XPM accounts for nonlinear polarization rotation (NPR), well known as part of a mode-locking technique which transforms polarization rotation into amplitude modulation, as discussed in Section 2.4.2.

2.2.4 Four-wave mixing

FWM is another consequence of $\chi^{(3)}$ nonlinearities[50, 51]. When the initial electric field is composed of several CW waves of different frequencies ω_i, the nonlinear polarization term of Eq. (2.26) includes a large number of terms. Some of them involve only the electric fields at

frequencies ω_i, and are responsible for SPM. Some others involve the electric fields at ω_i multiplied by the intensity of other electric fields, therefore accounting for XPM. Finally, sum or differences of the electric field terms account for FWM. A phase-matching condition also results from this equation, and the consequences of FWM are that photons from one or more frequencies are transformed into new photons at different frequencies, such that there is conservation of the energy and momentum [38].

From two pumps at ω_1 and ω_2, photons are created at frequencies ω_3 and ω_4 such that [38, Chap. 10]:

$$\omega_1 + \omega_2 = \omega_3 + \omega_4 \tag{2.42}$$

If phase-matching is satisfied ($\Delta k = 0$)

$$\Delta k = \beta_3 + \beta_4 - \beta_1 - \beta_2 = \frac{1}{c}(\tilde{n}_3\omega_3 + \tilde{n}_4\omega_4 - \tilde{n}_1\omega_1 - \tilde{n}_2\omega_2) \tag{2.43}$$

with $\tilde{n}_i$ the effective mode index at frequency ω_i.

If $\omega_1 = \omega_2$, FWM is said to be degenerate, and two new frequencies are generated on each side of the pump frequency, with an equal frequency offset.

2.2.5 Modulation instability

MI generally arises when a light beam propagates in a medium with anomalous dispersion at the beam wavelength. Considering a CW signal input to a fiber, the interplay of nonlinearities and dispersion amplifies the small perturbations of the CW signal, leading to the generation of a train of pulses.

By a linear stability analysis, the NLSE is solved, without high order dispersion terms or loss, in the frequency domain [38]. The gain spectrum is then given by

$$g(\omega) = |\beta_2\Omega|\sqrt{\Omega_c^2 - \Omega^2} \quad \forall\Omega \in [-\Omega_c, \Omega_c] \tag{2.44}$$

where $\Omega_c = 4\gamma P_0/|\beta_2|$. The gain provided for a highly nonlinear fiber (HNLF) with γ =12.5 $\mathrm{W^{-1}\,km^{-1}}$ and various signal power P_0 is shown in Fig. 2.7. The train of pulses has a period inversely proportional to the frequency of maximum gain $\Omega_{\text{max}} = \pm\sqrt{2\gamma P_0/|\beta_2|}$. Pulses induced from a CW signal induce supercontinuum (SC) generation because of their interactions, FWM, and a Raman induced frequency shift [52, 53].

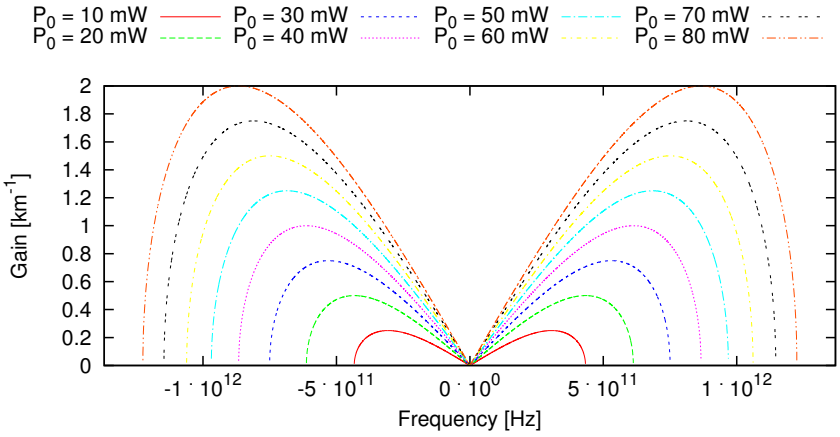

Figure 2.7 – *Gain of modulation instability for a HNLF of β_2 =2.09 ps^2 km^{-1} for various peak powers P_0.*

2.2.6 Stimulated Raman scattering

Predicted in 1923 and reported in 1928[54, 55], Raman scattering is a light-matter interaction for which photons incident to molecules or atoms interact with them by exchanging energy. Re-emitted photons are frequency-shifted. Raman scattering is therefore said to be "inelastic", contrary to Rayleigh scattering [3] where incoming photons are deviated without being altered in wavelength.

The high intensity of an optical beam causes vibrations of the molecular structure of the propagation media. Energy is therefore exchanged via optical phonons, absorbing some of the incoming photon energy. The remaining energy is re-emitted as an optical photon, at a lower frequency, at the so-called "Stokes wavelength". The interaction of an incoming photon with the lattice can also generate an optical photon of higher frequency, at the "anti-Stokes" wavelength [56].

2.3 Optical solitons

Solitons, as commonly defined, are a particularly interesting solution of the NLSE [57]. They are the result of the interplay of chromatic dispersion and nonlinearity, which balance each other [58]. Solitons of the first order keep their shape during propagation, in absence of loss, while higher

3. Detailed in a series of articles in *Philosophical Magazine* from 1871 to 1899.

order solitons undergo a periodic deformation, but recover their shape after a distance L_r. Solitons have an analytical formulation of Eq. (2.45).

$$A(t) = \frac{L_D}{L_{\text{NL}}}\sqrt{P_0}\,\text{sech}\left(\frac{t}{T_0}\right) \tag{2.45}$$

Provided that the dispersion length L_D and the nonlinear length L_{NL} are defined as follows:

$$L_D = \frac{T_0^2}{|\beta_2|} \tag{2.46}$$

$$L_{\text{NL}} = \frac{1}{\gamma P_0} \tag{2.47}$$

The soliton order N is

$$N^2 = \frac{L_D}{L_{\text{LN}}} = \frac{\gamma P_0 T_0^2}{|\beta_2|} \tag{2.48}$$

For solitons of order $N > 1$, the soliton period is $L_r = \pi/2 \cdot T_0^2/|\beta_2|$.

The solitons described above are often referred to as “bright solitons”, and have their counterpart, called “dark solitons”, which exist in normal chromatic dispersion. They form a gap into a continuous background, propagating without being altered [59].

Other particular solutions of the NLSE include Akhmediev breathers and Kuznetsov-Ma solitons [60–63]. A limiting case of these solutions is the Peregrine soliton [64]. This set of exact solutions of the NLSE are localized temporally, spatially or both. These solitons were observed in nonlinear optical fibers recently, and already found applications, such as the generation of pulses at high repetition rates [65].

The solitons described above are issued of conservative (Hamiltonian) systems, for which the nonlinear phase shift exactly compensates for dispersion during propagation. In a more general case, in the presence of losses and gains as well as dispersion-managed systems, so-called dispersion-managed (DM) solitons are sustained. Their temporal duration, peak power and chirp change along the path, but they retrieve their initial duration at a given period. These solitons therefore “breath” as they propagate [66], as illustrated in Fig. 2.8.

2.3.1 Soliton self-frequency shift

The Raman effect causes a frequency-dependent gain along propagation in a fiber, with a maximum of gain which is red-shifted with respect to the pump signal, as discussed in 2.2.6.

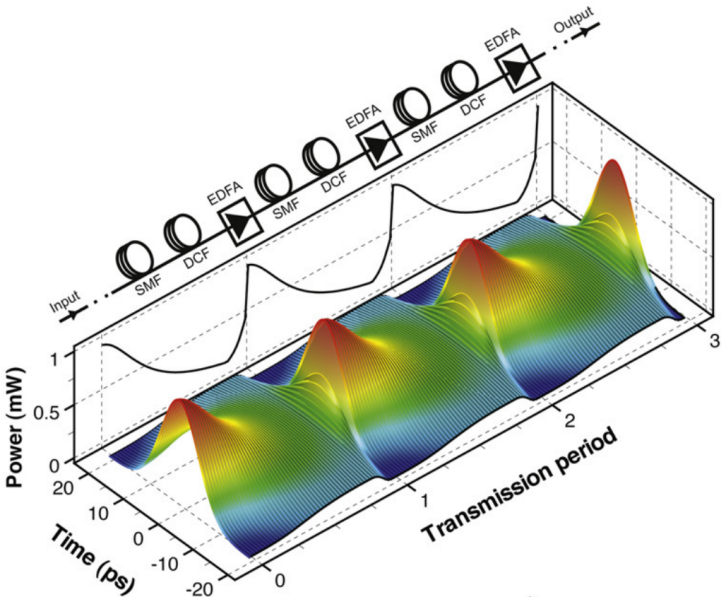

Figure 2.8 – *Propagation of DM solitons in an optical system. From [66]. Reprinted from Physics Reports, Vol 521, Sergei K. Turitsyn, Brandon G. Bale, Mikhail P. Fedoruk, "Dispersion-managed solitons in fibre systems and lasers", pp. 135–203, Copyright (2012), with permission from Elsevier.*

Because of that, a broadband soliton propagating in a fiber may self-induce gain for its longer wavelengths [67]. If it is the case, the soliton is continuously shifted towards the long wavelengths as it propagates, and this effect is as significant as the pulse is broadband. In fact, the rate of shift is proportional to the fourth power of the soliton duration.

Figure 2.9 illustrates the propagation of a higher order soliton inside a silica HNLF. The soliton experiences fission at the very beginning of the propagation. In the time domain, this corresponds to the division of the initial pulse into three fundamental solitons. The most powerful one, also the pulse of shortest duration, experiences SSFS and shifts towards the red wavelengths. Because the fiber has anomalous dispersion, the red-most wavelengths components travel slower than the blue-most components. Therefore, the pulse acquires a temporal delay of $\sim$150 ps.

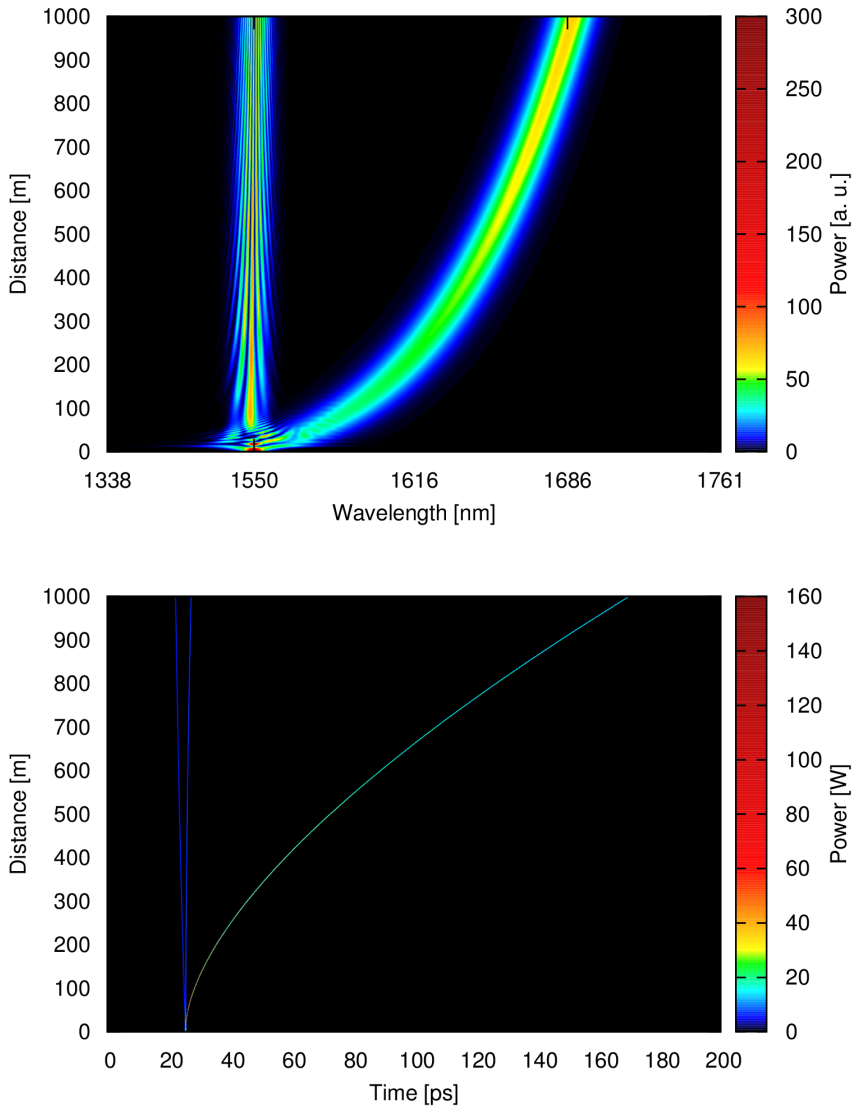

Figure 2.9 – *Illustration of soliton shifting in a silica nonlinear fiber, with* $D = 2.09\,ps\,nm^{-1}\,km^{-1}$ *and the slope of dispersion* $S = 0.02\,ps\,nm^{-2}\,km^{-1}$ *at 1550 nm.*

2.4 Generation of ultrashort pulses

Lasers are known to operate in various regimes, in which they generate pulses with different duration, temporal shape, and spectral features. These regimes are triggered via several techniques. We focus on techniques that yield to short pulses without active elements inside the laser cavity. They can be enumerated as follows:

- Mode-locking: a fast saturable absorber promotes higher peak powers, and yields ultrashort pulses.
- Noise-like pulses regimes: based on saturable absorption, generate packets of noise
- Cascaded regeneration: a saturable absorber and intracavity offset filtering generate ultrashort pulses.

Q-Switched operation, achieved by modulating the intracavity losses, is not considered because the generated pulses are usually in the nanosecond range [68]. After presenting common techniques for the measurement of ultrashort pulses, the techniques for ultrashort pulses generation listed above, and of picosecond duration at most, are detailed. They constitute a framework for this thesis, in which several of these methods were investigated.

2.4.1 On the measurement of ultrashort pulses

In this section, we review some techniques of ultrashort pulse measurement. We emphasize that the most widespread pulse measurement techniques operate by averaging over a significant number of pulses, and therefore only provide a realistic picture of the pulse properties when the pulse to pulse changes are small. Furthermore, only two of the three broadband sources studied in the next chapters do fulfill such conditions, with the exception of the solitonic regime of Chapter 6.

The limited bandwidth of electrical detectors does not allow a proper sampling of ultrashort pulses of pico- or femtosecond duration. To overcome this limitation, several techniques have been developed, and among them SHG autocorrelators and frequency resolved optical gatings (FROGs) devices enable a partial description of the pulse profile, and phase for the FROG.

2.4.1.1 Intensity autocorrelation

Intensity autocorrelators collimate the signal and its copy, delayed by a variable time τ, into a $\chi^{(2)}$ crystal. A photo-multiplier tube (PMT) or a photodiode is placed behind this crystal, and

measures the intensity of the frequency-doubled signal as a function of the time delay τ. At the telecom wavelengths of 1550 nm, the frequency-doubled signal falls into the near-infrared at 775 nm, and can be detected with a silicon photodiode. It was also shown that the crystal can be replaced by an adequate photodiode measuring the autocorrelation of the signal via a TPA process, for example in a GaAsP photodiode [69, 70]. In this case, the photodetector must not be sensitive to the signal wavelength, and the absorption band gap energy must be less than the energy of two signal photons.

Fig. 2.10 depicts the schematic of a common autocorrelator. It is important to note that the

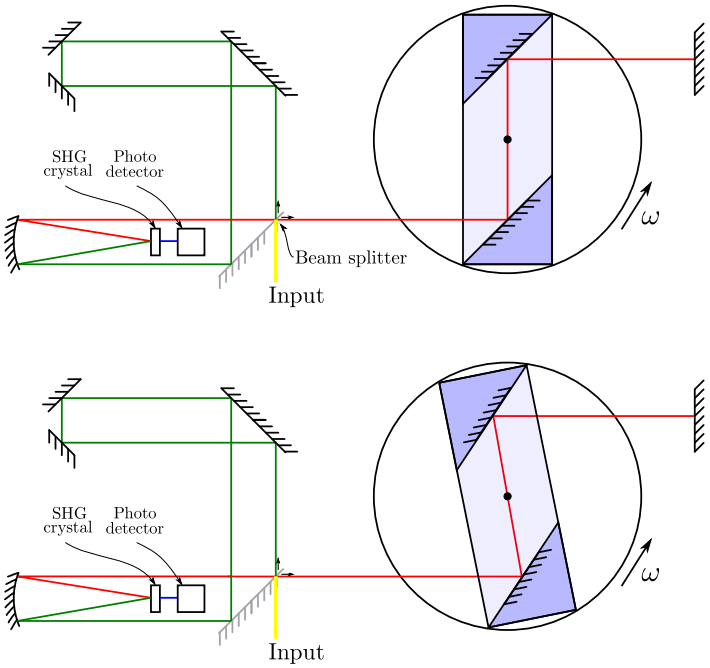

Figure 2.10 – *Schematic of a commercial autocorrelator. A time delay τ is induced by rotation of two parallel mirrors, and the propagation distance (in red) varies linearly (or almost) around $\tau = 0$.*

speed of variation of τ is usually small with respect to the pulse-to-pulse time delay. The measured output intensity at delay τ is a convolution of the signal with itself

$$I_{\text{out}}(\tau) \sim \int_{-\infty}^{\infty} I_{\text{in}}(t) I_{\text{in}}(t-\tau) \mathrm{d}t \tag{2.49}$$

corresponds to an averaging over a large number of pulses. Intrinsically, the intensity autocorrelation of a signal yields to a symmetrical response and loses the phase information. An estimate of the actual pulse duration is obtained by assuming a pulse shape [71]. For Gaussian pulses, the actual pulse duration is $\Delta t_{\text{FWHM}} = \Delta t_{\text{FWHM,autocorr}}/1.44$, whereas sech pulses have $\Delta t_{\text{FWHM}} = \Delta t_{\text{FWHM,autocorr}}/1.54$.

On the other hand, if the pulse-to-pulse variations are significant, the autocorrelation figure degenerates towards the autocorrelation of noise, which consists of a Gaussian pedestal with a sharp peak at $\tau = 0$. To overcome this limitation, single-shot autocorrelators were developed [72].

2.4.1.2 FROG devices

To address the problem of phase retrival, the FROG devices extract more information from the pulse autocorrelation [73]. Instead of measuring the intensity of the frequency-doubled signal like intensity autocorrelators, FROGs use a spectrometer to resolve the frequency components of the doubled signal at all times τ. Namely, the photodiode of Fig. 2.10 is replaced by a diffraction grating and a series of photodetectors, resolving the set of decomposed wavelengths. FROGs therefore output a spectrogram of the pulse, from which the phase information can be extracted via an iterative algorithm [74, 75].

The frequency and time dependent FROG output is

$$I_{\text{FROG}}(\tau) \sim \left| \int_{-\infty}^{\infty} I_{\text{in}}(t) I_{\text{in}}(t-\tau) e^{i\omega t} \mathrm{d}t \right|^2 \tag{2.50}$$

2.4.1.3 Single-shot spectral measurements

Common optical spectrum analysers (OSAs) are composed of a diffraction grating, which separates the input signal into its frequency components. A photodiode captures the intensity of the signal in each wavelength slit of spectral width $\Delta\lambda$. For that matter, spectrum analyzers require an acquisition time that usually exceeds the measured pulse duration. Therefore, the OSA performs an averaging of the input signal over a certain number of pulses, and does not perform single-shot measurements.

Most pulsed lasers produce pulse trains that are regular, with excellent pulse-to-pulse similarities. However, other kind of self-pulsating sources operate in a regime for which bursts of noise

are generated. SC sources also include rogue waves, which are noise-dependent, and therefore are comparable to random processes.

To characterize such pulses, single-shot measurements are necessary, and wavelength-to-time mapping techniques constitute a simple yet efficient way to measure instantaneously the spectrum of a pulse. The implementation of such a method was proposed in 1999 by Kelkar et al. [76], and revisited recently by Wetzel et al. [77] for the analysis of SCs. Figure 2.11 illustrates the experimental setup of this technique, which includes a long length of SMF, of a dispersion $D = 17\,\mathrm{ps\,nm^{-1}\,km^{-1}}$, and a photodiode. As the pulse propagates in the dispersive fiber, the components of the pulse

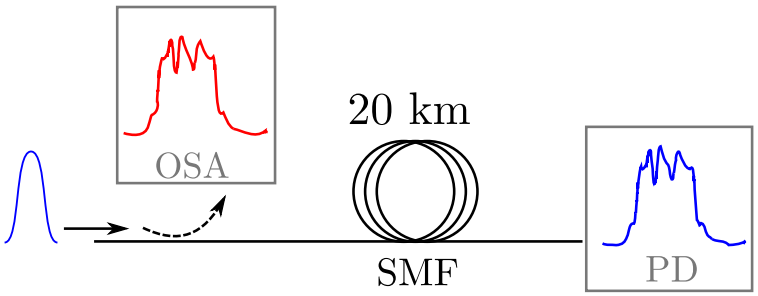

Figure 2.11 – *Setup for the time-domain single-shot spectrum analyzer. OSA: optical spectrum analyzer, PD: photodiode, SMF: single-mode fiber.*

experience a time delay which is proportional to their wavelength at the first order approximation, and this time delay $\Delta\tau$ is given by Eq. (2.51).

$$\Delta\tau = DL\Delta\lambda + \cancel{\frac{d}{d\lambda}DL(\Delta\lambda^2) + \ldots} \tag{2.51}$$

Silica SMF-28 has a zero-dispersion wavelength around 1310 nm, and hence anomalous dispersion at the telecom wavelengths of 1550 nm, with a low dispersion slope, and the first order approximation is accurate enough, as confirmed by experimental results.

The consequence of Eq. (2.51) is that any signal transforms into its Fourier transform when experiencing a large chirp. The output signal is observed in the time-domain, and for a sufficiently dispersive medium, the time delay is of several nanoseconds, large enough to be captured by a standard real-time oscilloscope.

Figure 2.12 presents the result of this method for the case of a pulse sent into a HNLF, in the normal dispersion regime.

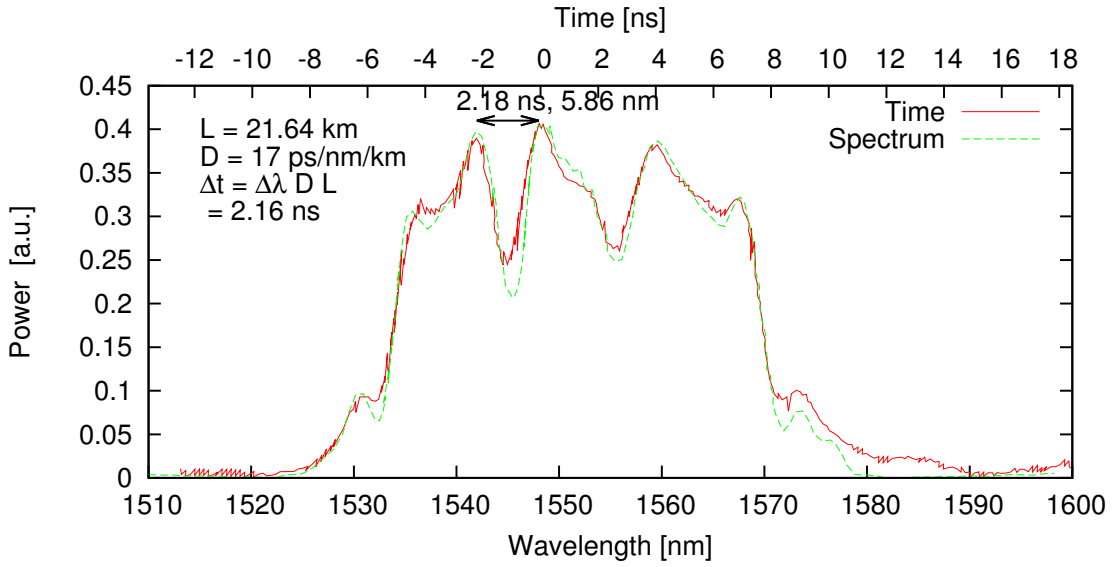

Figure 2.12 – *Spectral measurement: single-shot time domain measurement and averaging by an OSA.*

2.4.2 Mode-locking

As implied by its name, mode-locking occurs when the modes propagating in a laser have a fixed relationship, leading to an interference pattern that displays sharp peaks on a noise-less background. The first mode-locked laser was reported in 1964 [78] in free space, in 1986 with a doped fiber as gain medium [79]. In a ring laser resonator, the mode spacing in Hz is defined by the cavity length L, the speed of light c_0 and the refractive index of the medium n is referred to as the free spectral range (FSR) such as $\Delta_{\text{FSR}} = cn^{-1}L^{-1}$. Because the gain medium of lasers is usually much broader than the FSR, a large number of modes are sustained in the cavity, and the resulting electric field is the sum of the individual contributions of each mode. The relative phase of these modes indicates if the source is noise-like (no fixed phase relationship), or has some structure. More precisely, the total electric field can be written:

$$E_{\text{tot}} = \sum_{i=0}^{N} A_i \exp(j\omega_i t + \phi_i) \tag{2.52}$$

In Eq. (2.52), the i^{th} mode has an amplitude A_i, a frequency proportional to ω_i, and a phase ϕ_i. Fundamental mode-locking occurs if $\phi_{i+1} - \phi_i = \text{cte}\ \forall i \in 0 \dots N-1$, as illustrated in Fig. 2.13.

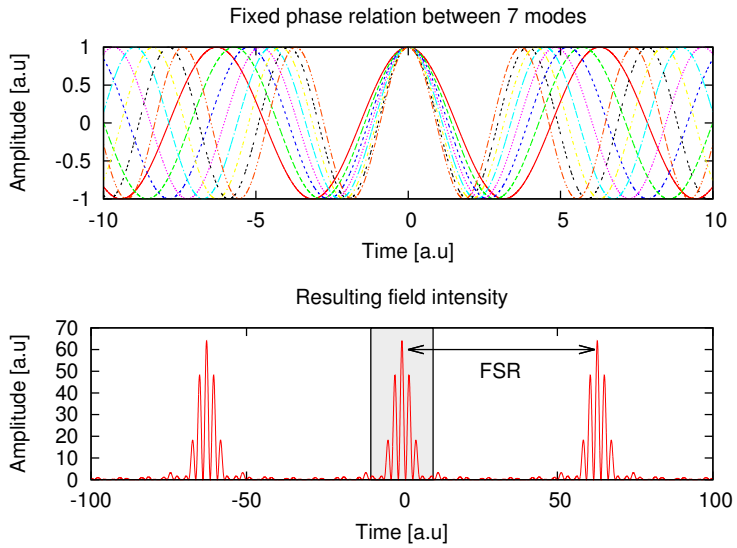

Figure 2.13 – *Interference pattern resulting of the addition of 7 modes with a fixed phase relationship.*

A train of pulses occurs at the repetition rate of the cavity. The larger the number of modes, the shorter the output pulses. In fiber lasers doped with erbium ions, the gain window spreads over about 3.77 THz at 1550 nm. For a cavity of L =10 m, the FSR is therefore 20 MHz, and the number of modes is close to 200 000. Constructive interference of modes over that bandwidth can result in ultrashort pulses of a few tenths of femtoseconds, and limited by the chromatic dispersion and wavelength dependent changes in the refractive index. Fundamental mode-locking enforces a fixed repetition rate. In harmonic mode-locking, however, multiple pulses travel in the resonator, formed by different sets of modes [80].

Mode-locking can be triggered actively by a modulation of the signal inside the cavity, or passively, using a saturable absorber [81, 82]. Passive mode-locking relies on the nonlinear power transfer function of an absorber, which favors high intensities.

We review free-space and all-fiber setups that act as saturable absorber due to interferometric effects, to the Kerr effect, to $\chi^{(2)}$ nonlineariries, or to semiconductors. We limit our description to self-pulsating sources, in which the pulses are spawned in a resonant cavity, hence including a gain medium. This excludes all locking techniques taking advantage of seed pulses, which operate by shaping or shortening existing pulses, or which turn CW beams into a series of pulses. Mode-

locking techniques based on $\chi^{(2)}$ processes are briefly described in Sections 2.4.2.9 to 2.4.2.10, as $\chi^{(2)}$ mode-locking techniques were not investigated in the framework of this thesis. Likewise, no ultra-high repetition-rate frequency combs with large mode spacing are presented in detail.

2.4.2.1 Nonlinear loop mirror

Nonlinear mirrors belong to the passive mode-locking techniques often referred to as additive pulse mode-locking (APM) [83]. The principle of APM is that the propagating pulse is split into two versions of itself, experiencing different phase shifts via nonlinear effects when passing through a Kerr medium. They are then recombined at an optical element such as a coupler of a polarizer, and the interference of these two versions results in a new pulse whose peak power and energy is a function of the differential phase shift between the two versions of the pulse.

Initially, the nonlinear optical loop mirror (NOLM) is composed of an optical coupler of a splitting ratio α forming a loop with an input and an output, playing the role of saturable absorber [84]. It is depicted in Fig. 2.14. The input signal is split and propagates in the two arms, and

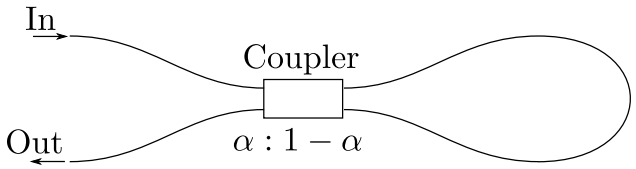

Figure 2.14 – *NOLM with a coupler of ratio* $\alpha : 1 - \alpha$

recombines at the coupler. The path of both arms have the same length, but if $\alpha \neq 0.5$, the signal in each arm has a different intensity, and therefore experiences a different amount of nonlinear phase shift due to the Kerr effect. The recombination of both signals is intensity dependent and quasi-instantaneous, and leads to the power transfer function of Fig. 2.15. In order to operate with an interesting modulation, NOLMs have to be used with ratios close to 50:50, or with a high nonlinear parameter. Ratios that are close to 50:50 do not take advantage of nonlinearities, since the peak power difference between the clockwise and counter-clockwise signal is low. At high γ, the limiting factor becomes the spectral broadening induced by SPM.

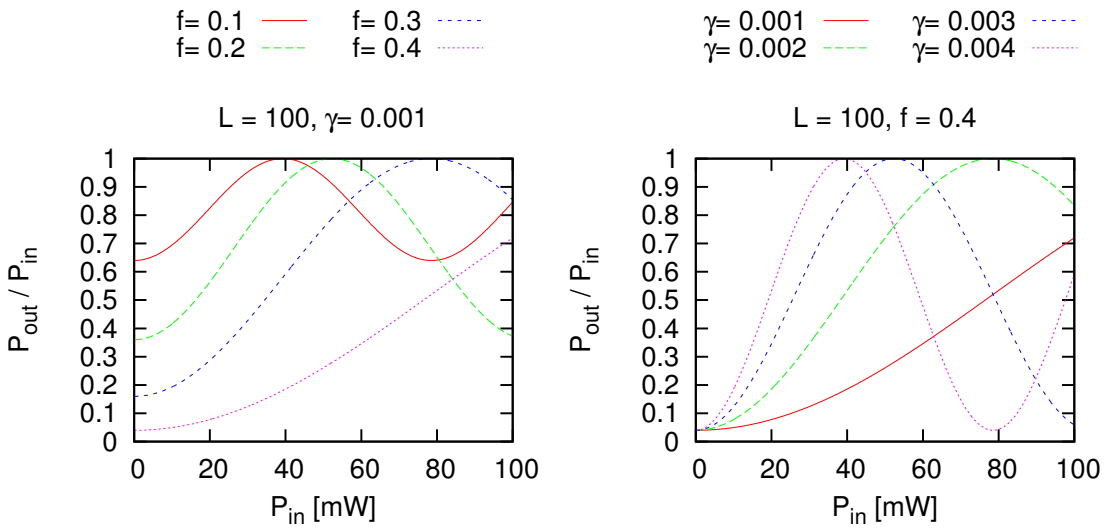

Figure 2.15 – *Transfer function of an NOLM with various coupler ratio f (left), and various nonlinear waveguide parameters γ (right).*

2.4.2.2 Nonlinear amplifying loop mirror

The nonlinear amplifying loop mirror (NALM) is an extension of the NOLM, including an amplifier placed at one end of the loop [85]. The input signal is split at a 50:50 coupler, and is amplified either at the beginning or at the end of its travel in the loop. This asymmetry induced an intensity dependent phase delay, leading to a large modulation depth even at low input powers. This configuration, shown in Fig. 2.16, has been used extensively. In polarization maintening (PM) fibers, NALMs provide a saturable absorber which is unaffected by its environment, ultrafast, and tunable with via the amplifier found in the loop [86]. The power transfer function of an NALM is

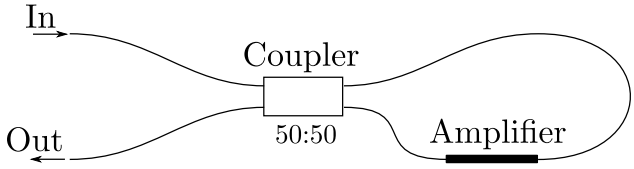

Figure 2.16 – *Schematic of an NALM.*

derived by writing the clockwise and counter-clockwise fields:

$$E_{\mathrm{CW}} = E_{\mathrm{in}}\sqrt{\alpha G}\,\exp(-j\gamma|E_{\mathrm{in}}|^2 L\alpha G)\sqrt{\alpha} = E_{\mathrm{in}}\alpha\sqrt{G}\,\exp(-j\gamma|E_{\mathrm{in}}|^2 L\alpha G) \tag{2.53}$$

$$E_{\mathrm{CCW}} = E_{\mathrm{in}}\sqrt{1-\alpha}\sqrt{G}\,\exp(-j\gamma|E_{\mathrm{in}}|^2 L(1-\alpha)G + j\pi)\sqrt{1-\alpha} \tag{2.54}$$

The coupler has a ratio α, the amplifier a gain factor G, the mirror a length L, and the fiber a nonlinear waveguide parameter γ. The output power is obtained via the sum of Eqs. (2.53) and (2.54), and P_{out} is related to the input signal via Eq. (2.55). The power transfer function of NALMs is depicted in Fig. 2.17.

$$P_{\mathrm{out}} = |E_{\mathrm{in}}|^2\left(1 - 2\alpha(1-\alpha)(1+\cos\left[\gamma|E_{\mathrm{in}}|^2 L(1-\alpha-\alpha G)\right])\right) \tag{2.55}$$

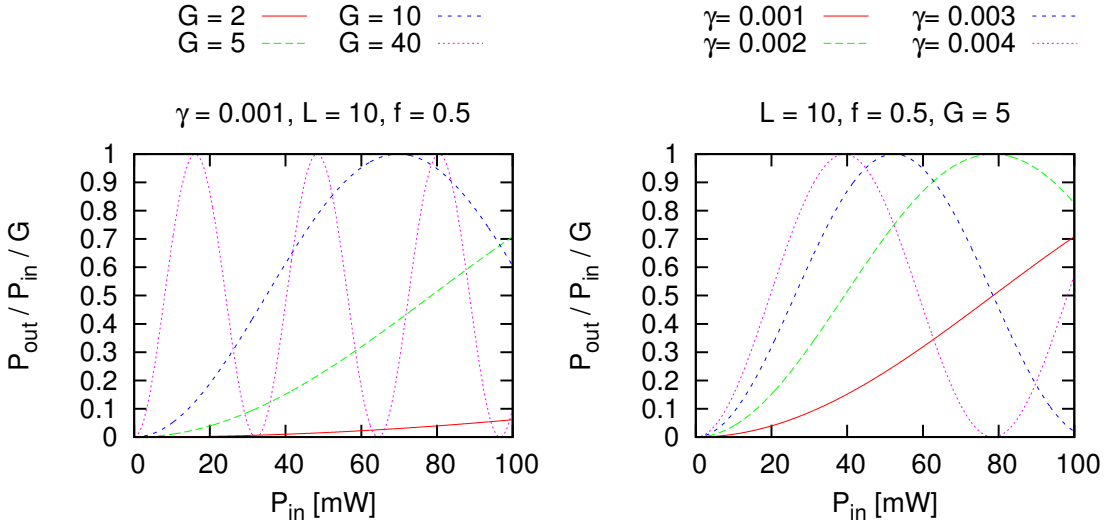

Figure 2.17 – *Power transfer function of a NALM with various gain G (left), and various nonlinear waveguide parameters γ (right).*

For $\alpha \neq 0.5$ and $G = 1$, we fall back to the NOLM. The NALM exploits the nonlinearity of the fiber better than the NOLM, and leads to nonlinear switching for shorter mirror length L.

2.4.2.3 Nonlinear polarization rotation

NPR relies on the intensity-dependent rotation of the polarization in a fiber. All single-mode fibers support two orthogonal modes, which interact together. If not linearly polarized along one

axis, the pulse excites the two orthogonal modes, and interactions may occur. NPR relies on SPM and the effects of XPM between the two linearly polarized eigenmodes, x and y. This effect, first reported by Dahlstrom in 1972 [87], is strong in particular if the birefringence is low. In this case, the group-velocity of the pulse components travel at a similar speed along each polarization axis, and interact by applying an intensity dependent phase shift on each other, as expressed by Eq. (2.56) and Eq. (2.57) [88, 89]:

$$\Phi_x = \left(\beta_x + kn_2\left[|A_x|^2 + \frac{2}{3}|A_y|^2\right]\right)L \tag{2.56}$$

$$\Phi_y = \left(\beta_y + kn_2\left[|A_y|^2 + \frac{2}{3}|A_x|^2\right]\right)L \tag{2.57}$$

In these equations, β_i the propagation constants along axes x and y, k is the free-space propagation constant, n_2 the nonlinear refractive index, and L the length of the nonlinear propagation. The XPM term is responsible for the cross-talk between both polarization axes. The addition of a polarizer after this interaction plays the role of saturable absorber, favoring the parts of the pulse which are best aligned with the polarizer, and attenuating the others. This concept is illustrated in Fig. 2.18. As a function of the polarizer angle, and for various nonlinear phase shifts ϕ_{spm}, the power transfer function of an absorber comprising nonlinear polarization rotation and a linear polarizer is illustrated in Fig. 2.19, and expressed in equation Eq. (2.58) [88].

$$P_{\text{out}} = P_{\text{in}}\sin^2\left[\frac{\phi_{\text{spm}}\cos(2\theta)}{6}\right]\sin^2(2\theta) \tag{2.58}$$

with θ the angle of the polarizer with respect to the reference polarization axis.

The use of tilted Bragg-gratings was recently proposed to replace the polarizer [90].

2.4.2.4 Self-focusing

The intensity dependent refractive index also leads to spatial variations of the effective refractive index across a Gaussian beam propagating in a Kerr medium. In 1962, it was predicted by Askaryan that this gradient of refractive index leads to self-focusing of gaussian beams [91]. Other researchers also reported and studied self-trapping and self-focusing in the next 20 years, theoretically [92–95] and experimentally [96]. It is only in the 90's that the conjunction of self-focusing and aperturing is shown to provide a nonlinear power transfer function that is suitable for the generation of ultrashort pulses [9, 97, 98]. Figure 2.20 illustrates this effect, referred to as

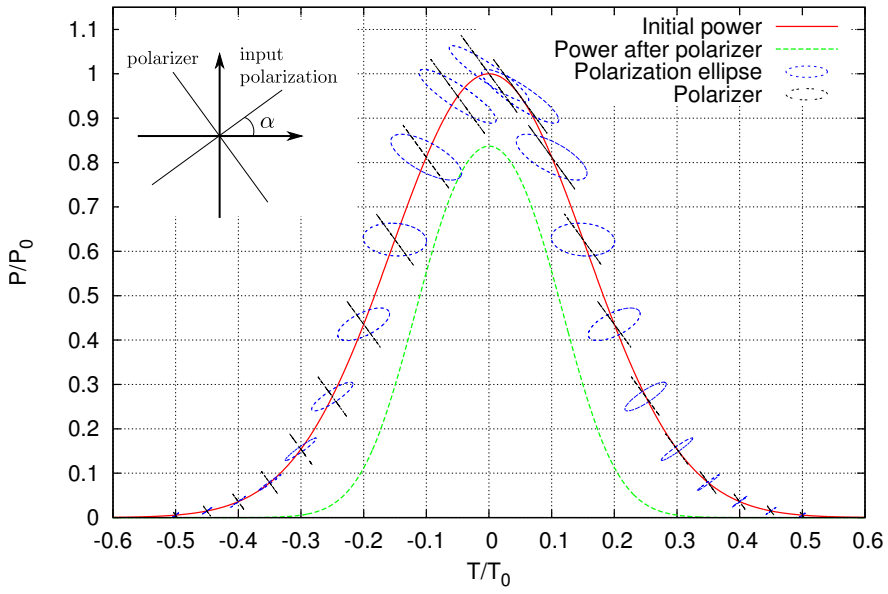

Figure 2.18 – *Illustration of the effect of nonlinear polarization rotation. Given an initial linear polarization of angle α with respect to the x axis, the pulse is sent to a nonlinear medium. By cross-phase modulation, the polarization evolves spatially along the pulse. This pulse passes a polarizer at angle $\alpha + \pi/2$, and results in the green signal, which is shorten in time.*

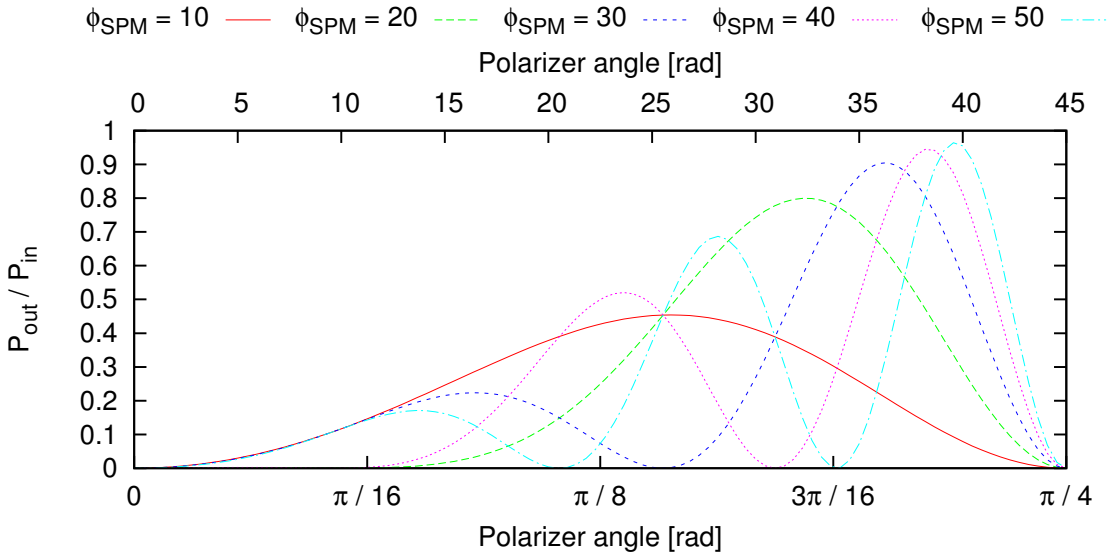

Figure 2.19 – *Power transfer function of NPR followed by a linear polarizer at angle θ, for various nonlinear phase shifts ϕ_{spm}.*

Kerr lens mode-locking (KLM), for an input Gaussian beam propagating in a nonlinear medium. It was observed by Spence et al. [9] and shown by Piché and Salin [99] that aperturing was not

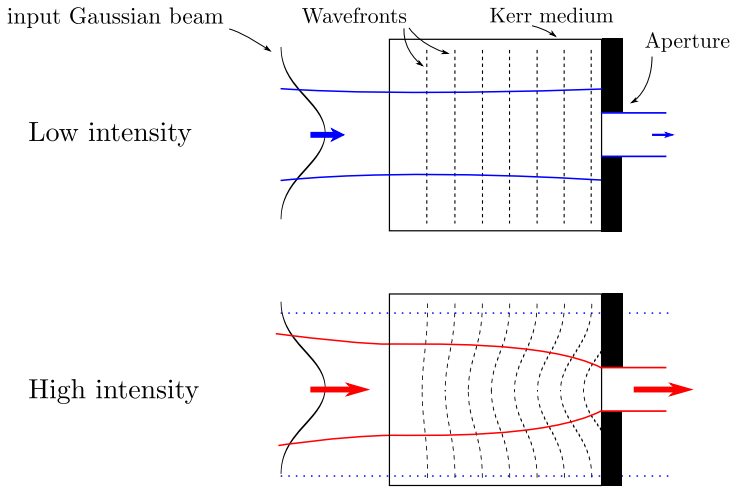

Figure 2.20 – *Self-focusing in a Kerr medium. At low intensity, a low amount of power remains after the aperture (top). At high intensity, self-focusing alters the beam waist, and most power remains after the aperture (bottom).*

required, as the transverse gain profile also favors pulses over CW oscillation.

Few-cycle pulses have been recently reported for such lasers, taking advantage of self-focusing in the amplifying medium, or in air, generating pulses of less than 6 fs [100–102]. KLM is found in free space configurations. Nevertheless, it may be possible to design such a laser with specialty fibers of high nonlinear refractive index coupled to a segment of fiber of different effective mode area.

2.4.2.5 Colliding pulse mode-locking

Fork et al. reported in 1981 a new technique, called colliding pulse mode-locking (CPM), for which the interaction of two counter-propagating pulses in a saturable absorber induces a power dependent attenuation [103]. Before that, the absorber was directly in contact with the mirror, which was technically difficult. Moreover, the pulse synchronization imposed by this technique diminishes instabilities observed in dye-lasers configurations. Pulses shorter than 0.1 ps are obtained with this technique, whereas the use of saturable absorbers, before that, were limited to

the generation of pulses of ∼1 ps. This technique was used recently in semiconductor lasers at ultra-high repetition rates [104, 105].

2.4.2.6 Frequency-comb sources

Mode-locked sources require a fixed phase relationship between its modes. Such a condition is naturally met by stimulated Brillouin scattering (SBS), and Lugovoi and Prokhorov predicted that ultrashort pulses could be generated by taking advantage of Brillouin scattering [106, 107]. Pulses of several nanoseconds were first demonstrated via this concept in 1978 [108]. More recently, picosecond pulses were obtained via several mechanisms, including cascaded-FWM processes in micro-resonators [109, 110], or in the all-fiber configuration of Fig. 2.21 [111]. Due to the Brillouin

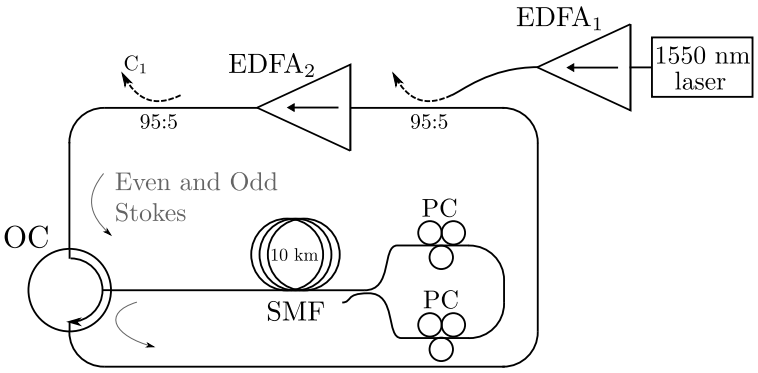

(a) *Even and odd Stokes signals are extracted from the cavity.*

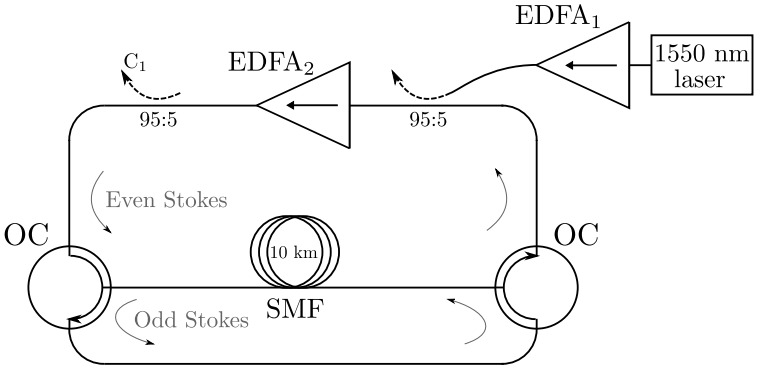

(b) *Only even Stokes contribute to the cavity output, doubling its repetition rate.*

Figure 2.21 – *Setup of the SBS sources. Adapted from [111].*

effect, for a CW signal which propagates in an optical fiber with a sufficient intensity, some of the signal power is transferred into a backwards-propagating wave, with a small frequency offset. This offset is material and wavelength-dependent, for a value of about 10 GHz in silica SMF [112]. The setup of Loranger et al. generates Brillouin lines of multiple orders, forming a frequency comb over about 2 nm [111]. The two configurations of Fig. 2.21 allow the creation a comb containing odd and even Stokes (Fig. 2.21a), or only even Stokes (Fig. 2.21b). Pulses are generated at a repetition rate which corresponds to the frequency spacing between the Stokes lines. The pulse duration is directly related to the spectral width of the comb, and therefore of the number of contributing Stokes lines.

2.4.2.7 Semiconductor saturable absorber

When light is sent to a semiconductor, photons are absorbed and their energy contributes to the displacement of electrons from the valence band to the conduction band. These charge carriers recombine quickly via thermalization and crystal defects [113]. However, when the light intensity increases, electrons accumulate and saturate the conduction band, decreasing the absorption.

Multiple types of semiconductors were used to achieve mode-locking since 1972 [114] with various materials, which recently include carbon nanotubes [115–117] and graphene [118, 119]. Lasers based on these kinds of saturable absorbers require extremely low saturation energy, and can be mode-locked at pulse durations of less than 100 fs [120].

2.4.2.8 Nonlinear mirrors

Another original approach enabling the generation of ultrashort pulses was introduced in 1988 by Stankov and Jethwa [121], with the use of a SHG crystal as presented in Fig. 2.22. The nonlinear power transfer function of this system is composed of the SHG crystal as well as the mirror M2, these components forming the so-called “Stankov mirror” [122]. Light at the pump wavelength of 1.06 µm penetrates the crystal, leading to a weak SHG signal at low pump power. Both the pump and the SHG signal reflect at M2. If the reflected signals are phase-matched, which can be adjusted by tilting the crystal, the pump signal experiences amplification from the SHG signal, as a reverse-SHG process. Therefore, the higher the intensity of the pump beam, the higher the SHG signal, and the higher the amplification of the pump signal [123].

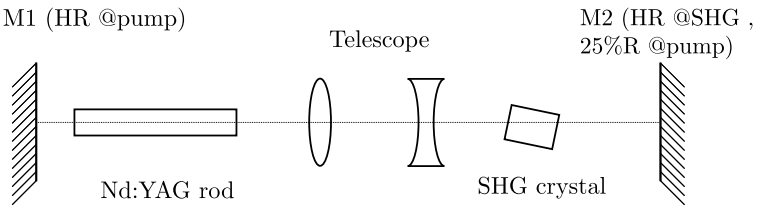

Figure 2.22 – *Cavity configuration: a high reflectivity mirror M1, a Nd:YAG rod, a telescope formed by a pair of lenses, a SHG crystal, and a mirror M2, featuring high reflectivity at the doubled frequency, as well as 25% reflectivity at the pump.*

This concept has been extensively studied, and pulses in the picosecond range were generated [124, 125]. The limiting factor for such an architecture is the group velocity dispersion (GVD)-mismatch between the fundamental and the doubled signals, as well as the phase matching condition. Variants of this technique were also reported, in particular with the use of a Michelson interferometer [126], or with Raman interactions instead of SHG [127, 128]

2.4.2.9 Cascaded second order nonlinearities

In a configuration similar to the one of the nonlinear mirror of Stankov, cascaded second-order mode-locking (CSM) was predicted by DeSalvo et al. in 1992 [129, 130]. CSM takes advantage of the $\chi^{(2)}$ equivalent of the self-focusing effect observed in $\chi^{(3)}$ media, described in Section 2.4.2.4. As for the nonlinear mirror of Stankov, a $\chi^{(2)}$ crystal faces a mirror, this time as reflective for the pump and the SHG signals. A slit is added on the optical path, serving as aperture as for KLM. During the propagation in the crystal, if the phase matching condition is not met, part of the SHG signal is down-converted to the pump frequency, but with a $\pi/2$ phase shift with respect to the pump signal [122]. The resulting wave therefore undergoes an intensity-dependent phase shift, as in $\chi^{(3)}$ nonlinear media [131].

Mode-locked lasers have been designed based on that concept, and pulses in the picosecond range were generated in such cavities [132, 133], which as for the nonlinear mirror suffer from limitations related to the GVD mismatch of the SHG process.

2.4.2.10 Quadratic polarization switching

In quadratic polarization switching (QPS), a type II nonlinear crystal is used to generate cascaded second order nonlinearities, as for CSM. It was shown that a linearly polarized field sent to such a crystal can yield to an intensity dependent output polarization [134]. Phase-matching conditions must be satisfied, and the field must unequally excite the ordinary and extraordinary components of the crystal. In this case, the SHG process turns into difference frequency generation between the fundamental field and its second harmonic, and the emitted field at the fundamental frequency acquires a π phase shift [135]. The polarization state therefore remains linear, but rotates by an angle which is intensity-dependent. A polarizer, as for NPR, transforms the polarization rotation into amplitude modulation. Pulses of 2.8 ps were obtained initially by Couderc et al. [135], and the same group achieved a reduction of the pulse duration down to 195 fs two years later [136].

2.4.2.11 Other mode-locking techniques or variants

Mode-locking was achieved with other techniques which are not detailed here, because the generated pulses are longer than the picosecond.

- Spence et al. reported that SRS could be used for mode-locking in fiber lasers [137, 138]. To date, no experimental confirmation of this technique was reported.
- A saturable Bragg reflector was introduced by Tsuda et al.[139]. It includes a semiconductor structure, and is therefore part of the semiconductor saturable absorbers [120].

2.4.3 Mode-locking of fiber lasers: the influence of GVD

In an attempt to achieve shorter and shorter pulse duration in passively mode-locked lasers, it was noticed that the influence of GVD was essential [140]. Fork et al. pointed out in 1984 that pairs of prisms could have negative GVD, and hence compensate for other components in free-space setups [141]. Moreover, the “Haus master equation”, reported in 1991, models the evolution of a weakly perturbed pulse in a laser cavity and concluded that highly chirped pulses could be sustained in the normal dispersion regime [83, 142]. In the case of anomalous dispersion, however, the pulse is a soliton, sustained by the balanced effects of GVD and SPM.

2.4.3.1 Solitonic and stretched pulse regime

When a laser cavity is made of components operating in the anomalous dispersion regime, solitons are generated and sustained in the laser cavity. Their profile is therefore a hyperbolic secant. As they propagate, these solitons are perturbed by the gain and losses encountered while travelling in the cavity. As a consequence of these changes in shape, the soliton radiates energy under the form of dispersive waves. Because the soliton undergoes nonlinearity, contrary to the dispersive waves, it experiences a continuous phase shift, and is therefore periodically phase-matched with the dispersive waves. The laser spectrum acquires sidebands, first explained by Kelly [143], which drain energy out of the soliton, and therefore limit its energy.

2.4.3.2 All-normal dispersion regimes

In average normal chromatic dispersion, fiber lasers also generate ultrashort pulses. The usual interplay between chromatic dispersion and SPM, contributing to the ignition of solitons, can not operate in normal dispersion. Mode-locking in particular was demonstrated when the cavity net dispersion was normal, but close to zero: in this case, the pulse sees an effective net anomalous dispersion [82]. The interest of such lasers lies in the fact that pulses are Gaussian only up to –10 dB from their peak power, and their slope is more abrupt after that. Even in the presence of dispersion changes, the pulses do not radiate, and no Kelly sidebands are generated. Later, Zhao et al. reported an all-normal dispersion laser designed with all-normal dispersion fibers [144]. So-called “gain-guided solitons” are formed in such cavities: they are sustained by nonlinearities, gain filtering, and the cavity transmission [145]. A steady state is found, such that the propagating soliton is linearly chirped. Its temporal duration increases during the propagation in normal-dispersion fibers, but decreases at the polarizer. Pulsed operation is enabled by an adjustment of the polarization controllers (PCs), and the required pump power is higher than for mode-locked lasers in solitonic regime. Nevertheless, gain-guided solitons carry a large amount of power in the absence of Kelly sidebands, and the intracavity pulse peak power remains low, as the pulse is highly chirped. High peak powers and femtosecond pulse duration can be obtained after dispersion compensation.

2.4.4 Self-similar pulses

By taking advantage of the gain medium, it is possible to generate pulses that are self-similar, which means that their normalized temporal profile is unchanged during propagation in the amplifying medium [146]. It is the case of parabolic pulses, which are also referred to as "similaritons". As they propagate, self-similar pulses grow in temporal duration and peak power. At the same time, their spectral bandwidth increases, without generating sidebands contrary to pulses which undergo wavebreaking during propagation in normal dispersion. These pulses therefore carry a large amount of energy, and their linear chirp enables compression by dispersion compensation. Lasers including self-similar propagation have been proposed recently [86, 147–149].

2.4.5 The noiselike pulse regime

Horowitz et al. reported in 1997 that fiber lasers mode-locked by NPR could enter another kind of regime, which they called "noiselike", because the autocorrelation figure of the observed pulses was typical of the intensity autocorrelation of a noisy pattern of picosecond duration [18]. Moreover, the acquired spectrum of such pulses is very smooth and spreads over tens of nanometers. Their autocorrelation figure is composed of a sharp peak with a duration of about a hundred femtoseconds, superimposed to a Gaussian whose maxima stands at 50% of the peak SHG power. In the time-domain, therefore, fast varying oscillations in the femtosecond range are confined in a pulse envelope of several picoseconds.

In their first paper, Horowitz et al. also suggest that in this operation regime, the pulse-to-pulse changes are significant and indicates that the locking of the modes is therefore only partial, as suggested by numerical simulations.

If their investigation included only cavities in average anomalous chromatic dispersion, it was shown later than this NLP regime could also be sustained in cavities of average normal dispersion [144]. In this case, the cavity does not support the propagation of solitons, and the pulse is only shaped by the gain provided. In this case, by the erbium fiber of the cavity, forming a so-called "gain-guided soliton", as described in Section 2.4.3.2. Tang et al. explain the process of noiselike pulse generation in cavities with anomalous dispersion [150]. As the gain in the cavity is increased, the circulating soliton experiences positive feedback in the cavity, increasing its peak power. At some threshold, the increase of the soliton peak power decreases the cavity

transmission, hence inducing negative feedback. From this point, increasing the laser gain only amplifies the dispersive waves and soliton background. Their interference with the actual pulse leads to noiselike pulse generation [151].

2.4.6 Cascaded regeneration

In this section, the SPM-OF regenerator is introduced. This component constitutes a basic block of regenerative laser sources, which are the subject of Chapter 4.

2.4.6.1 The SPM-OF regenerator

Developed with communications systems in mind in 1998, the SPM-OF regenerator, depicted in Fig. 2.23, is an optical setup that aims at improving the signal over noise ratio (SNR) which tends to decrease with increasing propagation distances [152]. Distortions occur as a result of processing operations such as reamplification, switching or demultiplexing. The SPM-OF regenerator is composed of two main components: a HNLF, preferably featuring normal dispersion, and a band-pass filter (BPF). During propagation in the HNLF, the signal undergoes SPM, which results in an intensity dependent spectral broadening. A BPF, spectrally offset with respect to the central wavelength ω_0. The output intensity of the signal is related to the spectral distance $\Delta\omega_{\text{shift}}$ between the signal and the filter with a nonlinear power transfer function. Low intensity fluctuations are filtered out (logical zeros), for they do not undergo any spectral broadening, while pulses of sufficient intensity are kept (logical ones). The output pulses are essentially transform-limited.

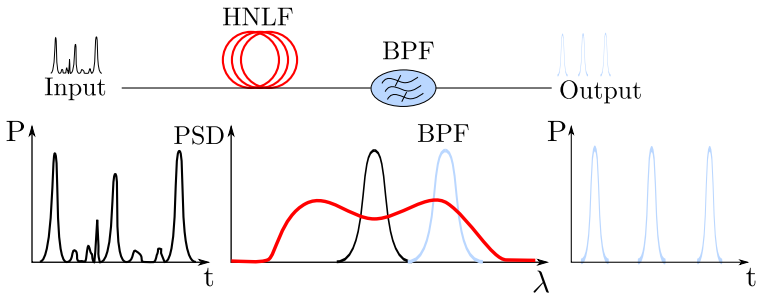

Figure 2.23 – *Schematic of a SPM-OF regenerator.*

Taking into account SPM only, the spectral bandwidth of the broadened pulse is [152]:

$$\Delta\omega_{\text{SPM}} = \Delta\omega_0 \frac{2\pi}{\lambda} n_2 I_p L \tag{2.59}$$

where $\Delta\omega_0$ is the pulse bandwidth. for pulses of various intensities I_p, a nonlinear refractive index n_2, a central wavelength λ and a nonlinear medium of length L. The pulse is rejected by the filter if $\omega_{\text{SPM}}/2 < \Delta\omega_{\text{shift}}$, and passes otherwise.

The pulses after regeneration are close to their transform limit, therefore the intensity of the output pulse intensity I_ω is proportional to the power spectral density (PSD) of the input signal, and one can write :

$$I_\omega \sim \frac{dI}{d\omega} \equiv \frac{I_p}{\Delta\omega_{\text{SPM}}} \tag{2.60}$$

Using Eq. (2.60) in Eq. (2.59),

$$I_\omega \sim \frac{I_p}{\Delta\omega_{\text{SPM}}} = \lambda^{-1} \Delta\omega_0 2\pi n_2 L \tag{2.61}$$

and surprisingly the output intensity is independent of the input intensity. The SPM-OF regenerator therefore equalizes the level of the output signal.

In two different configurations, the power transfer function is depicted in Fig. 2.24. It can be noted signals passing through such a generator experience a loss of about 10 dB.

P.V. Mamyshev also suggests the use of two regenerators in cascade, which flattens the power transfer function, and resets the signal to its initial wavelength. The insertion of amplifiers between each regeneration stage forms a reshaping and reamplification (2R) regenerator as illustrated in Fig. 2.25.

In conclusion, the SPM-OF regenerator is a simple all-optical regeneration system which lowers the amplitude fluctuations and operates at any signal bitrate, because of the quasi-instantaneous response of the Kerr effect. Analysis of the properties of SPM-OF regenerators have been conducted by several groups, and it was shown that 2R regenerators improve the overall bit error ratio (BER) [153], could operate with specialty fibers such as chalcogenide for compactness [154], and could take advantage of design rules to optimize their operation [155–157]. The generation of pulses from an incoherent wave with a series of cascaded regenerators was also investigated [149, 158].

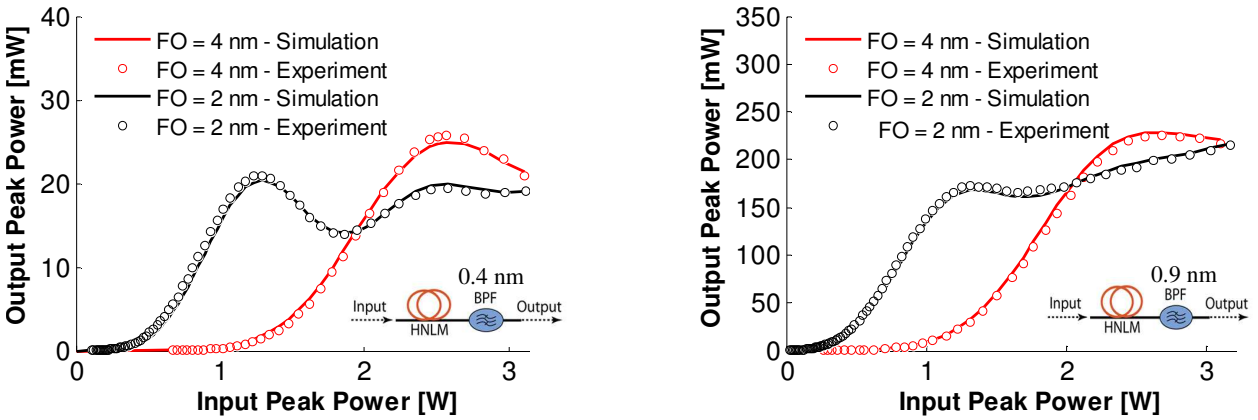

Figure 2.24 – *Power transfer function of a SPM-OF regenerator with filters of 0.4 nm and 0.9 nm bandwidth, and a filter offset of 2 and 4 nm. From [16], reproduced with permission.. FO: filter offset.*

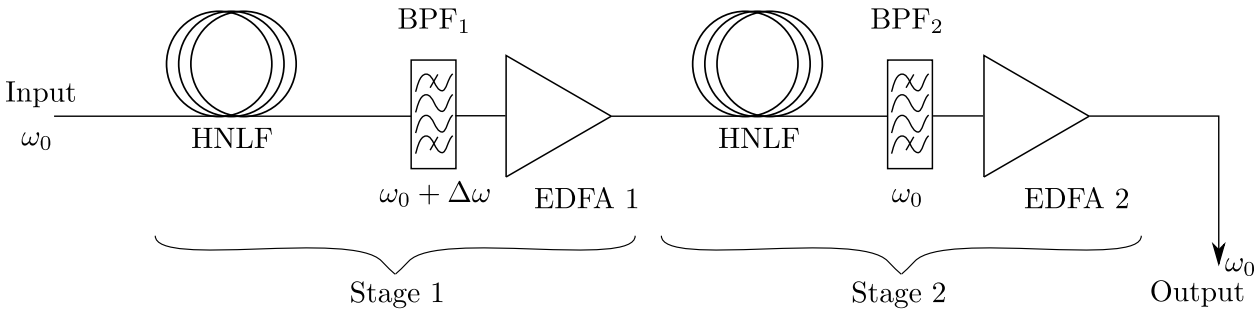

Figure 2.25 – *SPM-OF 2R regenerator.*

2.5 Summary

Figure 2.26 depicts the first apparition of each self-pulsating source described in Section 2.4: the top part of the figure lists the date of proposition for each pulse generation technique, while the bottom part of the figure represents the output pulse temporal duration and repetition rate. With this representation, free-space and fiber lasers are clearly separated, with the exception of the frequency-comb SBS laser, that operates at a high frequency > 10 GHz. Obviously, the criteria of pulse duration and repetition rate do not fully highlight all properties of pulses generated by these laser architectures, since for instance regenerative sources are aperiodic and support more than a single pulse in their cavity. Nevertheless, this representation enables quick comparisons between these techniques of pulse ignition. Table 2.2 summarizes these techniques and provides the appropriate references. Generally, fiber lasers operate at lower repetition rates because of the significant length of fibers required for each component, contrary to free-space setups that are more delicate, but compact. The pulse duration is often limited by the chromatic dispersion in the laser, which again is often harder to compensate in all-fiber cavities. Nevertheless, setups taking advantage of $\chi^{(3)}$ nonlinearity usually require low input pump power to trigger the pulsed regime.

In this thesis, fiber lasers are designed in cavities exceeding 1 km, because silica HNLFs are required to trigger pulses. The output pulse duration is nevertheless short, despite a kHz repetition rate.

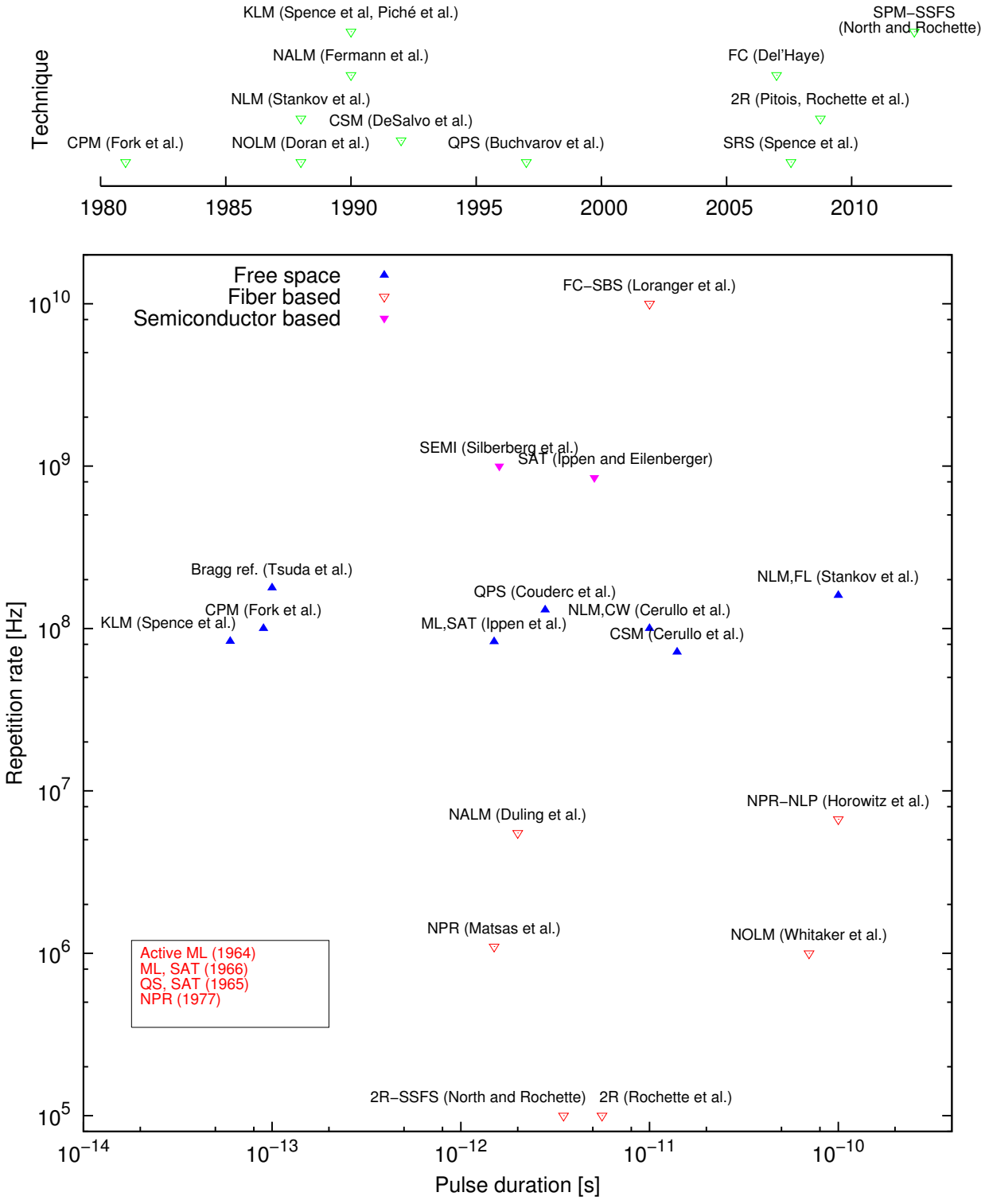

Figure 2.26 – *Techniques for the generation of ultrashort pulses. Top: Prediction or first demonstration. Bottom: Pulse duration and repetition rate reported or inferred.*

Technique description (1980 –)	Author and reference
CPM (1981)	Colliding pulse mode-locking (Fork et al.) [103]
NLM (1988)	Nonlinear mirror (Stankov et al.) [123]
NOLM (1988)	Nonlinear optical loop mirror (Doran et al.) [84]
NALM (1990)	Nonlinear amplifying loop mirror (Fermann et al.) [85]
KLM (1990)	Kerr-lens mode-locking (Spence et al., Piché et al.) [9, 97]
CSM (1992)	Cascaded second-order mode-locking (DeSalvo et al.) [129]
QPS (1997)	Quadratic polarization switching (Buchvarov et al.) [134]
FC (2007)	Frequency comb source (Del'Haye et al.) [109]
SRS (2007)	Mode-locking w/ stimulated Raman scattering (Spence et al.) [137]
2R (2008)	Cascaded 2R regeneration (Pitois et al. [149], Rochette et al. [17])
Experiment name and author	**Description**
Active ML (Hargrove et al., 1964)	Mode-locking via intracavity modulations [78]
QS, SAT (Hercher et al., 1965)	Single-mode operation, Q-switched ruby laser [159]
ML, SAT (DeMaria et al., 1966)	Mode-locking with a bleachable dye [160]
ML, SAT (Ippen et al.,1972)	Passive-locking with a saturable absorber, single-pulse operation [114]
ML, NPR (Sala et al., 1977)	Mode-locking via NPR in free-space [161]
SEMI (Silberberg et al., 1984)	Passive mode-locking with a semiconductor saturable absorber [162]
NLM, FL (Stankov et al., 1988)	Nonlinear mirror, pumped by a flash lamp [121]
NOLM (Whitaker et al., 1990)	Mode-locking with an NOLM [163]
KLM (Spence et al., 1991)	Kerr lens mode-locking without aperturing [9]
NALM (Duling et al., 1991)	Mode-locking via an all-fiber amplifying loop mirror [164]
NPR (Matsas et al., 1992)	Mode-locking via NPR in a fiber laser [165]
NLM, CW (Cerullo et al., 1994)	Mode-locking via a nonlinear mirror, pumped by a CW [166]
Bragg ref. (Tsuda et al., 1995)	Saturable Bragg reflector[139]
CSM (Cerullo et al., 1995)	Cascaded second-order mode-locking [132]
NPR-NLP (Horowitz et al., 1997)	Noiselike pulse generation in a fiber laser [18]
QPS (Couderc et al., 1999)	Mode-locking with QPS [135].
2R (Rochette et al., 2008)	Pulse generation via cascaded 2R regeneration [17]
SSFS-2R (North and Rochette, 2012)	Pulse generation via SPM and SSFS [22]
FC-SBS (Loranger et al., 2012)	Frequency comb source via SBS [111]

Table 2.2 – *Summary of the techniques for pulse generation in free space and fiber lasers.*

Chapter 3

A tool for simulating pulse propagation

In order to have a good understanding of the underlying mechanism of pulsed lasers, their simulation with a numerical model is absolutely essential. Even without a perfect model, a good match between experiments and simulations can be achieved. The temporal duration, spectral features, and energy of the circulating pulses can thus match the measured data and illustrate the complex behaviour of nonlinear systems. Laser architectures, including a fast saturable absorber as a trigger for mode-locking in a resonator, are well described by the master equation introduced by Haus et al. in 1991 [142]. Although very convenient for providing analytical solutions for the steady-state of pulses circulating in optical cavities, the master equation is subject to approximations that do not always hold. It is therefore usual to employ numerical methods to solve the differential equations describing the propagation of optical pulses in optical fibers, especially when the nonlinear effects play an import role. Other kinds of pulsed lasers, including the ones presented in Chapters 4 and 5, can not be modelled with the master equation, and numerical methods are required to describe the propagation of pulses. To achieve this, the GNLSE of Eq. (3.1) is generally solved with the split-step Fourier method [38], which integrates separately the dispersive terms, that are linear, and the nonlinear terms.

$$\begin{aligned} &\frac{\partial A}{\partial z} + \frac{\alpha}{2} - \frac{i}{2}\beta_2 \frac{\partial^2 A}{\partial T^2} + \frac{1}{6}\beta_3 \frac{\partial^3}{\partial T^3} \\ &= i\gamma \left(|A|^2 A + \frac{i}{\omega_0} \frac{\partial}{\partial T}(|A|^2 A) - T_R A \frac{\partial |A|^2}{\partial T} \right) \end{aligned} \tag{3.1}$$

The nonlinear term is evaluated in the time-domain, while the dispersive terms are computed

in the frequency domain via the use of a Fourier transform. More recently, a Runge-Kutta method of order 4 was demonstrated to solve the GNLSE with a better accuracy [167].

The simulation of pulse propagation in optical fibers is widespread for the study of nonlinear phenomenon such as SC generation as well as the study of mixing effects in communications systems, for example. Numerical methods are used to model pulses circulating in laser cavities, and provide a good model of DM solitons. However, a large number of numerical evaluations of the GNLSE have to be achieved. In order for the solution of these equations to converge, the time spent in the simulation of each propagation in an optical fiber can be of several minutes. For instance, it was reported recently that the simulation of the formation and propagation of noiselike pulses, wave-packets of several picoseconds containing fast and random oscillations in the femtosecond range, could require 48 hours for 2000 cavity round-trips [168]. Other kinds of pulsed laser cavities based on optical regeneration suffer from similar problems [22]. The large amount of nonlinearity required to trigger pulses are also demanding in terms of computational power, and the analysis of such lasers can take days or even months, to be completed, especially when higher order nonlinear effects are included. Fortunately, the numerical solution of the GNLSE can be paralleled to a certain extent. Even though the step-by-step propagation through the nonlinear medium is inherently sequential, all operations from one step to another can be paralleled either because they are element-wise computations, or because they are Fourier transforms. A solver for the multidimensional nonlinear Schrödinger equation was reported for Matlab including a serial and a graphics processing unit (GPU)-based implementation of the Runge-Kutta of order 4 method [169]. Several papers report speedups obtained by the implementation of the SSFS on a GPU [170–172].

For this thesis, a portable simulator, inspired by [173], was specifically designed for pulsed laser cavities. It is written in Python and takes advantage of numerous packages, such as Reikna [174], PyOpenCL [175], PyTables [176], Numpy [177], and SciPy [178], among others.

3.1 Design and implementation

Python was chosen as main language for its simplicity and the availability of numerous scientific packages. The program is object-oriented, usable interactively from an IPython shell [179], from a description file, or via a monitoring graphical user interface (GUI). Each optical component is described in a Python object, and inherits from methods of a `Device` class.

3.1.1 Optical components

The simulator implements several optical components. The propagation inside nonlinear fibers is implemented on the central processing unit (CPU) and on the GPU, with both the SSFS and the Runge-Kutta in the interaction picture (RK4IP) methods. The SSFS method is implemented with a fixed step size h, and also implements a system of coupled equations that allow the modelling of the two orthogonal polarization states of an optical fiber. The global error of the SSFS method is second-order in the step size, $O(h^2)$. The RK4IP method, however, is implemented with an adaptive step size, in order to provide a lower-bound to the error in between each spatial step h [180]. Its convergence is fourth-order accurate $O(h^4)$ [167].

Single-mode fibers can be described easily from their main characteristics: their nonlinearity in $\mathrm{W^{-1}\,m^{-1}}$, the second- and third order dispersion parameters β_2 and β_3 in $\mathrm{ps\,nm^{-1}\,km^{-1}}$ and $\mathrm{ps\,nm^{-2}\,km^{-1}}$, their length L in meters, and their attenuation α_{dB} in $\mathrm{dB\,m^{-1}}$. Optionally, the self-steepening effect can be included, as well as the Raman effect via a constant T_R in fs. It is also possible to replace the dispersion constants with a dispersion curve specifying $\beta_2(\omega)$, or to include a wavelength-dependent transmission. The method to use, as well as its implementation can be specified for each fiber. For visualization purposes, the pulse profile at each spatial step or at a custom series of steps can be saved to a hierarchical data format (HDF) file [181].

Band-pass filters compute the transmission of an input signal in the frequency domain via a fast Fourier transform (FFT), computed on the CPU. A Python wrapper, anfft, uses the multi-threaded FFTW [182] library. Gaussian or custom filter profiles can be specified via an external file. A fixed or user-defined wavelength shifting can be provided by the means of a `lambda` function related to the current cavity-round trip.

A time-domain filter is also implemented. It is especially useful when visualizing the spectrum of a given pulse in the simulation's temporal window in presence of other pulses, inducing a beating in the spectral domain. The filter can be temporally fixed, or follow the peak power of the temporal signal. Its shape is super-Gaussian with a custom order.

Erbium and thulium doped amplifiers are provided, with a simple yet satisfactory implementation, relating the input power P_{in} to the output power P_{out} via Eq. (4.2).

Other components relative to polarization are available: a linear polarizer with a custom angle with respect to the principal axis, a polarization retarder, inducing a delay to the principal axis, and a polarization rotator [41]. Pulses or custom data sources can be specified as a seed for the

simulated setup.

3.1.2 GPU implementation

The program relies on PyOpenCL to compile and run kernels on the GPU. Another abstraction layer, reikna [175], provides an efficient paralleled FFT implementation, and type abstractions. FFTs and element-wise operations on complex numbers can therefore be written in C, plus some specific syntax dealing with the data type. The computations are fully executed on the GPU, and does not move data to and from the CPU, an operation which is extremely time consuming.

In Fig. 3.1, a comparison is made between the speed provided by the CPU and GPU implementations of the RK4IP and the split-step Fourier method. The graphic card used in this comparison is a Nvidia GeForce GTX 470, and the host computer an Intel i7 quad-core, 2.80 GHz. This graphic card is not designed to efficiently handle double-precision operations, which explains the limited speedup observed when using full precision. Two CPU implementations are available. The first one is written in pure Python/NumPy, whereas the second one takes advantage of the numexpr virtual machine. The pure Python/NumPy CPU implementation is serial, except for the FFTs, which are handled by FFTW. The main penalty of this implementation is the creation of temporaries during elementwise operations [183]. Numexpr [1] is a just-in-time compiler, which parallelizes elementwise expressions, and avoids the creation of temporaries. The time taken in that process, however, has a limited effect and can be estimated by comparing the efficiency of the CPU implementation and the CPU-numexpr one: the speedup does not exceed a factor of two. Most of the time is spent in computing Fourier transforms, which is $O(n \log n)$.

3.1.3 The Python user interface

The simulation software can be used programmatically. Defining a setup to simulate is done in the following order: 1) an instance of the `Gparam()` class is created, and the simulation time and frequency steps are defined. 2) Components are created as instances of their respective class, and their parameters as set. 3) Components are linked together with their `set_input()` method. Finally, each component is run by executing its `run()` method.

1. Available at https://github.com/pydata/numexpr under the MIT license.

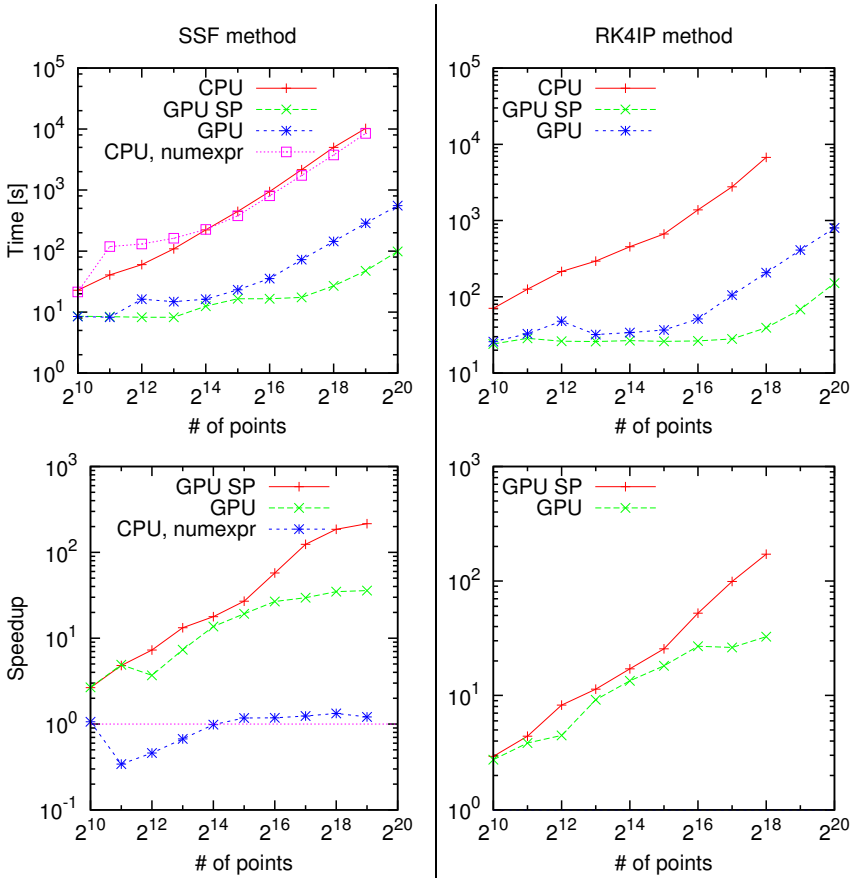

Figure 3.1 – *Execution time for the propagation of a soliton experiencing fission in a HNLF. Left: Split-step Fourier method, fixed step size. Right: Runge-Kutta method, adaptive step size. SP: single-precision operations, RK4IP: Runge-Kutta in the interaction picture method, SSF: split-step Fourier.*

The following code snippet simulates the nonlinear compression of a picosecond pulse. Three components are initialized: an initial pulse of 25 ps, a nonlinear fiber in normal dispersion, and purely dispersive fiber. Spectral broadening occurs due to the conjugated effects of SPM and dispersion, adding a quasi-linear chirp to the pulse. By compensation of the dispersion, the pulse is recompressed to less than 1 ps.

3.1.4 The text-based setup description

Another way to describe an experimental setup is by the creation of a configuration file. Its simple syntax is similar to the one of INI files, and includes sections containing `key = value` keywords. The `params` section is mandatory, and provides information about the simulation time and frequency vectors. It is in fact directly linked with the previously mentioned `Gparam` class. Each optical component is described in a section, and pairs of key and values provide the required simulation parameters. Values are evaluated by the Python interpreter, and can therefore be `lambdas` or expanded computations. An optical device can specify its input as the output of another component, and an initial seed to the simulation can be provided in a different section, with a target device. The program is executed via a parser that reads the configuration file, and connects the components. Only one cycle, detected with Tarjan's strongly connected components algorithm is allowed in the device graph [184]. A Breadth-first tree traversal is computed, and each device is executed sequentially. Devices and their children, that do not belong to the main cycle, can be executed in parallel.

The components described via the text interface of are simulated, started from the `seed`, and the simulated graph can be visualized as depicted in Fig. 3.2. Details regarding the code required for this experiment is available in Appendix A.1.

3.1.5 Supervision user interface

In order to monitor long simulations, a Python-based interface was written, and the simulator presented in this chapter was improved. During the simulation, the object corresponding to each device is sent via a socket to a monitoring interface, if the latter is running. Multiple simulations, running in parallel, can be monitored from this interface, and the input and output temporal and spectral graphs are readily available. Moreover, spectrograms can be computed directly from these

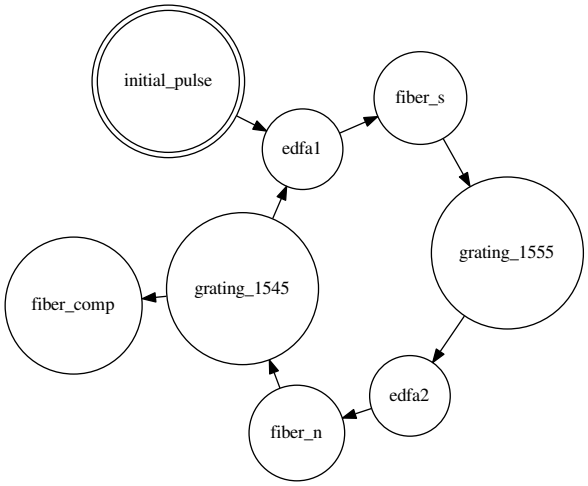

Figure 3.2 – *Graph of the simulated setup.*

results, independently of the state of the simulation. Figure 3.3 illustrates the user interface of this program, based on PyQtGraph.

In order to obtain decent performances and minimize the network traffic, the Blosc compressor is used. A patch was written to enable concurrency for the Blosc library, which was not re-entrant [2].

3.2 Conclusion

In summary, a flexible software to simulate pulse propagation in nonlinear cavities was presented. By exploiting the capabilities of GPUs, a typical speedup of 20× facilitates the modelling of complex setups. A unified and independent interface permits on-the-fly data visualization from simulations running on different physical computers. The program is written in Python, and relies on free software libraries, thus permitting its use on different computing platforms without licensing costs. A simulations presented in the next chapter take advantage of this software, and have required a computing ranging from a few seconds to several days, when a large number of cavity round-trips was required to reach a steady-state.

2. The corresponding patch was integrated upstream, from pull request #16: https://github.com/FrancescAlted/blosc/pull/16

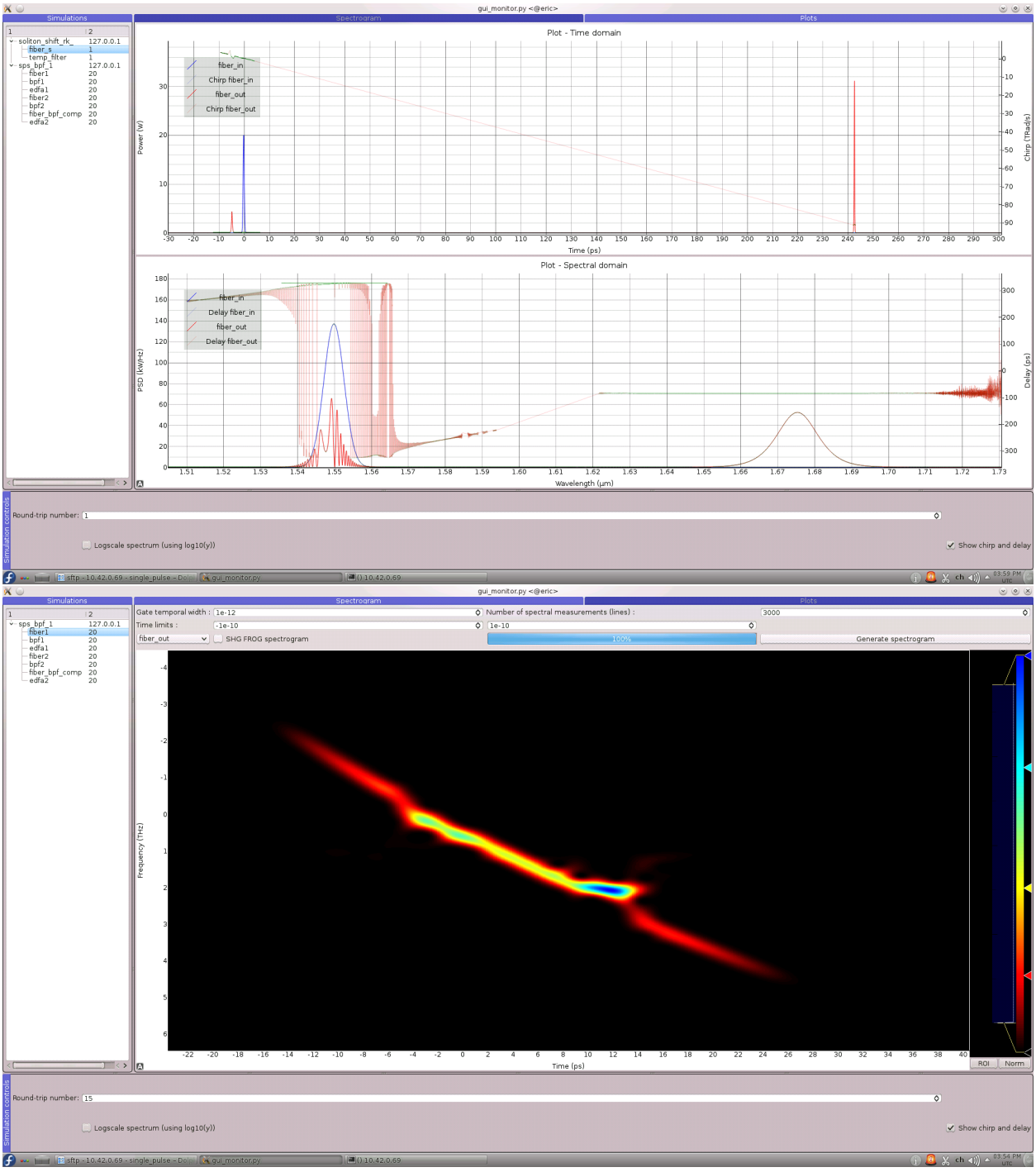

Figure 3.3 – *Top: temporal and spectral illustration of SSFS. Bottom: spectrogram of a pulse from the source of Chapter 4.*

Chapter 4

Regenerative SPM sources

4.1 Introduction

Self-pulsating sources based on cascaded regeneration are a new alternative to conventional mode-locked sources mainly based on saturable absorption via APM. Designs of fiber mode-locked sources feature this mode-locking technique most of the time, and other kinds of lasers take advantage of semiconductor saturable absorbers [83, 113], defining a fixed phase relationship between the propagating modes. Sources based on cascaded regeneration, however, do not allow a phase-locked laser oscillation as described in Section 2.4.2, but rather converge towards the propagation of a so-called "eigenpulse", which undergoes periodic changes in its profile and spectrum and is regenerated after every cavity round-trip [17]. Regenerative sources have three main operation regimes. In the degenerate case, the source outputs a CW signal. Otherwise, the source spontaneously generates pulses from noise in a self-pulsating (SP) regime, or sustain existing pulses in the pulse-buffering (PB) regime. Unlike conventional mode-locked sources, regenerative sources support the propagation of ultrashort pulses even in cavities as large as $\sim 2\,\mathrm{km}$, they are insensitive to polarization and can sustain one or more pulses in their cavity. Incidentally, the architecture of regenerative sources directly enables nonlinear pulse compression at its output from the SPM broadened pulse spectrum [16]. Furthermore, it was shown in [16] that the experimental behavior of this cavity configuration was well predicted by numerical models.

Optimization rules for 2R regenerators were reported previously [153, 155–157, 185], and a theoretical study of cascaded 2R regenerators was performed by Pitois et al. [149, 158]. In

the latter references, the authors describe the evolution of noise and pulses that are inputed to cascaded regenerators with controlled amounts of chromatic dispersion, nonlinearity and filter offset. In contrast with the regenerator cascade of [149], a self-pulsating source based on cascaded regenerators takes advantage of the saturable nature of the amplifiers in order to determine the dynamics of pulse propagation.

In this chapter, the ignition conditions of self-pulsating sources are investigated numerically in the SP regime for filter spectral bandwidth between 0.1 nm to 4 nm and adequate filter offsets. We also describe the source operation in PB regime, and show the importance of chromatic dispersion to ensure stability. Finally, an experimental implementation of regenerative sources operating at large filter bandwidth is presented. In such configurations, the pulse energy is maximized, while their temporal duration remains as short as 2 ps. The limit case of a pair of high- and low-pass filters is experimentally tested, and compared with simulations.

4.2 Operation principle of regenerative sources

In this section, the steady-state operation as well as the pulse ignition in regenerative sources is introduced.

Figure 4.1(a) illustrates paired regenerators $R_{1,2}$ in a closed loop, composed of two HNLFs with normal dispersion, two tunable band-pass filters, and two erbium-doped fiber amplifiers (EDFAs). The numerical model used in this work is based on experimental values reported in [16]. For simplicity, the modelled setup is symmetrical and both HNLFs have the same parameters: a constant waveguide nonlinear coefficient $\gamma = 12.5\,\mathrm{W^{-1}\,km^{-1}}$, a variable chromatic dispersion coefficient D in $\mathrm{ps\,nm^{-1}\,km^{-1}}$, a fixed dispersion slope $S = 0.0074$ ps/(nm^2·km), a fixed loss $\alpha = 1.86\,\mathrm{dB\,km^{-1}}$ and a fixed length $L = 1007$ m. The EDFAs are characterized by an unsaturated gain G_0 and a saturation power P_{sat}. They also contain an isolator to ensure unidirectional operation. The band-pass filters BPF$_1$ and BPF$_2$ are spectrally centered at $\lambda_{1,2}$ with a FWHM bandwidth $\Omega_{1,2}$. The spectral offset between BPF$_1$ and BPF$_2$ is $\lambda_1 - \lambda_2 = \Delta$. Figure 4.1(b) depicts the main spectral features of the source at their operation wavelengths λ_1 and λ_2. Pulses propagating in HNLF$_1$ at λ_2 undergo spectral broadening by the conjugated effects of SPM and dispersion. After filtering at BPF$_1$ and reamplification a similar spectral broadening is experienced by pulses in HNLF$_2$, and finally BPF$_2$ reestablished λ_2 as the central wavelength for the next cavity round-trip. In Fig. 4.2 (a) and (b), the

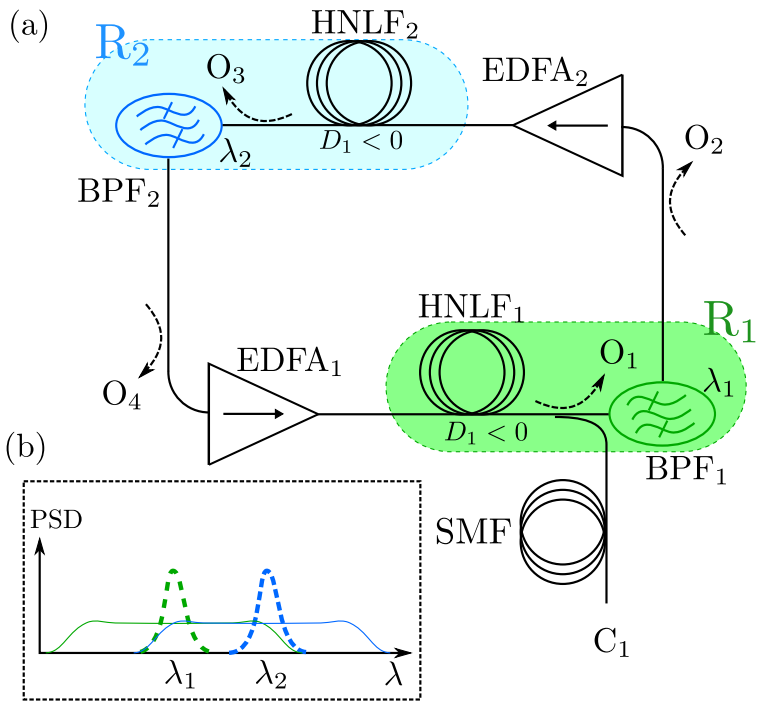

Figure 4.1 – *Source setup: (a) paired regenerators in closed loop, (b) SPM broadening and offset filtering.*

temporal and spectral power profile of an eigenpulse is shown as a function of the propagation distance. During propagation in the HNLF, the pulse broadens in the first 300 m and then acquires a pedestal. Its final FWHM duration is 10× higher than its initial duration. Spectrally, oscillations due to SPM build up in the first 200 m. The conjugated effects of SPM and dispersion then flatten the central part of the spectrum, and transfer energy towards its edges. Figure 4.2 (c) presents the process of pulse generation from ASE. At each cavity round-trip, pulses are shaped from noisy components of high intensities, and the background diminishes for intensities below the threshold of SPM-OF regenerators.

The source is observed at outputs O_{1-4}, and after nonlinear compression at C_1. Figure 4.3 is an experimental FROG spectrogram of the source output at O_2, depicting a chirped pulse at the output of a BPF of 1 nm of bandwidth.

Regenerative sources naturally provide a convenient architecture for nonlinear pulse compression [186]. After the HNLF in normal dispersion, the eigenpulses undergo a large amount of chirp and spread temporally and spectrally by SPM, with a decreasing peak power. Amplification can be achieved without the interference of nonlinear effects due to high peak powers. With the addition of a segment of dispersive fiber, a chirp of opposite sign compresses the amplified pulse, whose bandwidth is largely increased by SPM. Such a pulse is shown in Fig. 4.4.

4.2.1 Numerical model

Propagation through all segments of fiber is described by the nonlinear Schrödinger equation,

$$\begin{aligned} &\frac{\partial A}{\partial z} + \frac{\alpha A}{2} - \frac{i}{2}\beta_2 \frac{\partial^2 A}{\partial T^2} + \frac{1}{6}\beta_3 \frac{\partial^3 A}{\partial T^3} \\ &= i\gamma \left(|A|^2 A + \frac{i}{\omega_0}\frac{\partial}{\partial T}(|A|^2 A) - T_R A \frac{\partial |A|^2}{\partial T} \right) \end{aligned} \tag{4.1}$$

taking into account the effects of chromatic dispersion of the second (β_2) and third (β_3) orders, the nonlinearity (γ), the medium attenuation (α), self-steepening and the Raman effect ($T_R = 3$ fs). Also in Eq. (4.1), A is the electric field, T the time, ω_0 the carrier frequency, and $i = \sqrt{-1}$.

Equation (4.1) is solved numerically using the fourth order RK4IP with an adaptive step size [167, 180], on an Nvidia GeForce GTX 550Ti using Reikna [174] on top of PyOpenCL [175], with 2^{15} sample points in time and frequency, for a large temporal window and a good temporal

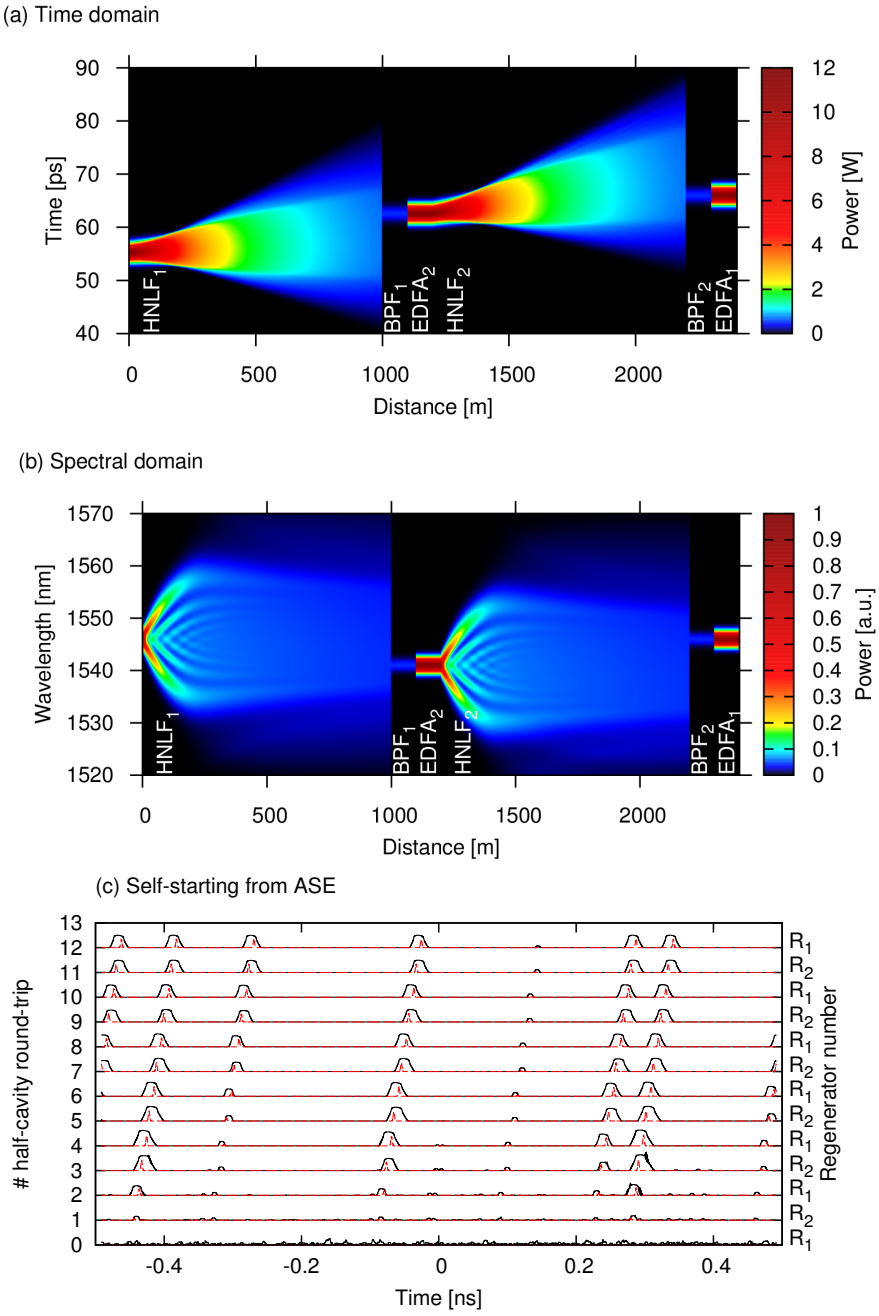

Figure 4.2 – *(a) and (b): Maps of the pulse propagation, in the time and frequency domains, in steady-state. The length of the amplifying and filtering regions is increased for readability. (c) Self-starting from noise, after the HNLF (solid line) and after filtering (dashed line).*

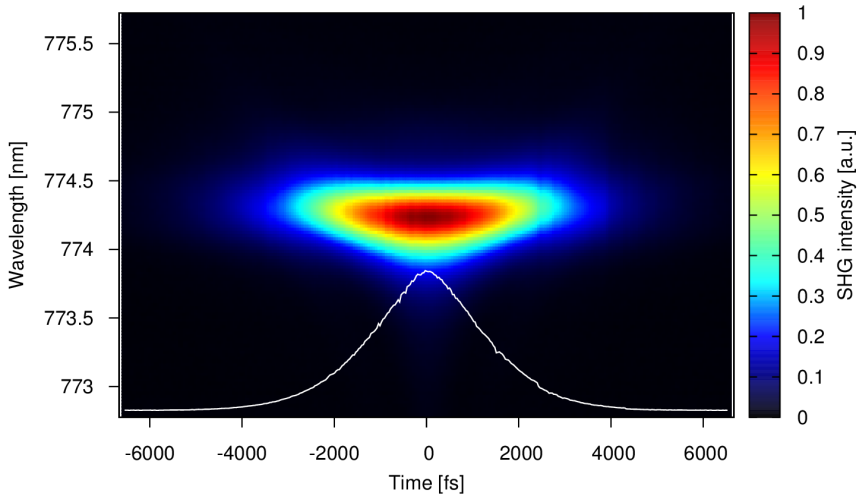

Figure 4.3 – *Spectrogram of pulses generated after the BPF, with an autocorrelation width of 4.4 ps.*

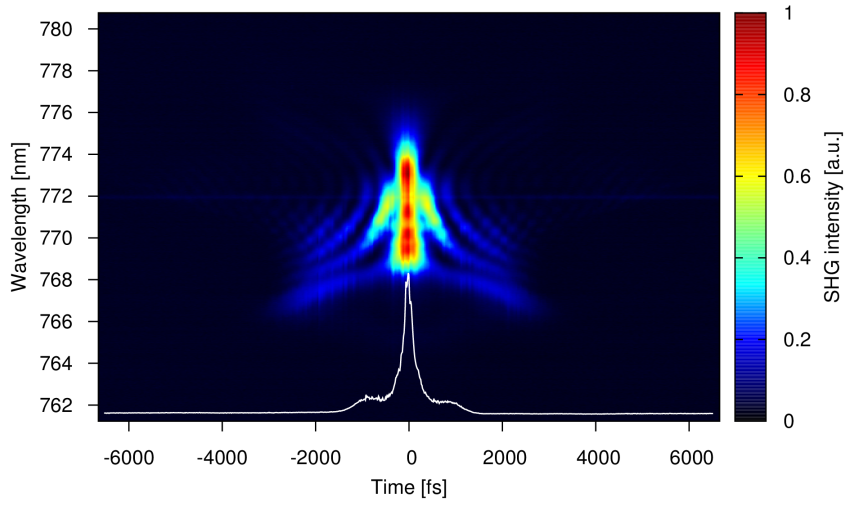

Figure 4.4 – *Chirped pulse amplification with the addition of SMF-28 fiber after the nonlinear medium. The compressed pulse has an autocorrelation width of 478 fs.*

and spectral resolution. Amplifiers are characterized by a saturable output power P_{out} modeled as the following [187]:

$$P_{out} = P_{in} G_0 \exp\left[-\frac{P_{out} - P_{in}}{P_{sat}}\right] \tag{4.2}$$

where P_{out} is related to the input power P_{in} with the small signal gain G_0 and the saturation power P_{sat}. When explicitly specified, the amplifier noise is included in the calculations [47]. A single polarization component is considered to interfere with the oscillating signal, the other component being orthogonal. The total ASE power

$$P_{\text{ASE}} = \int_{-\infty}^{\infty} n_{\text{sp}} h \nu_0 (G-1) H_{\text{A}}(\nu - \nu_0) \mathrm{d}\nu \tag{4.3}$$

where $n_{\text{sp}} = 2$ is the spontaneous-emission factor, h the Planck constant, G is the gain, ν_0 is the central frequency, and H_{A} is the gain profile approximated by a tapered cosine window in the range 1525 nm to 1560 nm [188]. Band-pass filters are modeled with a Gaussian profile, and a real response is assumed. Loss is neglected in all components, except for the HNLFs.

The source self-starts from spontaneous emission. A minimum of 20 cavity round-trips are performed for each simulation to assess whether self-starting occurs or not. When self-starting occurs, a steady-state is usually reached within the first 15 cavity round-trips. The setup of Fig. 4.1 is observed at outputs O_{1-4}, and a time-domain filter, numerically implemented, is added at outputs O_2 and O_1, providing two additional outputs. These filters are super-Gaussians of order 10, and are centered over the most powerful pulse with a temporal duration of 3$\times$ the pulse FWHM. The Fourier transformed signal therefore shows a profile cleared of the beats induced by the presence of multiple pulses, and spectral features can be measured more accurately.

4.3 Results

In Section 4.3.1, the operation of the self-pulsating source of Fig. 4.1 is observed under a set of different configurations. We assess its ability to self-start from ASE under several values of gain, spectral offset Δ, and filter bandwidth Ω. In subsection 4.3.2, one BPF is spectrally shifted once the source has reached a self-pulsating state. In this process, the output pulse properties are investigated and the source stability is analyzed in terms of time and amplitude jitter in Section 4.3.3.

4.3.1 Self-starting conditions: contribution of the filter offset

The experimental values of Sun et al. [16] are being used for the following simulations: at $\lambda_0 = 1550\,\text{nm}$, $D = -0.69\,\text{ps}\,\text{nm}^{-1}\,\text{km}^{-1}$, $S = 0.0074\,\text{ps}\,\text{nm}^{-2}\,\text{km}^{-1}$, $\alpha = 1.86\,\text{dB}$. The saturation power, however, is reduced to 6 dBm to limit the number of pulses in the cavity, to avoid overlaps and therefore facilitate the extraction of pulses from the temporal signal.

There are three regimes of operation for a self-pulsating source, depending on the filter spacing Δ, as pointed out in [16]. Increasing the value from $\Delta = 0$, the emission transforms from a CW regime, to a SP regime, to a PB regime. In the latter, only existing pulses are sustained, and the source cannot ignite pulses from ASE noise for example when the doped fibers are pumped with increasing power. To assist the realization of such sources, it is necessary to describe the conditions for self-starting, their relationship to the filter offset, the filter spectral bandwidth and the available amplifier gain. Numerical simulations show that the transition between the CW and the SP regimes with increasing Δ occurs gradually. Gaussian pulses build up in the cavity in the first 20 cavity round-trips, but also coexist with CW components, forming a noisy pulsed signal in time, with a noise amplitude that decreases with increasing Δ. Experimentally, the wavelength dependent attenuation introduced by the cavity components leads to a co-propagating amplified ASE signal. Figure 4.5(a) shows the coexistence of these signals in the time domain, with an amplitude jitter of $\sim 4\%$ in power, and Fig. 4.5(b) depicts the corresponding spectrum.

An appropriate time-domain filtering confirms that the pulses profiles in time are associated with the sidelobes of the spectrum, under the influence of SPM, while the noisy signal in time stands spectrally at the intersection of the BPFs.

In a first series of simulations, the operating regimes which allow self-starting are shown as a function of the amplifier gain and the filter spectral offset, from an initial invariant ASE spectrum. In Fig. 4.6, the normalized filter offset $F = \Delta/\Omega$ is considered, and the source is in a pure pulsing regime with a clear background when $F \gtrsim 1.7$. Figure 4.6 shows the number of oscillating pulses, as well as the ratio of noise over signal power, for several filter bandwidths. Self-starting at large Δ is also enabled by an increased gain, but the number of propagating pulses saturates due to the fixed $P_{sat} = 6$ dBm. It may be noted that for a bandwidth $\Omega = 0.9\,\text{nm}$ and $G_0 =\sim 100$, the operation region spreads from 1.6 nm to 2.2 nm, which corresponds well with the behavior observed experimentally, in Fig. 4 of [16] reproduced in 4.5(c). The leftmost gradient of Fig. 4.6(aa) – (ff) indicates the decrease of noise as Δ increases, and the yellow rightmost region indicates

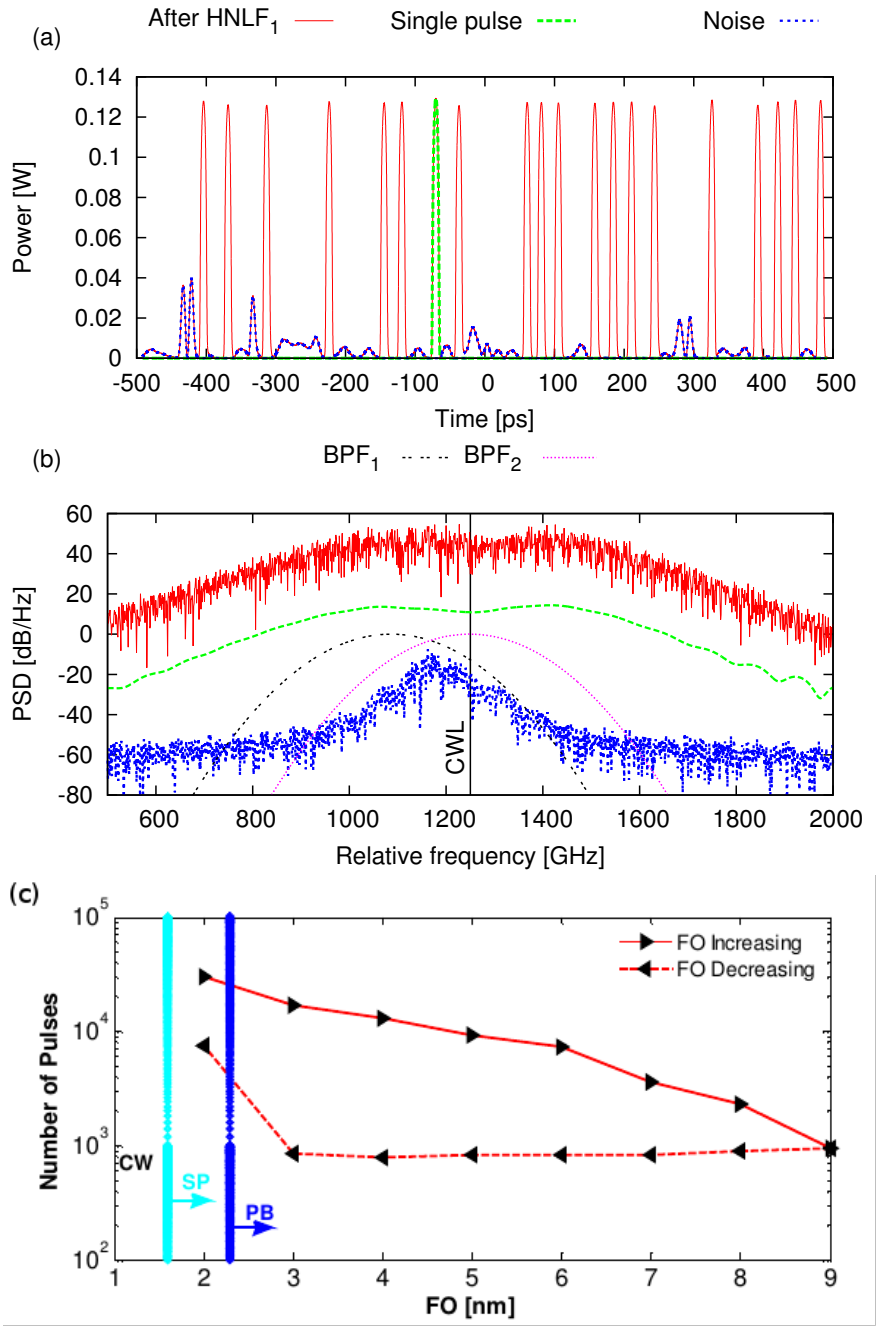

Figure 4.5 – *In (a), noisy signal including a series of eigenpulses (red), and isolated eigenpulse (green) and a noise floor (blue) in the time domain. In (b), spectra of the noisy signal (red), isolated eigenpulse (green), and noise floor (blue). The transmission profiles of BPF_1 and BPF_2, separated by 162 GHz, are also provided. (c) Fig. 4 of Sun et al. From [16], reproduced with permission.*

the absence of pulses in the cavity. In [16], self-pulsing operation is demonstrated with filters of bandwidth of 0.4 nm and 0.9 nm, but this bandwidth can be increased safely at least up to 4.0 nm and more without preventing self-pulsation. For this particular nonlinear medium, a wide range of filter bandwidths leads to self-pulsation. The two conditions for generation of eigenpulses are 1) an adequate spectral separation Δ between the band-pass filter that does at the same time favor pulses over CW oscillation and tolerate an initial ASE propagation, 2) an amplifier gain which is sufficient to trigger SPM broadening from the ASE. Qualitatively, in the case of pulses that are temporally long, for a small filter bandwidth Ω, requirement 2) may be difficult to attain. At large filter bandwidths, the spectral content is more likely to produce a fast varying intensity profile, whose slope induces important amounts of spectral broadening by SPM. In this case, the amplifier gain must be sufficient to sustain pulses of that power spectral density in spite of other cavity losses.

4.3.2 Transition in between the self-pulsating and pulse-buffering regimes

Practically, tuning one BPF towards the PB regime is interesting. High values of the normalized filter offset improve the signal over noise ratio, and diminishes the number of pulses in the cavity. Their peak power is therefore increased, and ultrashort pulses can be generated by nonlinear compression at C_1. In this series of simulations, the source is started from ASE noise with a spectral offset of $\Delta = 1.7$ nm, in SP regime, and spawns 14 pulses in the simulation's temporal window. The band-pass filter has a spectral FWHM of 0.9 nm, and the unsaturated gain $G_0 = 200$, with $P_{\text{sat}} = 9$ dBm.

In order to attain the PB regime, BPF_1 must be spectrally shifted towards longer wavelengths, which can be done experimentally with tunable filters. To ensure a smooth transition, by leaving the circulating pulses unaffected, the filter is shifted by 5 pm at each consecutive cavity round-trip. Because the time window of 1 ns used in simulations is much shorter than the round-trip period of the source of $\sim 10\,\mu$s, the number of pulses that circulate in the cavity is limited by the sampling window. Sharp transitions occur when the number of pulses changes, as the available power is redistributed among the remaining ones. Experimentally, however, one can expect to observe a smoother behavior, since $\sim 10^4\times$ more pulses can coexist in the cavity, when the cavity size is ~ 2 km. In Fig. 4.7, the source is started from ASE and 14 pulses circulate in the simulation's temporal window. After 15 cavity round-trips, filter BPF_1 is shifted at a rate of 5 pm/round-trip.

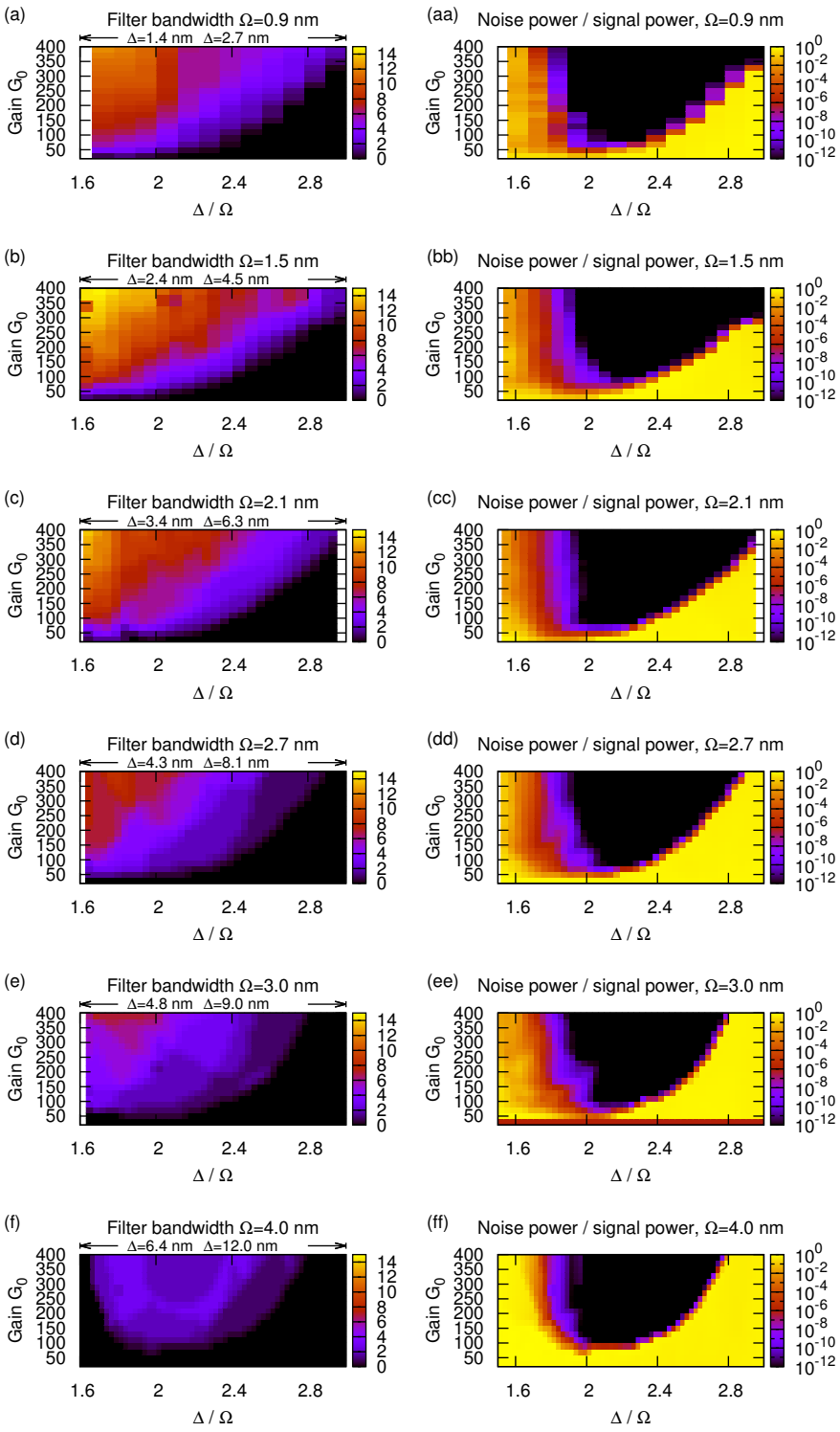

Figure 4.6 – *Left: Number of pulses as a function of the gain and the filter offset Δ, for filter bandwidths of 0.9 nm to 4.0 nm. Right: corresponding plot of noise/signal power.*

Figure 4.7(a) depicts the efficiency of the source, the number of pulses in the cavity, the EDFA gain, and the peak power of circulating pulses as a function of the spectral separation of the BPFs. A maximum of $\sim 13.5\%$ of transmission is reached at a filter offset of 2.6 nm. This corresponds to the position of the first SPM lobe for a nonlinear phase-shift of $\sim 2\pi$ [38]. The discrepancy in gain and pulse peak power, particularly visible at high Δ, indicates that the source tends to lose its unique eigenpulse in favor of two different pulses, one per HNLF. Although pulses are of similar FWHM, the third order dispersion of the HNLFs induces an asymmetry on their spectrum [189]. With fibers featuring a positive dispersion slope, the blue-most filter BPF_2 enables a higher transmission than BPF_1, which yields to pulses that are up to 12% more powerful compared to the ones out of BPF_1.

In Fig. 4.7(b), the output chirp slope and pulse FWHM, the pulse temporal FWHM, and the bandwidth at BPF_1 are depicted as a function of the filter offset. Because the chirp is close to linear, the chirp slope refers to the value of the chirp derivative at the position of maximal peak power. In this particular configuration and in setups including a narrow BPF such as this one, the chirp remains low for all Δ, and the pulse has a time-bandwidth product of 0.45. Aside from the discrepancy in peak power, the outputs O_2 and O_4 are interchangeable. In Fig. 4.7(c), the time and amplitude jitter are depicted as a function of the filter offset. The amplitude jitter is defined as $\delta P/P_0$, where δP is the standard deviation of the peak power of all pulses visible in the temporal window, and P_0 the median peak power. The time jitter measures the pulse-to-pulse time difference between the current and the previous cavity round-trip. The amplitude jitter increases significantly when a pulse is about to be discarded. Temporally, it is observed that most pulses are unequally affected in this process, and undergo a reduction of their peak power. The nonlinear power transfer function of cascaded regenerators quickly discards pulses of low peak power, and a new stable state occurs. At all time, the timing jitter is stable and negligible in the cavity, which is expected for a cascade of 2R regenerators. In Fig. 4.8(a) , from the configuration depicted in Fig. 4.7, the spectral offset Δ is decreased once a stable single pulse operation is attained. The amplifiers are modeled with spontaneous emission from Eq. (4.3). The single pulse propagating in the cavity is sustained, and the source can not spawn new pulses from ASE when there is no filter overlap, since the 2R regenerator intrinsically rejects ASE noise. It is only when Δ approaches 1.96 nm that new pulses are generated, marking the transition between the PB regime and the SP regimes. In this process, simulations indicate that the amplifier noise is the predominant factor

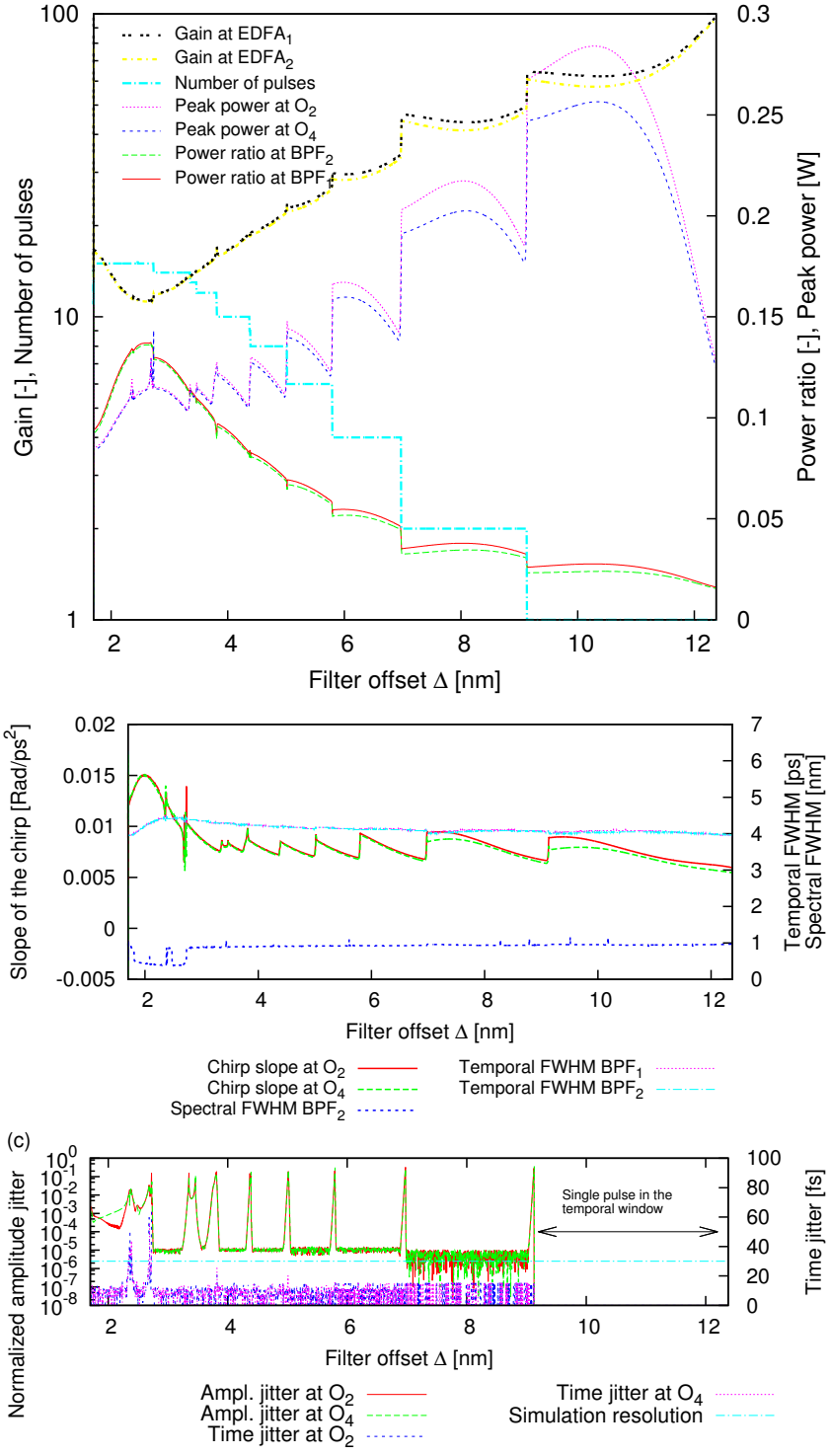

Figure 4.7 – *Transmission at $BPF_{1,2}$, number of pulses and peak power observed in the simulation for $G_0 = 200$. The asymmetry of the SPM-induced spectral broadening due to third-order dispersion is responsible for the transmission mismatch between BPF_1 and BPF_2. (b) Chirp slope and pulse temporal width as a function of the filter distance Δ. (c) Amplitude and time jitter after the BPFs.*

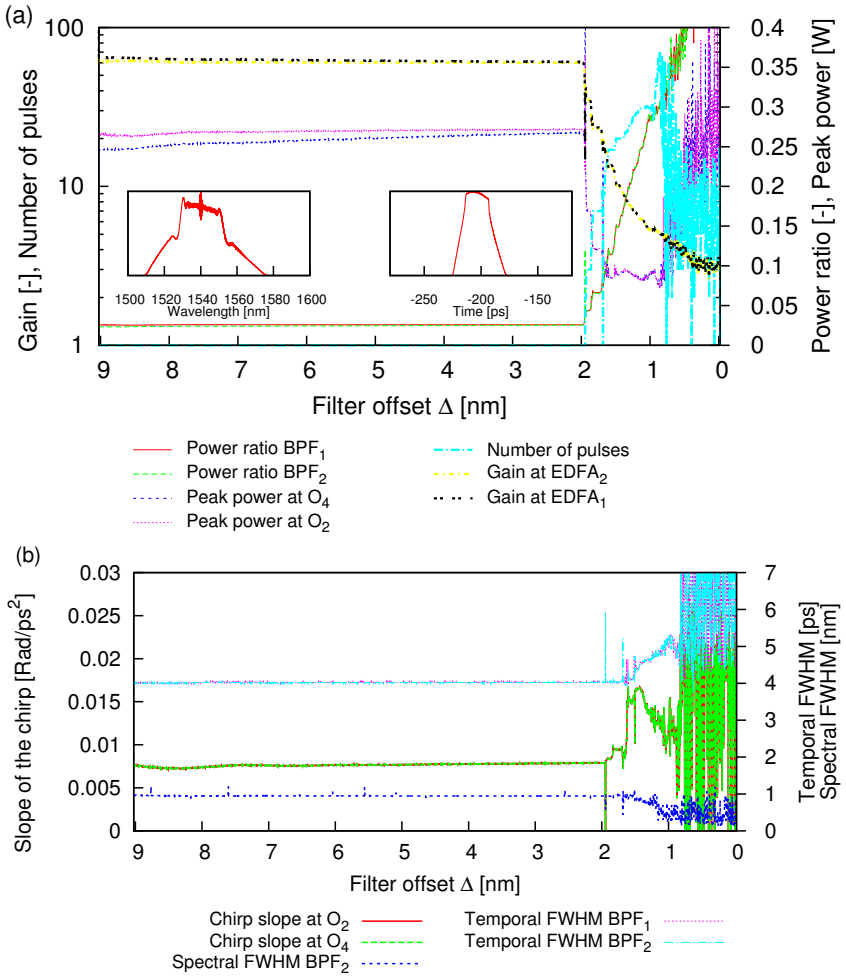

Figure 4.8 – *(a) Transmission at $BPF_{1,2}$, gain, number of pulses and peak power observed in the simulation for $G_0 = 200$ and a bandwidth of 0.9 nm, as the offset Δ is decreased. Insets: typical spectral and temporal shape over the range 9 nm to 2 nm. (b) Corresponding chirp slopes and temporal pulse widths.*

for the generation of new pulses in the cavity, rather than pulse-splitting, which occurs because of the spectral overlap of the BPFs. The wavelength of transition between the SP and PB regimes is hence different whether Δ is increased or decreased.

4.3.3 Stability: timing and amplitude jitter

As indicated by Fig. 4.8(a) and (b), the source shows an excellent stability over a wide wavelength range. Once in PB regime, little chirp or peak power variation occur as Δ is altered. This stability originates from the amount of chromatic dispersion accumulated in the HNLFs, which prevents large spectral fluctuation induced by SPM alone. This amplitude jitter is associated with the presence of multiple eigenpulses in the cavity, as reported in [149]. When pulses of different peak power co-propagate, their group-velocity, associated with the effective refractive index, and therefore related to their peak power, induces timing jitter and pulse collision. In comparison, Fig. 4.9(a) features a HNLF with a dispersion $D = -0.173\,\mathrm{ps\,nm^{-1}\,km^{-1}}$. Numerous instability domains result from the insufficient amount of chromatic dispersion in the nonlinear medium, for filter offset Δ larger than 5.5 nm. By observing the inset of Fig. 4.9(a), it is apparent that $\mathrm{BPF_1}$ intercepts the SPM-induced spectrum at a position where the slope of the spectrum is large. In this case, for a fixed filter position, small amplitude variation at the input are translated into large peak power variations at the output and the source experiences an amplitude and a timing jitter. This unstable state is not necessarily permanent, since a pulse is occasionally discarded by pulse collision, and hence resets the source to a stable operation. Figure 4.9(b), depicts the coexistence of different eigenpulses in the source, in accordance with [149]. After self-starting, the temporal simulation window contains 23 pulses. Collisions occur in that process, and the number of pulses drops to 21 after 5000 cavity round trips. Since these eigenpulses have different group velocities, collisions occur and ultimately only a single type of eigenpulse is sustained at the steady-state. In regenerative sources, reaching optical wave-breaking is desirable, because this phenomenon flattens the central part of the spectrum, as illustrated in the inset of Fig. 4.8(a). A large ratio of the dispersive and nonlinear lengths $L_D = T_0^2/|\beta_2|$ over $L_{\mathrm{NL}} = 1/(\gamma P_0)$, ensures that wave-breaking is reached. In addition to that, the input pulse sent to the HNLFs is always chirped, which accentuates this effect. The loss in the HNLFs is also beneficial in terms of stability, because it decreases the importance of nonlinearities while leaving the accumulated dispersion unaffected.

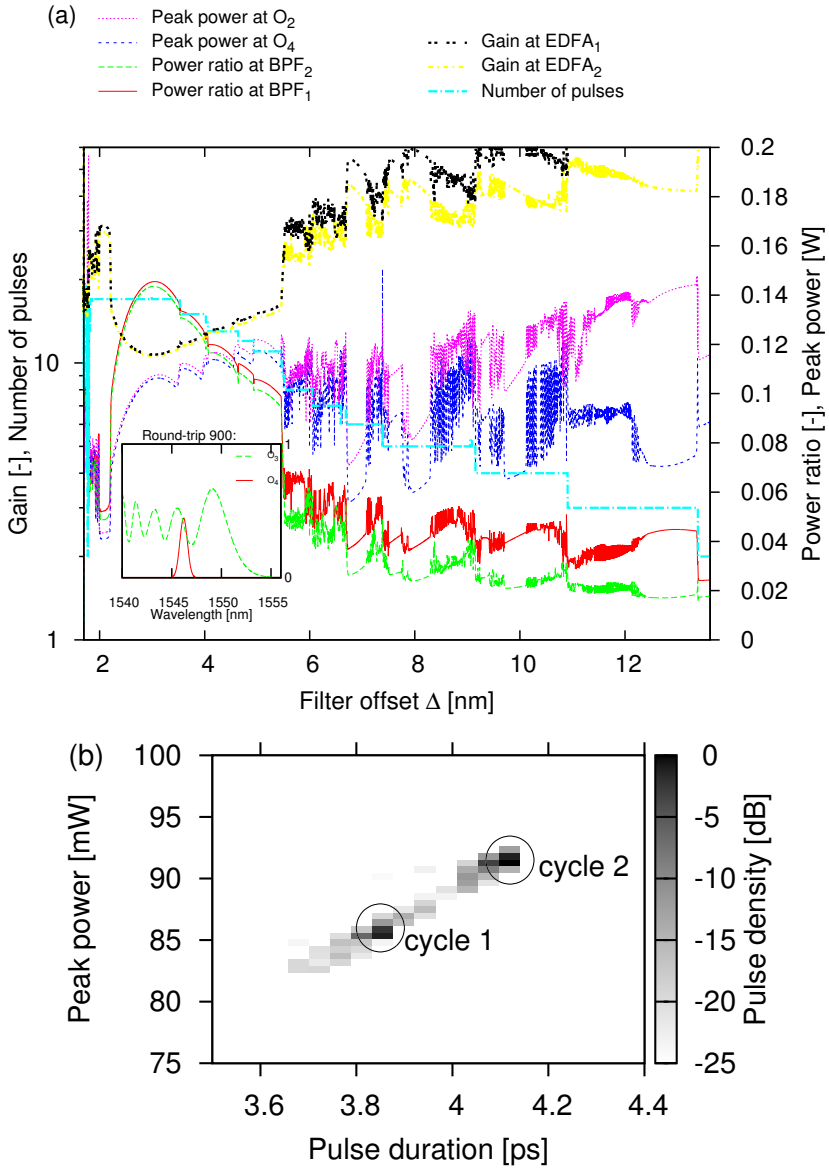

Figure 4.9 – *(a) Peak power, power ratio, gain and number of pulses in the cavity for* $G_0 = 200$, $D = -0.173\,ps\,nm^{-1}\,km^{-1}$. *Inset: For round-trip #900, spectrum at* O_1 *and* O_2. *(b) Limit cycles for* $D = 0.395\,ps\,nm^{-1}\,km^{-1}$ *and* $G_0 = 200$.

4.3.4 Pulse properties in the PB regime

Previous work of Sun et al. [16] reveals that the chirp of output pulses after filtering increases with the filter bandwidth. The reason behind this observation is that pulses that undergo SPM in a medium of normal dispersion acquire a chirp which is close to linear, and corresponds in the spectral domain to a linear delay function across the broadened spectrum. A broader filter therefore captures spectral components that have a larger relative delay, leading to an increased chirp. In the configuration (f) of Fig. 4.6 with a gain $G_0 = 100$, it is assessed that the pulses could be recompressed down to 930 fs by the addition of single-mode fiber (SMF) at the output O_2, in good agreement with [16]. This value is close (within 5%) to the value of 880 fs expected for transform-limited pulses, confirming that the chirp is close to being linear. With a BPF bandwidth of 6 nm, the chirp becomes nonlinear due the growing influence of the asymmetries in the SPM-broadened spectrum. Along with the effects of third order dispersion, nonlinear recompression at C_1 therefore saturates at 210 fs for Ω =4 nm and 6 nm despite the large available bandwidth exceeding 20 nm. Nevertheless, the source shows an excellent stability at large BPF bandwidths, as well as a good efficiency above 20% caused by a large amount of power captured at the filtering stage.

It must also be pointed out that the FWHM of the filtered spectrum depends directly on the shape of the broadened signal. After a filter that faces a dip in the SPM-broadened spectrum, the output pulses can be up to 20% shorter in time than those for which the filter faces a local maximum. Figure 4.10(a) illustrates this in the spectral domain, while Fig. 4.10(b) shows the corresponding time-domain pulses, centered at the origin for simplicity. After a linear shift of BPF_1 towards longer wavelengths in the PB regime, the distribution of temporal FWHM of the pulses emanating from this displacement is presented in Fig. 4.11, when $P_{\text{sat}} = 9$ dBm. The pulse width reported in this figure is the median value of the FWHM of pulses visible in the time window, their variance being negligible. Figure 4.11(c) and (d) present a larger dispersion of pulse widths due to the instabilities encountered while altering the value of Δ. From that spectral position, if BPF_1 is shifted towards shorter wavelengths, the number of pulses in the cavity remains fixed, at its minimum value. If wavebreaking is reached due to an increased pulse peak power, the spectrum flattens as observed in the inset of Fig. 4.8, and the distribution of temporal pulse duration will show no dispersion.

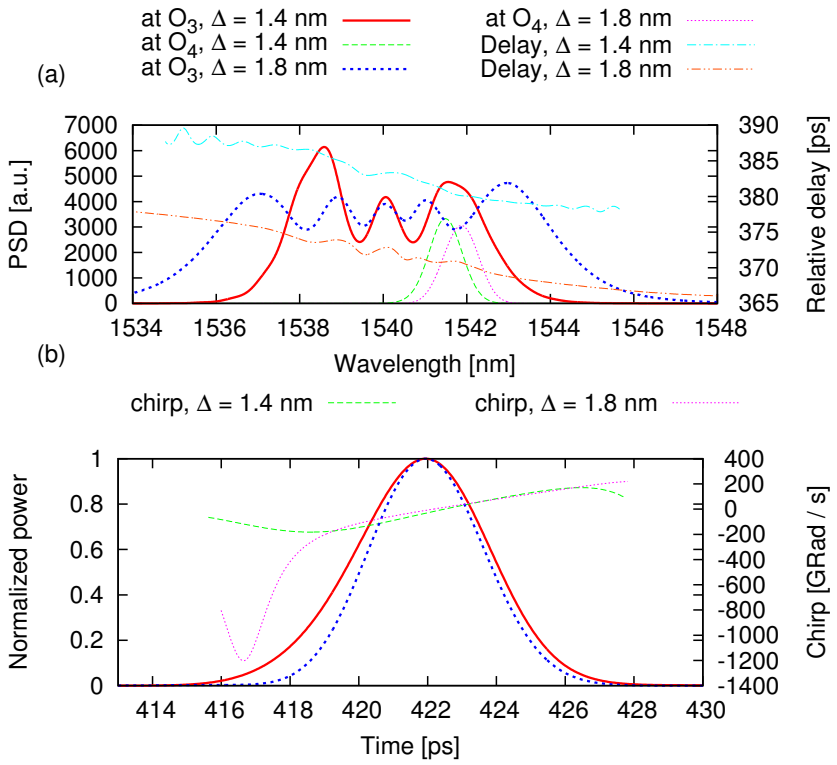

Figure 4.10 – *Spectral and temporal profiles associated to* $\Delta = 1.4$ *and 1.8 nm for* $G_0 = 100$. *Different positionnings of the band-pass filters with respect to the SPM-induced spectrum result into different pulse duration and spectral width.*

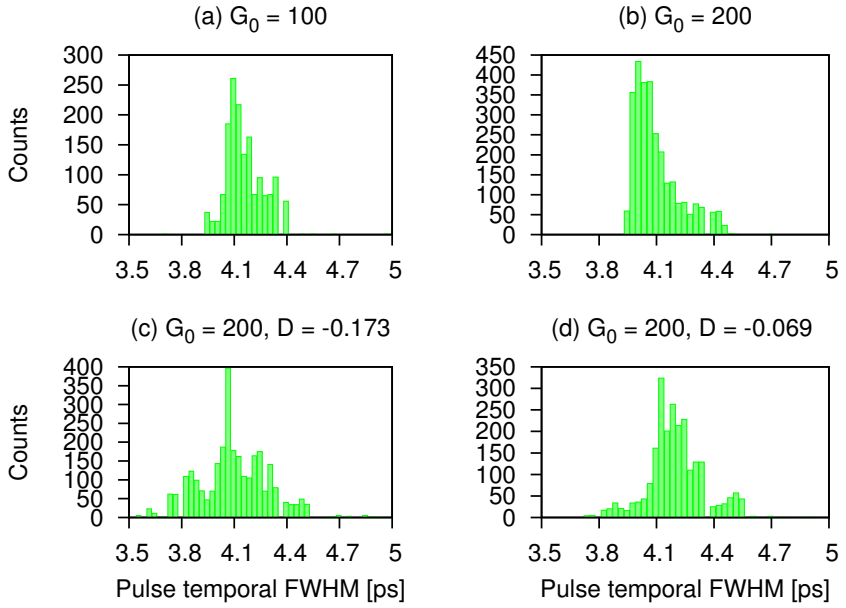

Figure 4.11 – *Temporal FWHM distribution of pulse in PB operation for (a)* $G_0 = 100$*, (b)* $G_0 = 200$*, (c)* $G_0 = 200$ *and a chromatic dispersion* $D = -0.173\,ps\,nm^{-1}\,km^{-1}$*, (d)* $G_0 = 200$ *and* $D = -0.069\,ps\,nm^{-1}\,km^{-1}$*.*

4.3.5 Summary

A numerical study of self-pulsating sources based on cascaded regeneration was performed for a set of cavity configurations. Self-starting is observed for a broad range of filter bandwidths, gain values, and filter offsets. The ability of these sources to self-start depends on the gain of the amplifiers being used, while the number of pulses is determined by the saturation power of the amplifiers. Self-starting occurs with an unsaturated gain that decreases with increasing filter spectral width. As well, the source enters the self-pulsating regime with filter bandwidths in the range 0.1 nm to 4.0 nm, making this architecture very interesting in practice. The continuously changing temporal profile eigenpulses propagating in the cavity is reminiscent of other types of self-pulsating sources such as self-similar or stretched-pulse lasers. In these lasers, linearly chirped pulses are propagating in the cavity, enabling high energies without impairments due to the excess of nonlinearities inside the cavity. The regenerative sources architecture offers such advantages as well, and limitations induced by excessive nonlinearities occur only in the PB regime, when the cavity contains very few pulses. By design, regenerative sources however reject a relatively large fraction of their spectrum at the filtering stages, and this is the main obstacle to the generation of high energy pulses.

The third-order dispersion of the HNLFs introduces asymmetries in the spectral features of output pulses, as shown in [189], which translate into output pulses of different energies after each regeneration stage. The gain of the EDFAs can be adjusted relatively to the sign of β_3 in order to compensate for this discrepancy.

Pulse properties have also been investigated, and variations in the pulse duration occur in PB regime as the spectral filter offset is altered. The pulse bandwidth is influenced by the shape of the SPM-broadened spectrum after the HNLFs. Especially for large filters, it turns out that the pulse duration can vary by $\sim 20\%$ mainly for this fact.

It could be tempting to increase the filter bandwidth in order to generate ultrashort pulses. However, an additional chirp limits the expected pulse shortening. The addition of a standard SMF leads to near transform-limited pulses after the BPFs, and simulations show that subpicosecond pulses can be obtained without nonlinear compression at output $O_{2,4}$. However, nonlinear recompression is bound to the effects of third-order dispersion and to the limited spectral broadening that pulses undergo in the nonlinear medium. Finally, amplitude and timing jitters are observed in fibers that have large ratios of dispersive length over nonlinear lengths. This must be kept in

mind for the conception of such sources that offer a high nonlinearity and for which the nonlinear length is much smaller than the dispersion length. Such sources are more likely to be unstable if operated with band-pass filters of relatively narrow spectral widths.

4.4 Design of a regenerative source of large bandwidth

Self-pulsating sources based on cascaded regeneration by self-phase modulation and offset filtering are investigated experimentally using large filter bandwidths of 3.5 nm and higher. In this configurations, less energy is wasted during the regeneration stage because the BPFs capture a larger amount of spectral components contributing to the pulses. In accordance with the numerical results of Section 4.3, such sources self-start from ASE, and picosecond pulses are sustained in a nonlinear cavity. We provide numerical and experimental results indicating the generation of 2 ps pulses, and observe 0.4 ps pulses after dispersion compensation and amplification. We also demonstrate that a pair of low- and high-pass filters also spawn pulses whose bandwidths are determined by the combination of the filters and gain profile, hence simplifying the experimental setup for short pulse generation.

4.4.1 Experimental setup

The self-pulsating cavity under study is depicted in Fig. 4.12(a), and resembles the design of [17]. Instead of using BPFs tunable in wavelength only, filters that are adjustable in bandwidth and tunable in wavelength are used. As shown in Fig. 4.12(b), such filters offer flexibility, but with the downside that their spectral shapes deviate strongly from Gaussian, and are best fitted with super-Gaussians. As a consequence of that and by the properties of the Fourier transform, the temporal profile of the output pulses is expected to exhibit a pedestal. The HNLF has a waveguide nonlinear coefficient $\gamma = 11.5\,\mathrm{W^{-1}\,km^{-1}}$, second- and third-order chromatic dispersion coefficients $D =$ -0.71 ps/(nm·km) and $S = 0.0074$ ps/(nm^2·km) at a wavelength of 1550 nm for a length of $L =$1007 m. BPF$_1$ is continuously tunable in bandwidth and wavelength in the C-band, and has an insertion loss of 5.5 dB. BPF$_2$ is adjustable by passing or blocking neighboring channels of 100 GHz. It has an insertion loss of 8 dB. Each circulator has an insertion loss of 2 dB, and each output coupler O_i has an insertion loss of 0.5 dB in addition to the loss resulting of their coupling ratio. The EDFAs have a saturated output power of ~ 15dBm. Pulses centered at a wavelength of

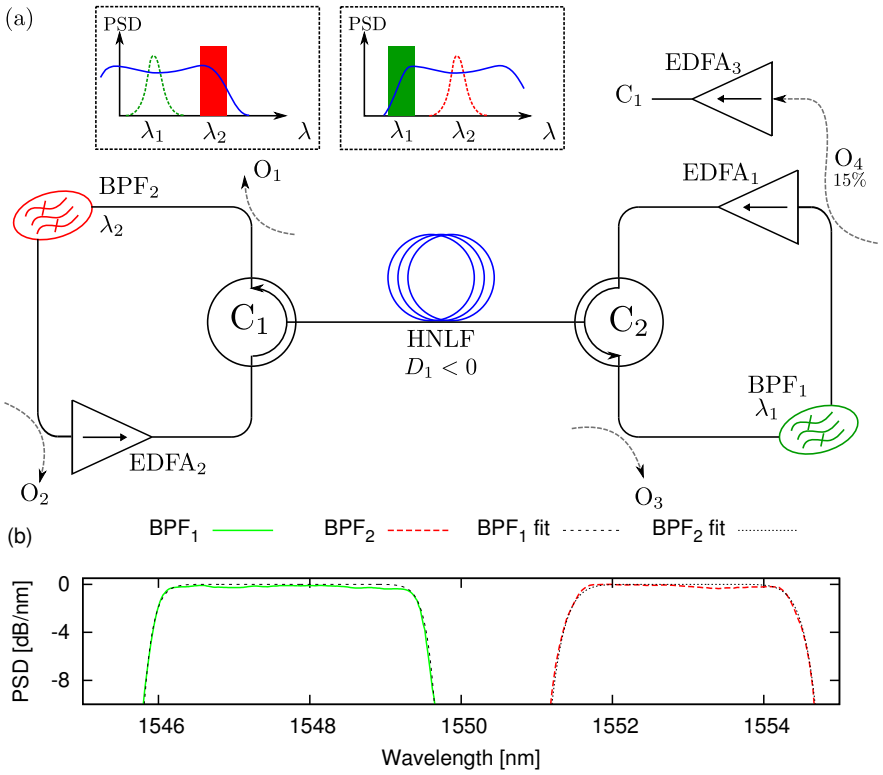

Figure 4.12 – *(a) Experimental setup of the self-pulsating source. Insets: Spectral overview of the source operation, including spectral broadening by SPM and offset filtering at wavelengths λ_1 and λ_2. (b) Profiles of the BPFs.*

λ_1 undergo spectral broadening in the HNLF by SPM in a medium featuring normal dispersion. A slice of that spectrum is preserved at BPF_2. Amplification compensates for the loss in power, and the pulses now centered at λ_2 propagate in the HNLF in the opposite direction. Their spectrum is broadened by SPM, and part of that spectrum traverses BPF_1, and is amplified at $EDFA_1$, therefore closing the loop. BPF_1 is first shifted towards the long wavelengths to trigger self-pulsation, and then in the opposite direction to attain the PB regime. The source self-starts for any BPF bandwidth smaller than 14.5 nm, which is the upper limit of tunability of BPF_2.

In a first configuration, the bandwidth of BPF_1 is set to 3.5 nm, and the 3 dB edge-to-edge spectral separation between the filters is of 1.8 nm. The bandwidth of BPF_2 is of 3.2 nm. Output pulses are observed in the time domain via a FROG. These measurements are compared with simulations in Fig. 4.13. The numerical model includes super-Gaussian filters as described in Fig. 4.12(b), and the HNLF is modeled including its second- and third-order dispersion coefficients. Nonlinear propagation is modeled with a Runge-Kutta algorithm of order 4 on a GeForce GTX 470 processor, with an adaptive step size [167, 180]. The simulation begins from the ASE spectrum sampled from an EDFA in an open loop configuration. Figure 4.13 indicates that the pulses generated at a filter bandwidth of 3.5 nm exhibit a near-Gaussian shape with a pedestal.

The recovered pulses have a duration of 2 ps, and simulations indicate that dispersion compensation does not enable a significant compression, in contrast with the Gaussian BPFs of Ref. [16]. In case of Gaussian BPFs, the duration of pulses would be of 2.6 ps, and 1 ps when the chromatic dispersion is compensated with additional SMF. The measured pulse duration corresponds well to the simulation, as depicted in Fig. 4.13(a) and (b). The differences in the chirp values are attributed to the effects of amplification at $EDFA_3$, as well as the residual error in the FROG retrieval algorithm, confirmed by the mismatch between the retrieved pulse duration and the autocorrelation width. Fig 4.13(c) and (d) indicate the autocorrelation width and retrieved pulse profile when the output signal is amplified, and 13 m of additional SMF-28 fiber are appended at O_4. The pulse duration shortens because nonlinear compression occurs as a consequence of SPM inside $EDFA_3$ followed by the effects of chromatic dispersion of SMF. This measurement differs from the nonlinear compression of Fig. 9 in Ref. [16], in which pulses were compressed at O_3, as depicted in Fig. 4.14. In Fig. 4.15, the output spectra of the source observed at O_1 are shown for three different filter offsets, and compared with the pulsed operation of Ref. [16]. The amount of spectral broadening induced by SPM in Fig. 4.15 in the setup of Sun et al. is such that $< 2\%$ of the power is transferred from λ_2

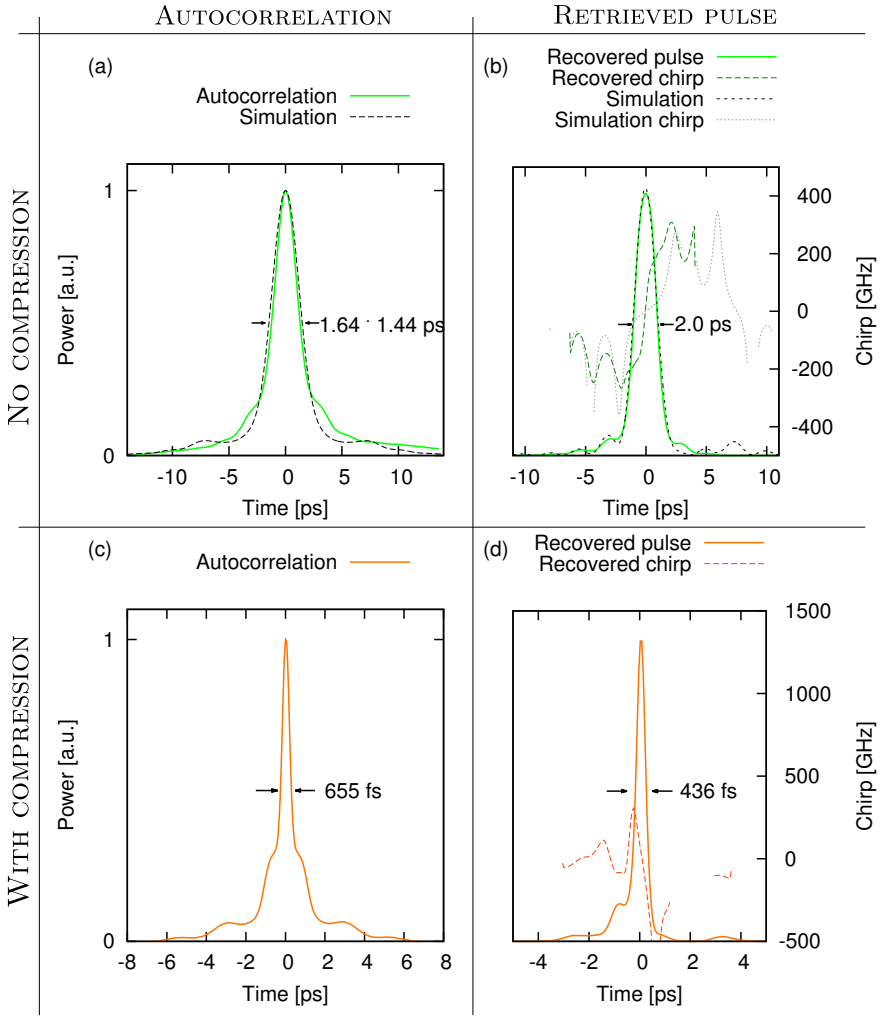

Figure 4.13 – *Pulses observed at O_4 (first row) and C_1 (second row) (a) Measured and simulated pulse autocorrelation, (b) FROG recovered pulse and simulated pulse, (c) autocorrelation of the pulse compressed with additional SMF, (d) pulses of (c) as retrieved by the FROG.*

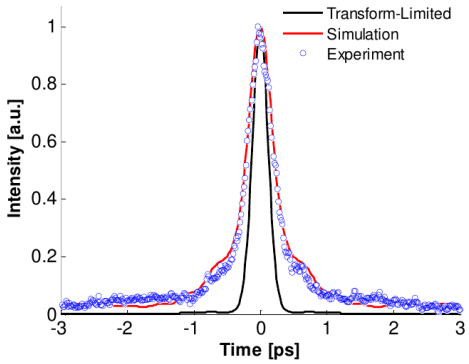

Figure 4.14 – *Nonlinear pulse compression.From [16], reproduced with permission.*

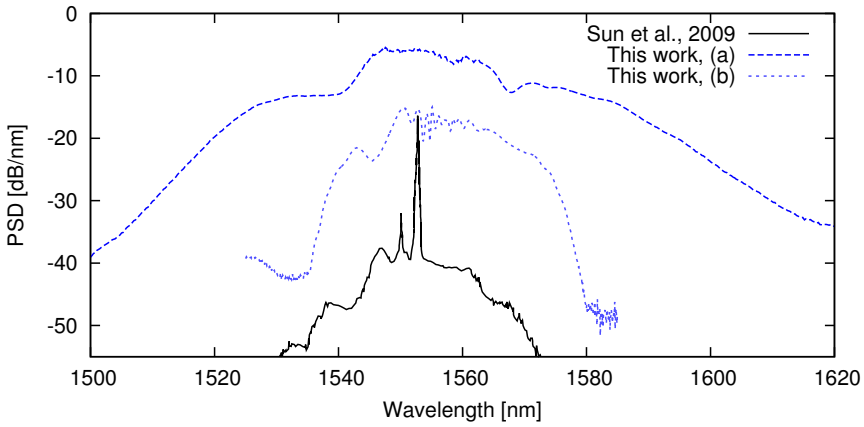

Figure 4.15 – *Comparison of the output spectra originating from this work and previous work by Sun et al. In [16] (solid line), the filter bandwidth was of 0.9 nm, and the filter offset was of 2.6 nm. In this work, the filter bandwidth is of 3.5 nm. In (a), with a filter offset of 4.2 nm, and in (b) with a filter offset of 5 nm. The reference level of each line was adjusted for visibility.*

to λ_1. In (a) and (b), the amount of transferred power is of 13% and 15%, respectively. The large 3 dB spectral broadening of 18 nm in (a) and 13 nm in (b) suggests the propagation of powerful and short pulses. The light propagating in the cavity is composed of ASE and pulses, and the pulse energy is measured when a small number of eigenpulses are visible in the time domain. Since the cavity round-trip time is of 10.6µs, the energy contained in the pulses account only for a small portion of the total energy. Under the assumption that the peak power of the pulses does not change significantly when the number of pulses in the cavity changes, the energy is estimated by measuring the average output power as a function of the number of pulses. The decrease in average power is monitored as well as the number of pulses measured by an oscilloscope through one cavity period. In the current context where the pulse power is small with respect to the total ASE power, the ASE power is expected to remain constant independently of the number of pulses. The energy contained in each pulse can be inferred from the measured average power.

In Fig. 4.16, the filter offset is increased to reduce the pulse number. At output O_4, the energy per pulse is estimated to be of 3.5 pJ, considering a pulse duration of 2 ps, and therefore the pulse peak power is of 1.7 W at O_4. With a 3 dB spectral separation of 4.5 nm, the cavity contains 12

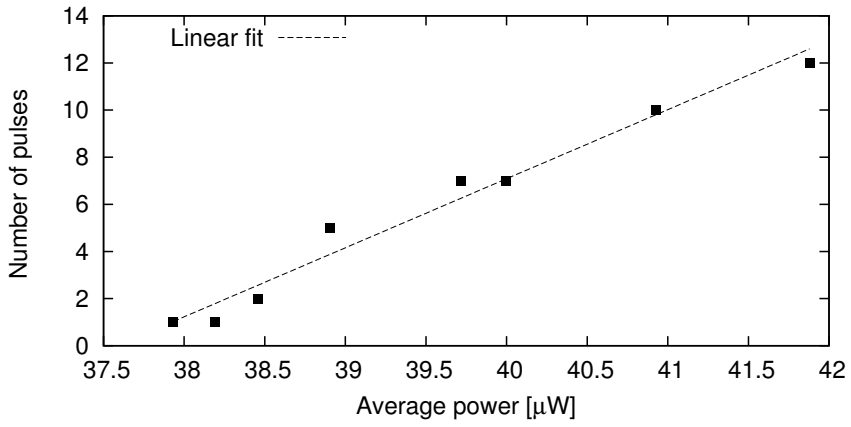

Figure 4.16 – *Number of pulses as a function of the cavity average power.*

pulses. This number is small compared with the $> 2.9 \times 10^4$ pulses observed in a similar cavity with filters of 0.9 nm of bandwidth, and a 3 dB spectral separation of 1.1 nm [16]. However, at 3.5 nm of filter bandwidth, the in-cavity eigenpulse energy is larger than this previous report by a factor of 70.

In a second configuration, the spectral width of the BPFs are maximized. At these bandwidths,

the filters BPF_1 and BPF_2 can be considered as high- and low-pass filters, respectively, as their leftmost and rightmost cutoff edges are outside of the gain window of the EDFAs. In this case, the pulse bandwidth is limited by the gain window on one side, and by a filter edge on the other, which permits pulsed operation as when a pair of BPF is used. For this configuration, Fig. 4.17(a) presents the output spectrum of the source in operation. The peak at 1530 nm is due to the unfiltered EDFA leakage, and BPF_2 fails to block the 1505 nm – 1515 nm wavelengths. Figure 4.17(b) and (c) show the simulated pulses profiles in the time domain, before and after filtering at BPF_1 and BPF_2. Because of the propagation in a dispersive HNLF, the spectral components of the pulses spread in time. Only the short wavelengths corresponding to the tail of the pulse are selected after BPF_1, while it is the opposite at BPF_2. Therefore, no single eigenpulse is sustained in the cavity, but rather the alternation of two pulses of complex profiles. As depicted in Fig. 4.17(d), such pulses do not converge towards Gaussians after dispersion compensation. The pulse energy of the filtered pulses of Fig. 4.17 is of $\sim$50 pJ. Because of SRS, large pulse-to-pulse fluctuations occur, and the autocorrelation trace of such pulses resembles the one of noise inside a Gaussian envelope. A positive third order dispersion coefficient leads to an asymmetry in the spectra broadened by SPM, tilting its top clockwise with respect to the central wavelength [189]. The HNLF generates a Raman replica of the pump pulses at the Stokes wavelengths when the pulse peak power is above the Raman threshold. This is due to a group-velocity matching provided at the wavelengths of 1550 nm for the pump and 1670 nm for the Raman signal. Because of the alternative filtering, the Stokes pulses are not sustained in the cavity, but rather rebuilt from noise at each passage through the nonlinear medium. The overlap between the spatial distribution of the pump and Stokes pulses is verified with a broadband InGaAs photodiode and a cascade of two 1310/1550 wavelength-division multiplexers. Each of the pump and Stokes wavelengths are alternatively filtered out: the filtering provides an attenuation in excess of 18 dB for each signal. Nevertheless, the pulses propagating in the cavity are visible in both cases, and their respective temporal distribution is similar. This effective transfer of energy towards the Stokes wavelengths induced by the long interaction distance turns into a drawback for the laser cavity efficiency. The energy of the pump pulses transfer towards the Raman pulses, thus leaving less power in the cavity. The polarization dependence of the Raman gain also introduces polarization dependent losses in the cavity, which is sensitive to external disturbances. In Fig. 4.18, the tunability of the source is investigated with the largest bandwidths enabled by the adjustable filters. As the filter offset increases, the number

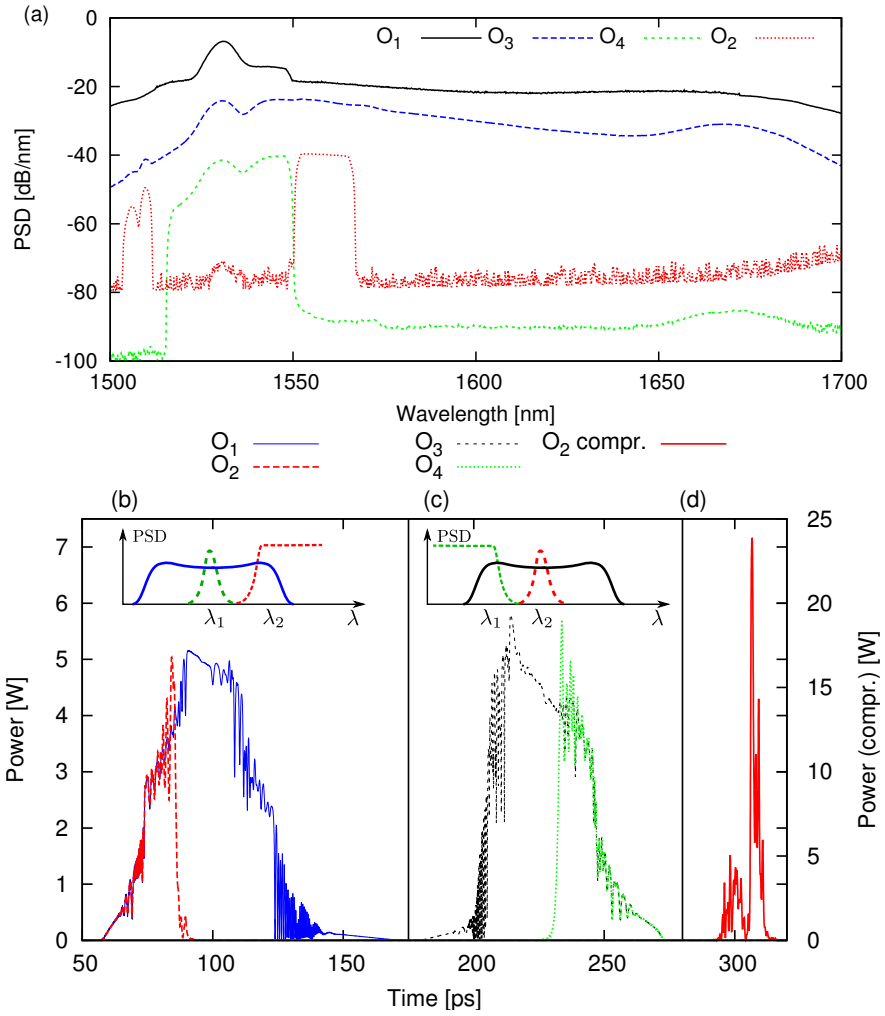

Figure 4.17 – *(a) Experimental spectra, observed before and after band-pass filtering. (b) Simulated pulse before and after filtering at BPF_2, (c) simulated pulse before and after filtering at BPF_1, (d) simulated pulse of (c) compressed by dispersion compensation.*

of pulses in the cavity first increases as the source efficiency increases. The PB regime is sustained up to a filter offset of 5.5 nm, instead of the ~ 18 nm predicted by simulations of [24], in case of Gaussian filters. The energy lost at the pump by SRS, as well as the sharp edges of the BPFs are responsible for this difference.

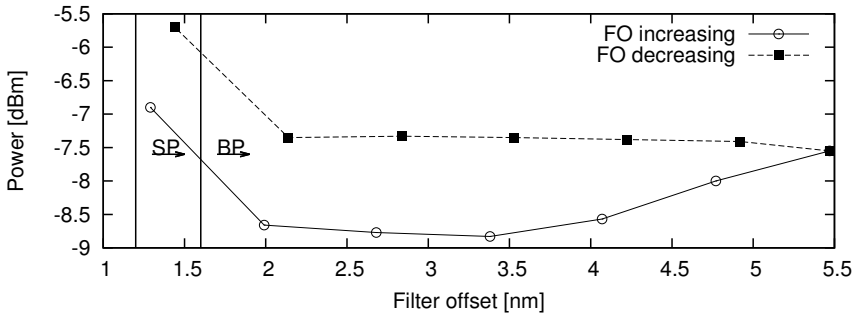

Figure 4.18 – *Domains of SP and PB as a function of the filter offset, at output O_3. FO: filter offset.*

4.4.2 Summary

Self-pulsating sources based on cascaded regeneration operate efficiently with BPFs larger than 1 nm, as suggested by numerical simulations in Section 4.3.1.

In [16], the shortest pulses observed without nonlinear compression were at their transform limit, with a duration of 3 ps and an energy of 0.17 pJ. By using large BPFs, near-transform limited pulses as short as 2 ps and with energies $20\times$ higher than previously reported are observed without compression or chirp compensation when the filter bandwidth attains 3.5 nm. After propagation in SMF and amplification, the pulses are compressed down to a duration < 0.5 ps.

By design, this source toggles in between two wavelengths, 1548 nm and 1553 nm, as well as generating pulses at 1670 nm via SRS in the HNLF.

When $\text{BPF}_{1,2}$ are a high- and a low-pass filter respectively, the gain window determines the spectral bandwidth of the pulses. A simplified cavity could be designed with such components, at the expense of the pulse quality. Despite the non-optimal filter shapes, pulses of 2 ps as well as pulses shorter than 0.5 ps are observed at the output of the cavity. Regenerative sources therefore operate at large filter bandwidths and are robust to non-optimal filter shapes.

4.5 Discussion & Conclusion

In this chapter, the performances of regenerative sources have been investigated. In contrast with previous work, the starting of self-pulsating sources based on cascaded regeneration was described, and indicates that the design of such sources of large filter bandwidth is a new candidate for the generation of ultrashort pulses of broadband spectra and good efficiency. Compared to previous work, shorter and more energetic pulses were generated. It can be expected that future work will focus on improving the source efficiency by reducing the effects of SRS, as well as including new nonlinear media to replace the silica fibers. In terms of pulse energy, simulations indicate that the pulse energy does not significantly increase when the number of pulses in the cavity decreases by increasing the filter offset. Therefore, achieving pulses several orders of magnitude higher than the nanojoule seems unlikely for regenerative sources based on SPM-OF regenerators. The effect of filtering, at which most spectral components are lost, prevents a strong rise of the pulse energy. However, an increased normal dispersion in the cavity may increase the pulse energy by stretching them temporally. Other improvements could lead to the creation of self-pulsating sources for the mid-infrared (MIR), to trigger ultrashort pulses. As of this year, tunable BPFs as well as thulium amplifiers are commercially available, and only the nonlinear medium should be well chosen or engineered in order to reach satisfying dispersion profile and nonlinearity value. The use of fiber tapers, for example, may lead to shorter cavities which operate at longer wavelength via rare-earth-doped fibers of parametric amplification. Since the pulse spectrum is composed of frequency components which have been generated by SPM, the source has no stable longitudinal modes, and is therefore expected to be modeless. Further experimental evidence of this fact would be helpful, since sensing applications would benefit of a source whose PSD is continuous over the pulse bandwidth. Finally, custom BPFs profiles may lead to the generation of eigenpulses of different shapes.

Chapter 5

Self-pulsating sources based on SSFS and SPM

5.1 Introduction

In Chapter 4, pulsed lasers based on a pair of complementary regenerators of type SPM-OF regenerators were introduced. Their architecture has interesting features including aperiodicity, low polarization sensitivity, and multiwavelength operation [16, 24]. Pulses propagating in sources based on that concept undergo large changes in their spectral and temporal profile twice per cavity round trip. As a result, their output feature invariant eigenpulses, which can be regarded as dispersion-managed solitons [66]. These sources do not belong to the class of mode-locked lasers, for which a fixed phase relationship is maintained between the spectral components. Consequently, the repetition rate of the output pulses is not constrained to a pulse-to-pulse time interval dictated by the cavity free spectral range or one of its harmonics.

Based on cascaded regeneration, a new method for generating short pulses in fiber lasers was proposed and demonstrated experimentally in 2012 [22]. Sources of that kind, referred to as self-phase modulation and offset filtering (SPM-SSFS) sources, are composed of two distinct regeneration stages. In the first stage, regeneration based on SPM-OF is followed by a second regeneration stage in which SSFS occurs during the generation of a SC. This SC is partially washed out by a red-shifted band-pass filtering, and the ring cavity is closed as the output of the second stage becomes the input of the first stage. Hence, the design of SPM-SSFS has similarities with

self-pulsating sources based on cascaded SPM-OF regenerators, which also feature wavelength toggling and alternating offset filtering. An interesting feature of SPM-SSFS sources is that they provide a broadband SC at one of their output, along with a tunable temporal burst duration which can be extended up to several hundreds of nanoseconds when the pump power is increased. Because of the presence of multiple and varying pump pulses, the SC generated by this type of source may be compared to SCs emanating from noise bursts [190, 191] or noiselike pulses [192].

5.2 Theoretical basis & experimental setup

Self-pulsating sources based on cascaded regeneration rely on two or more nonlinear stages whose function is to convert the propagating signal from one wavelength to another. When there are two nonlinear stages, the initial signal is shifted from the wavelength $\lambda_{1,2}$ to the wavelength $\lambda_{2,1}$ via nonlinear wavelength converters (NWCs), as depicted in Fig. 5.1. These NWCs must feature intensity dependent transfer functions and hence favor high intensities, triggering pulses. Regenerative sources solely composed of cascaded SPM-OF regenerators at $\mathrm{NWC}_{1,2}$ sustain pulses

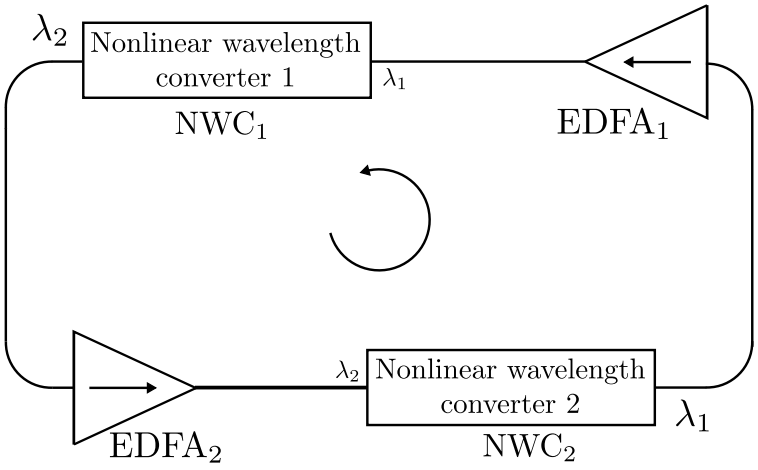

Figure 5.1 – *Setup of a generic self-pulsating source based on cascaded regeneration. EDFA: erbium-doped fiber amplifier.*

with a low amplitude jitter, due to the sharp transfer function that characterizes the SPM-OF regenerators placed in the cavity [149]. The temporal shape of the pulses is imposed by the spectral shape of the filters, via their Fourier transform plus an additional chirp, mostly linear

across the pulse. Figure 5.2 depicts such a regenerator. In fact, a remarkable property of SPM-OF

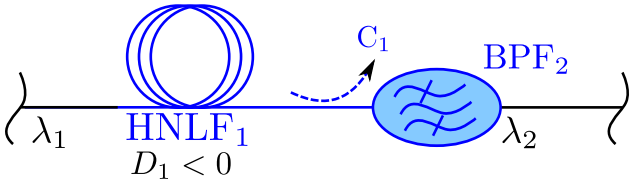

Figure 5.2 – *First nonlinear stage- SPM-OF regenerator. BPF: band-pass filter, HNLF: highly nonlinear fiber.*

regenerators is that at the first approximation, the output pulse peak power is independent of the input pulse power. Given that the latter is above threshold, the output peak power P_ω is expressed as [152]:

$$P_\omega \sim \frac{P_p}{\Delta\omega_{\text{SPM}}} = \frac{1}{\lambda}\Delta\omega_0 2\pi n_2 L \tag{5.1}$$

In Eq. (5.1), the output intensity is proportional only to the initial bandwidth ω_0, as well as the nonlinear propagation length L and the nonlinear coefficient n_2. The central wavelength is λ, $\Delta\omega_0$ is the input pulse bandwidth, $\Delta\omega_{\text{SPM}}$ is the bandwidth of the pulses broadened by SPM, and P_p is the input pulse peak power. Amplitude variations are, therefore, limited by this first nonlinear stage, which generates near chirp-free pulses at its output at small filter bandwidths, and linearly chirped pulses at larger spectral filter bandwidths [16].

In SPM-SSFS sources, the second NWC (NWC_2) is a HNLF with anomalous dispersion at the pump wavelength used in tandem with a BPF, as depicted in Fig. 5.3. Pulses input to this NWC undergo SSFS, induced by MI when their temporal duration is in the picosecond range [38]. By

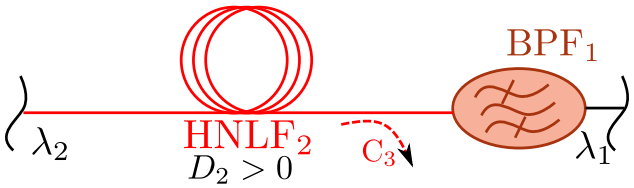

Figure 5.3 – *Second nonlinear stage: SSFS induced by MI and followed by selective filtering. BPF: band-pass filter, HNLF: highly nonlinear fiber.*

joining both nonlinear stages with EDFAs, the source self-ignites pulses from ASE, provided that the BPFs have an adequate relative spectral position, which is the subject of Sections 5.3.1 and 5.3.2.

The experimental setup of Fig. 5.4 is composed of two HNLFs of length $L = 1007$ m, two adjustable and tunable BPFs, centered at the wavelengths $\lambda_{1,2}$, and with tunable 3 dB bandwidths $\Omega_{1,2}$, respectively. The filters have sharp edges, as shown in Fig. 5.4(d), and a modification of their bandwidth only alters the length of their flat top portion. The filter offset is defined as $\Delta\lambda = |\lambda_1 - \lambda_2|$. The nonlinear fibers HNLFs$_{1,2}$ have a nonlinear waveguide coefficient $\gamma = 12.5$ W^{-1}km^{-1}, and a chromatic dispersion coefficient $D_1 = -0.71$ ps/(nm·km) and $D_2 = 2.09$ ps/(nm·km), respectively. Their third-order dispersion coefficients are $S_1 = 0.0074$ ps/(nm^2·km) and $S_2 = 0.002$ ps/(nm^2·km). Insertion losses are of 1.7 dB for each HNLF, 8 dB for BPF$_1$, 5.5 dB for BPF$_2$, and 0.5 dB for each output coupler, in addition to the power drawn by their output port. Two EDFAs are inserted between each nonlinear stage, with a saturation power $P_{\text{sat}} \approx 15$ dBm. The cavity output is observed via the four output tap couplers C_{1-4} with 12.5 GHz photodiode and a standard OSA.

In Fig. 5.5, the propagation of pulses is shown in the spectral and temporal domain after 18 cavity round-trips. The limit case where BPF$_1$ is a low-pass filter and BPF$_2$ is a high-pass filter is illustrated. Pulses from EDFA$_2$ are launched into HNLF$_2$, and interact by the conjugated effects of MI and FWM. These interactions give birth to fundamental solitons, which experience SSFS as illustrated in Fig. 5.4(c), where a powerful soliton shifts to a wavelength of ∼1630 nm. In the time domain, these solitons acquire a delay because of their different group-velocity in the anomalous dispersion regime. Low-pass filtering at BPF$_1$ do not extinct the significantly shifted solitons. However, they do not benefit from the gain of EDFA$_1$, nor pass through BPF$_2$. For other spectral components, SPM broadening occurs in the first few meters of the fiber, thereby resetting the central wavelength to λ_2, as depicted in Fig. 5.4 (b). The numerical model used to generate Fig. 5.5 includes the effects of second- and third-order dispersion $\beta_{2,3}$, nonlinearities, and the Raman effect ($T_R = 3$ fs), and is implemented as described in [24].

5.3 Experimental & numerical demonstration of the source operation

In this first series of experiments, a setup similar to the one of Fig. 5.4 is used. BPF$_1$ is composed of a circulator followed by a Bragg grating with bandwidth of 5.0 nm centered at $\lambda_1 = 1544.0$ nm.

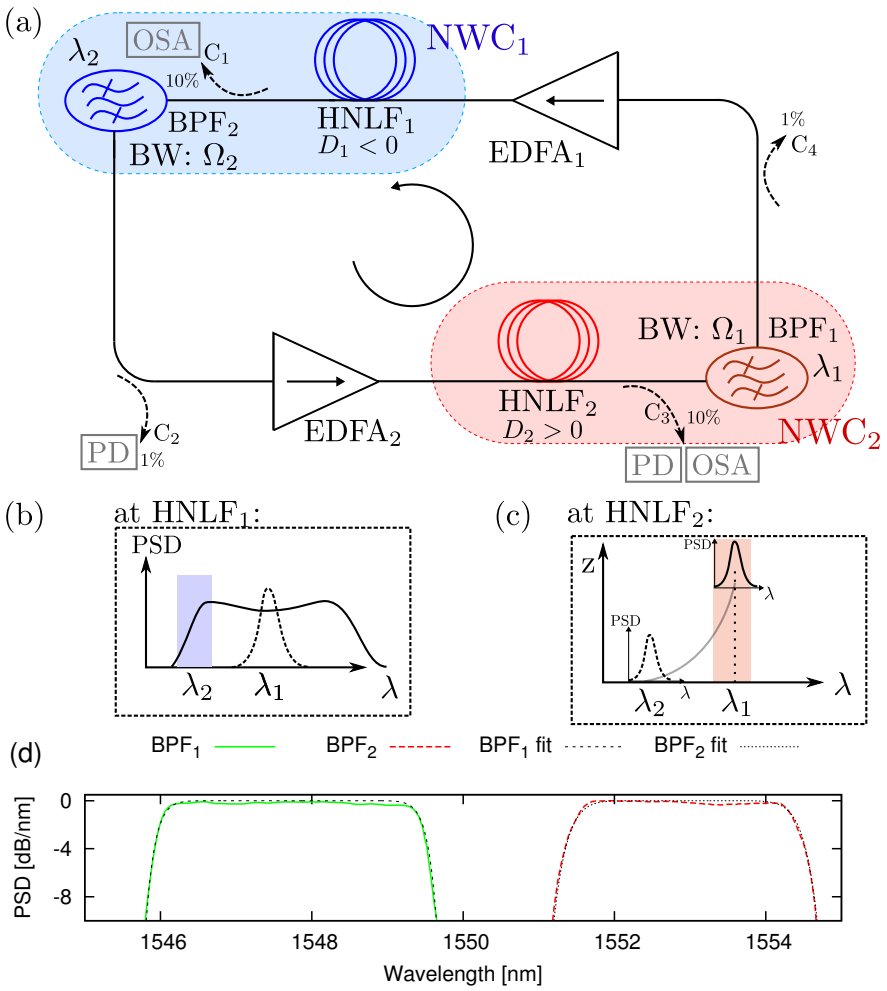

Figure 5.4 – *Closed-loop self-pulsating cavity. (a) Experimental setup of the SPM-SSFS source. (b) spectrum at the first nonlinear stage, with SPM broadening and offset filtering at λ_2. (c) SSFS and filtering at λ_1, in the second nonlinear stage, (d) Illustration of the filter profiles. BPF: band-pass filter, BW: bandwidth, HNLF: highly nonlinear fiber, EDFA: erbium-doped fiber amplifier, NWC: nonlinear wavelength converter, OSA: optical spectrum analyzer, PD: photodiode, PSD: power spectral density.*

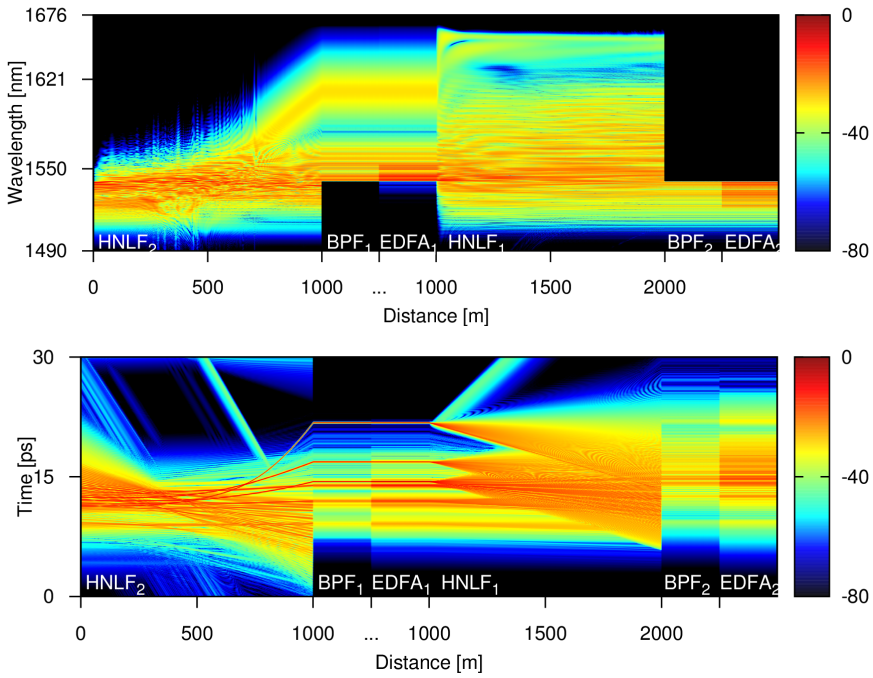

Figure 5.5 – *Propagation of pulses in the cavity of Fig. 5.4(a). Top: In the frequency domain. Bottom: in the time domain. The propagation length of the BPFs and EDFAs are increased for readability.*

The other regeneration stage includes a BPF with 6.2 nm of bandwidth centered at λ_2 =1550.5 nm.

In each half, various couplers C_{1-4} are used for monitoring purposes. Insertion losses are of 3.3 dB for the grating and optical circulator combination, and 9.9 dB for the tunable BPF.

The pulses propagating in the cavity are monitored spectrally using OSAs connected to 10% tap couplers $C_{1,3}$, and also monitored in time using a photodiode (PD) followed by an oscilloscope at the output of 1% tap coupler C_2.

5.3.1 Spectral and temporal observations

The source self-starts from the ASE of both EDFAs. The gain is initially set at 11.6 dB for $EDFA_1$ and 16.2 dB for $EDFA_2$. Figure 5.6 (a) and (b) show the spectra observed at outputs C_1, C_2 and C_3, while (c) and (d) show oscilloscope traces of the laser output as measured from C_2 and C_3 with the PD. The trace in (c) shows that the laser provides a burst of power at every 10.5 μs. Trace (d) shows that this burst is made up of a collection of short pulses in cascade. On inset (e), picosecond pulses are observed after the SPM regeneration process.

The SC observed at output C_3 originates from pulses that have experienced SSFS in $HNLF_2$, which is a required condition for a pulsed regime. It also appears from output C_1 that the pump pulses in $HNLF_1$ provide a Raman gain with a 13.2 THz offset with respect to the pump, and resulting ASE centered at 1664 nm. The absence of power at a wavelength of $\sim$1450 nm excludes the contribution of a degenerate four-wave mixing process at the pump. It was also observed that additional bursts of pulses similar to those shown in Fig. 5.6 (d) are created and sustained in the cavity when increasing the EDFAs gain.

The circulation of pulses in the cavity was simulated and indicates the possibility of single-pulse operation at low gains, and SC generation at higher levels of pump power in presence of multiple pulses. The propagation in both HNLFs was modeled using a split-step Fourier method including the effects of the nonlinearity, the second- and third-order dispersion terms, self-steepening and Raman scattering approximated to its first order differential term. Filtering was modeled with BPFs, and the EDFAs were modeled as perfect amplifiers with a saturable gain. To start the source, both white noise and Gaussian pulses used as a seed led to similar results. Figure 5.7 (a) and (b) illustrate solitons after $HNLF_2$ for the 50th cavity round trip. In the frequency domain, Fig. 5.7 (c) provides the spectra before and after propagation in $HNLF_2$, in agreement with the experimental result of Fig. 5.6 (b). Due to the filtering at λ_1, pulses that are entering $HNLF_2$ have a

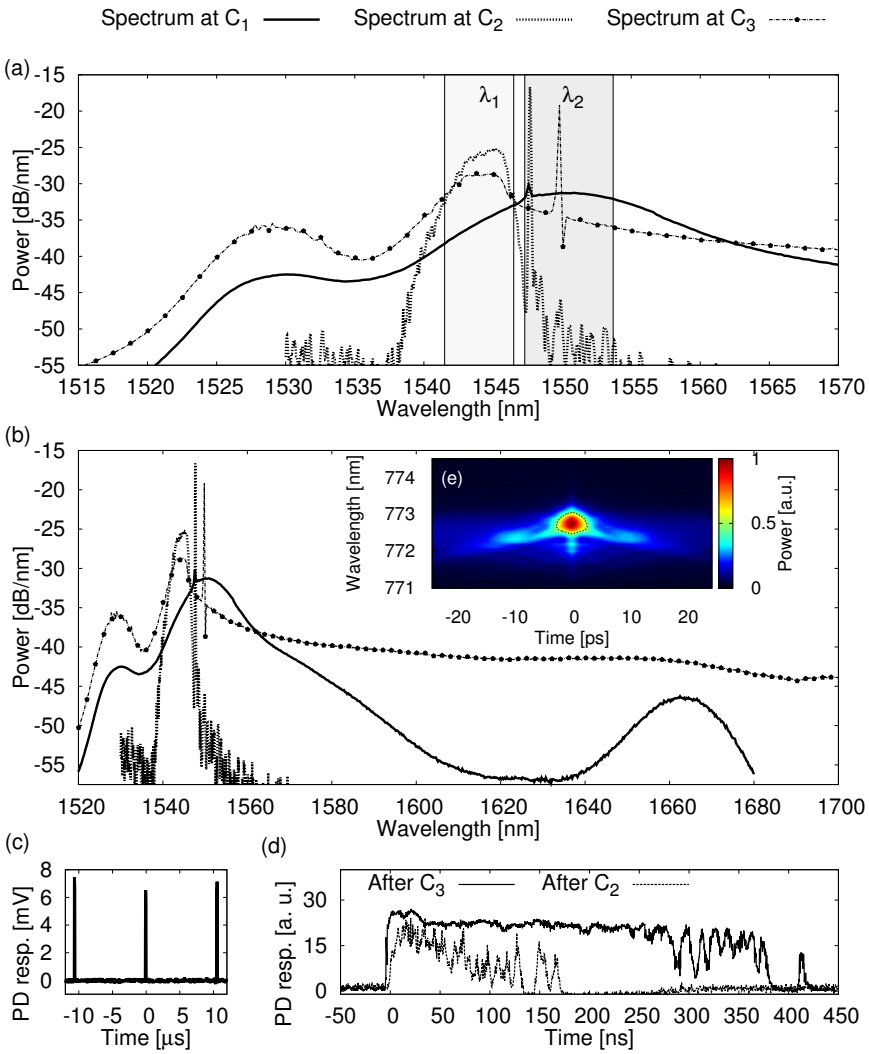

Figure 5.6 – *(a) and (b) Spectra from outputs C_1, C_2 and C_3, (c) observed from C_2, oscilloscope trace showing the repetition rate and burst structure of the output signal, (d) observed from C_2 and C_3, oscilloscope trace zooming on one burst and revealing a structure that comprises several pulses. Inset (e): frequency-resolved optical gating spectrogram at C_2.*

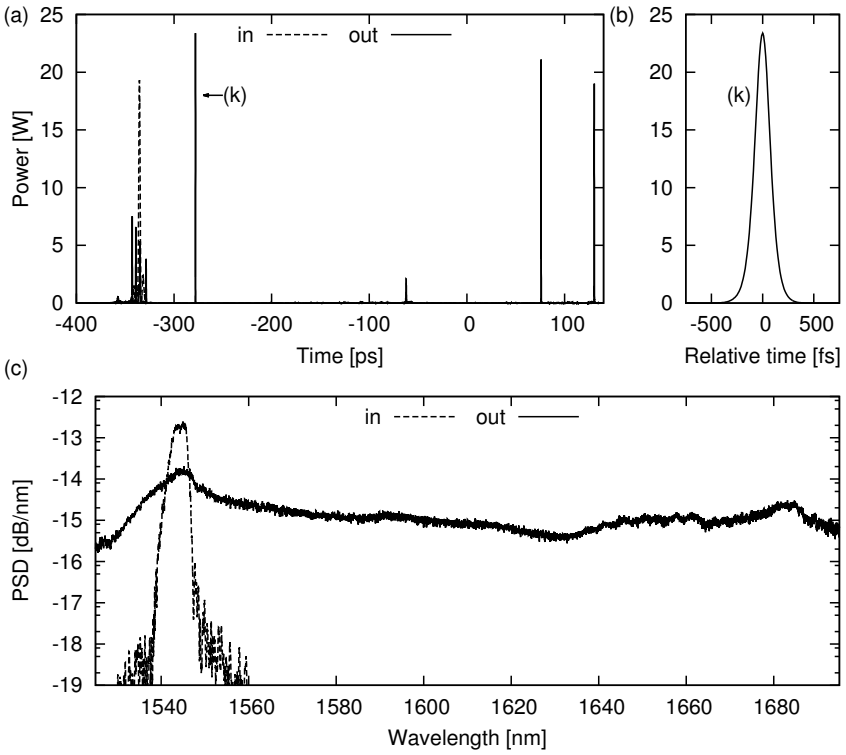

Figure 5.7 – *Numerical simulations for the setup of Section 5.3. (a) Fundamental solitons after $HNLF_2$, (b) Zoom on the output soliton (k), (c) Spectrum obtained by an averaging over 50 round-trips of the cavity, starting at round trip 10. The dashed and solid curves correspond to the input and the output of $HNLF_2$, respectively.*

FWHM duration of ∼1 ps but with a peak power of ∼20 W, which corresponds to a higher order soliton of $N \cong 5.5$. Hence, we observe soliton fission during the beginning of propagation in $HNLF_2$ [193]. New solitons of various FWHM duration and peak power co-propagate in the HNLF, with a group-velocity relative to their central wavelength, and an acceleration due to the SSFS induced by the Raman effect.

Figure 5.8 illustrates that soliton fission occurs within the first 20 m of propagation, leading to fundamental solitons. The slope of their trajectories is related to their group-velocity dispersion, and powerful pulses slow down as a result of intrapulse Raman scattering. This figure also illustrates that the accumulated delay of these solitons is responsible for the long burst of pulses experimentally observed in Fig. 5.6 (d).

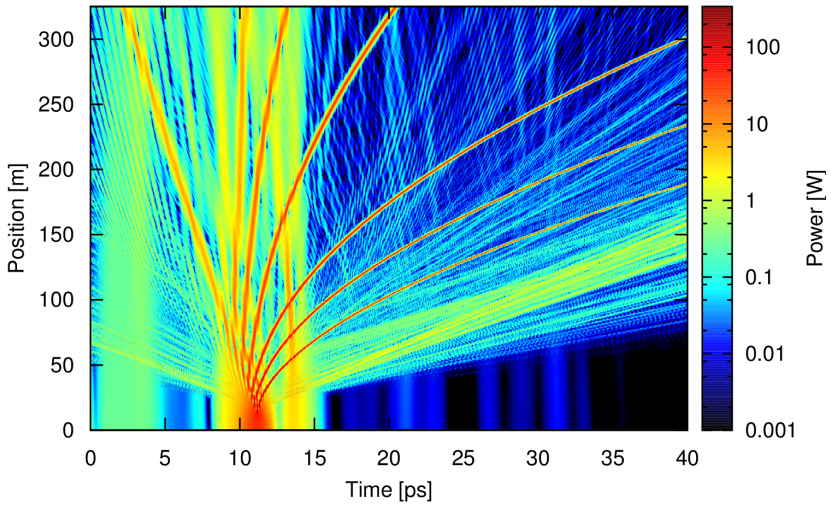

Figure 5.8 – *Soliton fission in the time-domain and propagation of the resulting fundamental solitons in the first 300 m of $HNLF_2$.*

The wide spectrum of Fig. 5.6 (b) and Fig. 5.7 (c) results from the propagation of several subpicosecond pulses in $HNLF_2$, which experience an amount of SSFS that depends on their own temporal width and peak power. Because the amount of SSFS is related to $1/t_{\mathrm{fwhm}}^4$ [67], only solitons with an adequate FWHM are selected by the BPF, and will be sustained by the cavity for

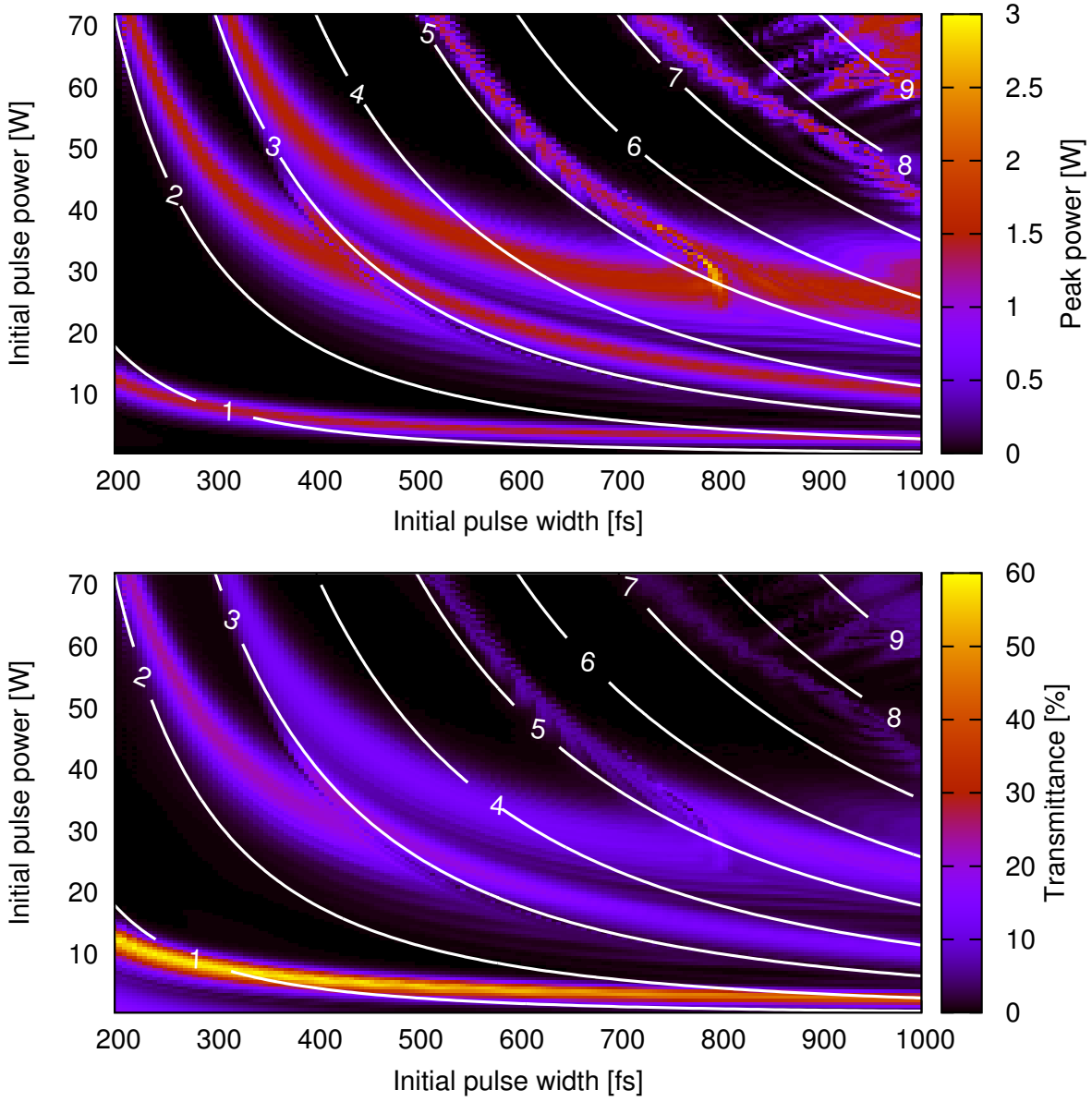

Figure 5.9 – *Pulses with an initial temporal width and peak power are launched in $HNLF_2$. (top) Their final peak power is represented after filtering at the BPF. (bottom) The transmittance at the filter is shown. For reference, solid lines indicate the corresponding soliton order.*

the next round trip. Fig. 5.9 (a) shows the peak power of pulses launched in $HNLF_2$ after filtering at the BPF, and (b) provides the associated transmittance at this BPF. Another pulse selection is performed at the regenerator, and the bandwidth of the fiber Bragg-grating (FBG) gives a first limit on the pulse temporal width. The observed pulse of Fig. 5.6 (e) is about 3 times longer than expected by simulation, and has pedestals because of the presence of multiple pulses in the cavity.

5.3.2 Effect of the filter bandwidths

The output properties of SPM-SSFS sources were studied in [22] for fixed filter spectral positions and bandwidths. The source was started from ASE, as the pump power of $EDFA_{1,2}$ was increased beyond a given power threshold. In this section, the operation of the source is shown for a wide range of filter spectral bandwidths, and pulses are triggered by altering the filter offset. At one limiting case, BPF_1 is a low-pass filter, and BPF_2 is a high-pass filter. Experimentally, this case is implemented by maximizing the bandwidth of the filters, so that they exceed the erbium gain window. At the opposite limiting case, both BPFs have a narrow bandwidth < 0.5 nm, and the source operates in a CW regime, with amplified fluctuations induced by MI. In this configuration, the propagation in $HNLF_2$ is comparable to the self-pulsating laser introduced by Lee et al. [194] which generates a broadband SC from MI in a ring cavity, except for the fact that the pump power is two orders of magnitude lower than the one reported in [194].

In Fig. 5.10, BPF_1 is a low-pass filter, and BPF_2 has a variable bandwidth. Self-pulsation occurs for a fixed EDFA pump power, by reducing the spectral separation between the BPFs, by red-shifting BPF_2. The green zone of Fig. 5.10(a) represents the maximal filter offset that induces self-pulsation. This zone has a maximal $\Delta\lambda$ when Ω_2 =3 nm. Figure 5.10(b) illustrates the continuum observed at C_3 for some of these configurations. For a BPF_2 bandwidth of 3.5 nm, the continuum generated at C_3 is maximized, and reaches wavelengths past 1900 nm. For larger and smaller bandwidths, less energy is transferred towards the long wavelengths. Hence, there exist an optimal spectral bandwidth of BPF_2 for which the captured spectral power density contributes optimally to sustain the existing pulses in the cavity. This particular case was illustrated in [25], in the case of regenerative sources. In such a situation, the pulses filtered at BPF_2 exhibit long temporal duration due to the accumulated dispersion, or contain a broad pedestal if compression is achieved by chirp compensation. The pulse energy is high due to the large amount of spectral components captured by the BPF, but it is spread over a long duration, which is non-optimal for SC generation.

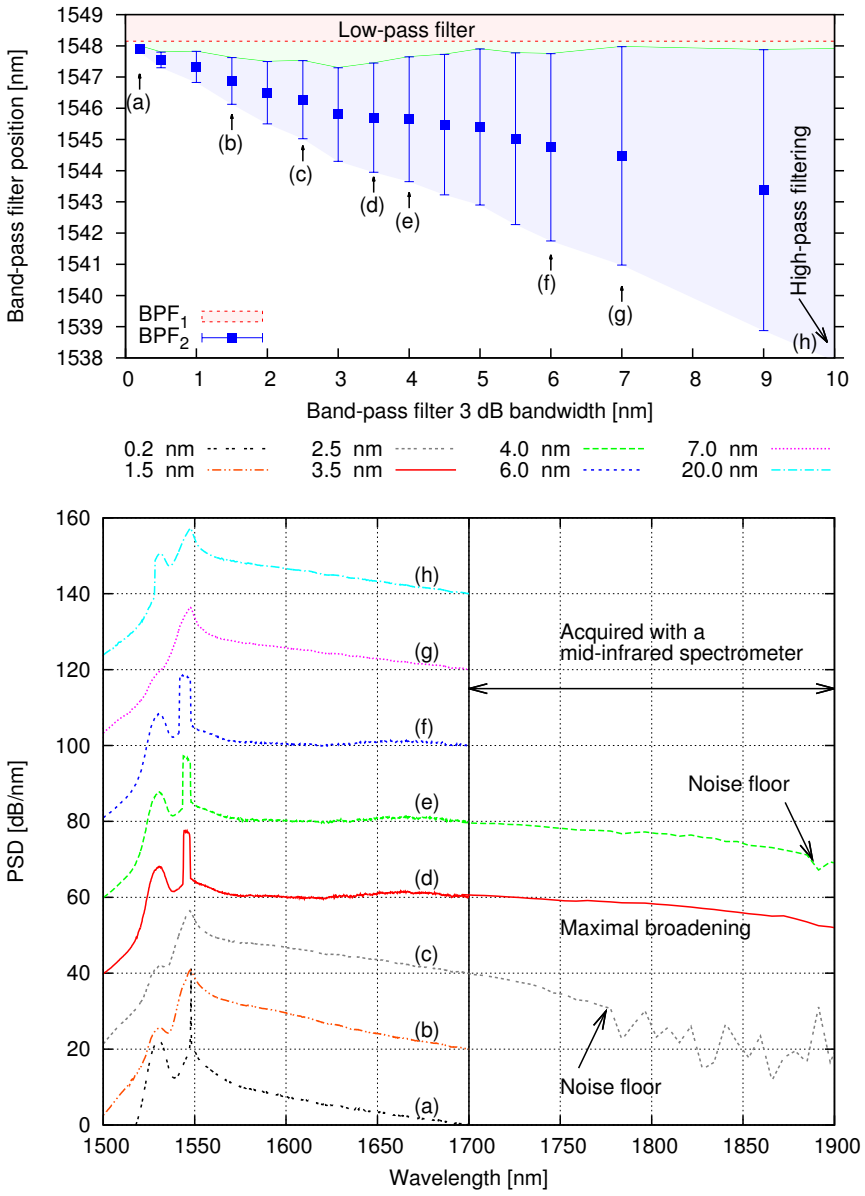

Figure 5.10 – *(a) Filter position for variable bandwidths of BPF_2. The spectral position of BPF_2 corresponds to the blue-most position which triggers pulses in the cavity. (b) Spectrum at output C_3 for different values of bandwidth of BPF_2. The leftmost part of the graph is acquired with a standard OSA, while the rightmost part of the graph is acquired with a NearQuest spectrometer of lower dynamic range, operating in the range 1000 nm to 2400 nm*

In a second set of experiments, the filter bandwidths are changed, so that $\Omega_1 = \Omega_2$ at all times. In Fig. 5.11, the position of each BPF is depicted. BPF_2 is first shifted towards the longer wavelength to trigger self-pulsation, and the output power at C_3 is recorded at that moment. Then, BPF_2 is shifted in the opposite direction, and the wavelength at which the source stops pulsating is recorded. For filter bandwidths of 4.7 nm, pulses are sustained in the cavity up to a filter offset

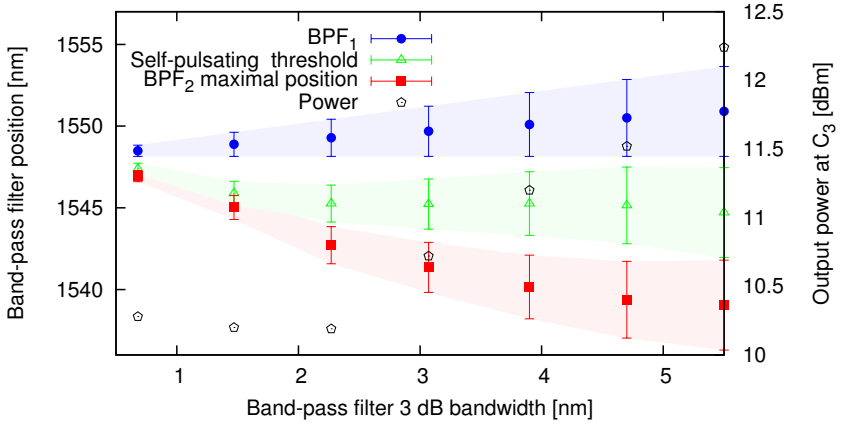

Figure 5.11 – *Operation of the SPM-SSFS source at several different filter bandwidths. The error bars represent the 3 dB bandwidth of the filters. The self-pulsating threshold position is depicted as well as the maximal spectral shift of BPF_2 that is reached without altering the source operation. The output power corresponding to the threshold is reported on the right axis.*

of $\Delta\lambda$ =3 nm. Spectrally, the continuum at C_3 shows insignificant changing when altering the filter bandwidths. Even for fiter bandwidths of 0.5 nm, which means large temporal pulse duration of ∼7 ps from the SPM-OF regenerator, SC generation is initiated in $HNLF_2$.

Overall, SPM-SSFS sources self-start from thin filter bandwidths of 0.5 nm to ultra-large bandwidths in the limiting case, when reduced to a pair of low- and high-pass filters. Optimal filter bandwidths maximize the source efficiency by blocking the spectral content which does not contribute to the pulses.

5.4 Single-shot spectral measurements

A wavelength-to-time mapping technique is used to capture the power spectral density of pulses originating from $HNLF_2$ [76]. Used recently to analyze supercontinua induced by MI or

noiselike pulses [19, 77], this technique relies on the fact that any pulse tends to turn into its Fourier transform when passing through a dispersive medium. When the third-order dispersion is small, the last term of Eq. (5.2) is negligible, and Eq. (5.2) provides a linear relationship between a time interval $\Delta\tau$, a wavelength interval $\Delta\lambda$, the chromatic dispersion coefficient D and the fiber length L.

$$\Delta\tau \approx DL\Delta\lambda + \frac{\mathrm{d}}{\mathrm{d}\lambda}DL(\Delta\lambda^2) \tag{5.2}$$

A spool of 21.64 km of SMF-28, for which this assumption holds, is used along with a real-time oscilloscope. The temporal duration of the observed signal must be small with respect to the time-delay corresponding to the signal bandwidth. Because SPM-SSFS source generate a burst of pulses at their output, it is necessary to reduce the burst duration to a minimal value. For this purpose, the EDFA pump power is decreased to shorten the duration of the temporal burst after the regeneration stage. Figure 5.12 presents a set of unrelated 30 single-shot spectra, when BPF_1 and BPF_2 have a bandwidth of 5 nm and 6 nm, respectively. This set of spectra reveals several peaks at various wavelengths, red-shifted with respect to the pump, which correspond to powerful solitons shifted by SRS. Figure 5.5(a) indicates that co-propagating solitons exchange energy as they collide with others [195–197]. The soliton temporal duration can be retrieved from their bandwidth at the output C_3. From the solitons of Fig. 5.12(a) whose FWHM is separated from other spectral components, the soliton temporal FWHM are of $\sim$120 fs to 200 fs, for a spectral bandwidth of 12 nm to 21 nm. As indicated by Fig. 5.12(a), a small amount of energy is nevertheless transferred to the longer wavelength, up to 1700 nm, revealing the presence of solitons of short temporal duration whose frequency shift is proportional to $1/t_{\mathrm{fwhm}}^4$ [67]. The shifting rate is also potentially raised by collisions with other solitons generated by MI [197]. The randomness characteristics of SC generation induced by MI imply that the energy contained in the cavity is not constant, contrary to mode-locked lasers or sources based solely on cascaded SPM-OF regenerators. The offset filtering periodically reduces the number of pulses, and the total pulse energy varies as depicted in Fig. 5.13.

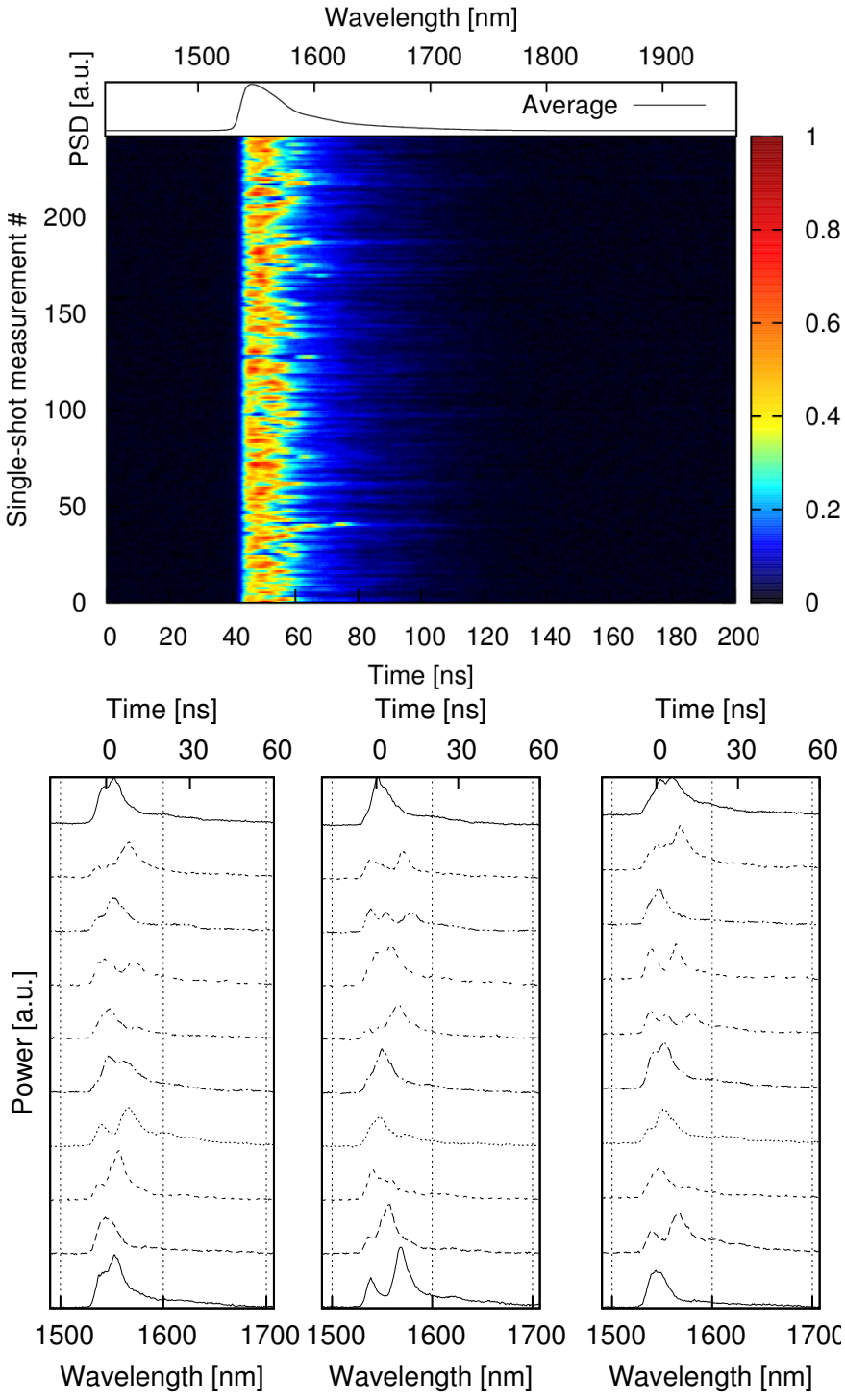

Figure 5.12 – *(a) Single-shot measurements of the spectrum at C_3. (b) Spectra corresponding to 30 independent single-shot measurements of (a).*

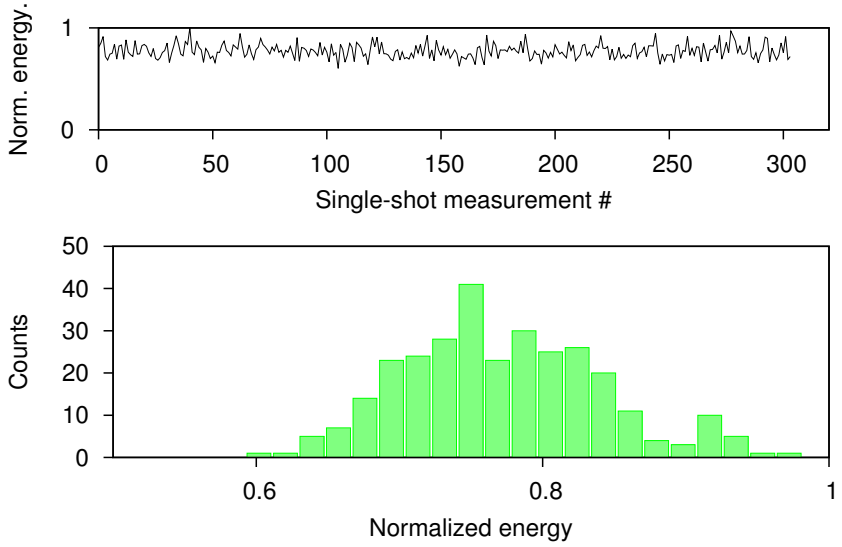

Figure 5.13 – *Energy retrieved from single-shot measurements, integrated from the time-domain spectral measurements.*

5.5 Supercontinuum-free operation

The operation of SPM-SSFS sources according to the setup of Fig. 5.4 is such that the pulse input to $HNLF_2$ is chirped, in the picosecond range, and energetic. This pulse is split into several fundamental solitons, drifting with various amounts of spectral shifts. Most of the time, these solitons are therefore rejected by BPF_1. If BPF_1 is a low-pass filter, the solitons are sustained in $HNLF_1$ but rejected at BPF_2, because their spectral broadening by SPM is insufficient to transfer energy back to λ_2. In this case, the source efficiency is limited as illustrated by the SC observed at C_3.

However, are SPM-SSFS sources able to generate and sustain a single pulse, which could undergo SSFS and transfer most of the energy from the short towards the long wavelengths? To answer this question, the setup of Fig. 5.4 is altered by the addition of a dispersion compensating fiber after $EDFA_2$. Chirp compensation therefore decreases the pulse input to $HNLF_2$ below the picosecond. At such pulse duration, propagation in $HNLF_2$ enables SSFS of a single soliton, because the effects of MI and FWM do not prevail [198].

Simulations conducted with various filter bandwidths, gain and saturation indicate that single-pulse operation is supported by the cavity. However, the source is not self-starting in this config-

uration. To trigger pulses, the required saturation energy leads to higher order solitons of $N > 2$ input to $HNLF_2$, contradicting the requirement for single-pulse operation. Nevertheless, if a pulse seed is launched in a cavity with adequate amplifiers, the SPM-SSFS source reaches a steady-state, sustaining picosecond pulses in $HNLF_1$, and subpicosecond in $HNLF_2$. Figure 5.14 illustrates the steady-state propagation of a single pulse inside the cavity, in the time and frequency domains, after 10 cavity round-trips. The BPFs are Gaussian, with a FWHM bandwidth of 5 nm, and their spectral separation $\Delta\lambda$ =10 nm. The saturation power of $EDFA_{1,2}$ are of 0.075 dBm and 2.11 dBm, respectively. A length of 42 m of single-mode fiber compensates for the dispersion in $HNLF_1$. In

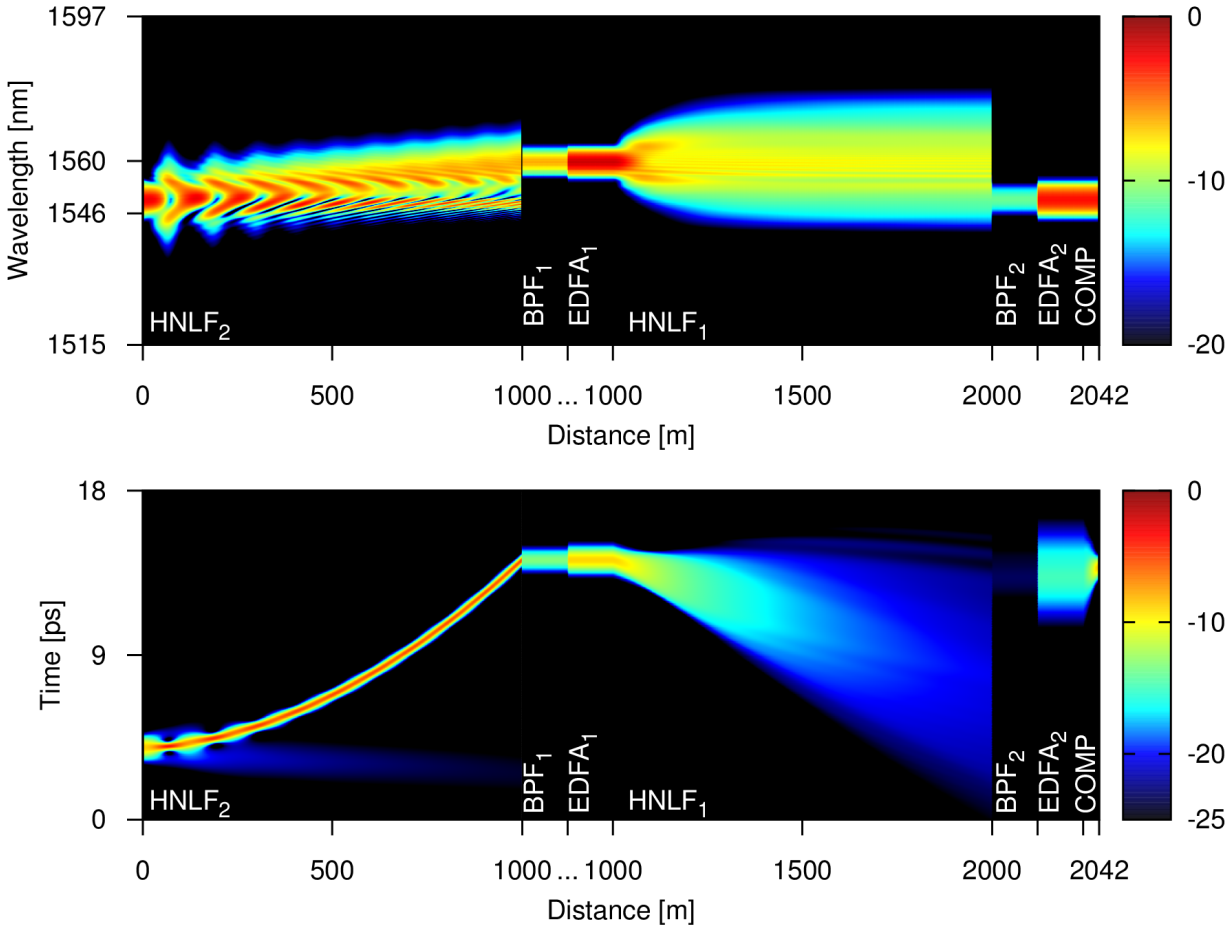

Figure 5.14 – *Propagation of a single pulse in the cavity. (a) In the frequency domain, (b) in the time domain. The propagation length of the BPFs and EDFAs are increased for readability.*

this configuration, 37% of the power input to $HNLF_2$ passes through BPF_1. The SPM-OF regenera-

tor is less efficient, and passes 14% of the resulting power. The soliton sustained by $HNLF_2$ has a FWHM duration of 300 fs.

5.6 Summary & Conclusion

The operation of self-pulsating sources based on SPM-OF regenerators as well as SSFS followed by offset filtering is characterized temporally and spectrally.

The conditions for pulse ignition and SC generation were investigated experimentally from the influence of filters in the cavity. The range of operation of this cavity is broad, and the bandwidth of BPF_2 has a direct influence on the width of the SC generated at C_3. Results provide the optimal filter bandwidth that maximizes the output SC bandwidth as well as the total output power. The optimal filter bandwidth of 3.5 nm leads to a broad SC, which extends past 1900 nm, and potentially further with the use of a HNLF pumped closer to the zero-dispersion wavelength than the one currently used. A spectrally narrow BPF_2, on the other hand, leads to an operation regime close to the one of CW SC sources. These SCs, seeded by picosecond pulses, are extremely sensitive to initial conditions, and therefore their output spectra are unique [199]. Numerical simulations were conducted, and show that the architecture of SPM-SSFS sources can sustain pulses in a SC-free regime, by avoiding the generation of multiple solitons. In this case, the source efficiency is maximal, and subpicosecond pulses are readily available at one cavity output.

The experimental setup of this source may be simplified at the expense of a maximized output continuum by replacing the BPFs with low- and high-pass filters.

Single-shot measurements illustrate that the mechanism of pulse generation in $HNLF_2$ is induced by MI and FWM. This process is stochastic, and the SC produced at C_3 is the time-average of several solitons, shifted by SRS. The source itself hence exhibits a stochastic behavior, and the energy sustained in the cavity is time-dependent, contrary to mode-locked lasers with output pulses of constant energy. Application such as random-number generation or chaotic LIDARs could benefit of such an architecture.

Chapter 6

Design of broadband noiselike pulsed sources

In this chapter, the design of two all-fiber ring cavities supporting the NLP regime are presented. In a first configuration, the use of chalcogenide fiber is investigated [21], and dual-wavelength noiselike pulse generation is demonstrated in the second configuration [23].

6.1 Introduction

Fiber ring lasers produce short and powerful pulses when passively mode-locked using NPR [200] or saturable absorbers [201]. In the particular case of NPR, the combined effects of XPM and SPM lead to a nonuniform rotation of the polarization state across the pulse. As a consequence, the combined effect of NPR and a polarizer shortens pulses at every cavity round-trip by transmitting their highest intensity components and attenuating their wings[88], as described in Section 2.4.2.3. It has been shown that the total dispersion in a NPR-based ring dictates the minimum achievable pulse width [202], and pulses as short as 77 fs have been generated in a dispersion-compensated fiber cavity [32]. The temporally stretched pulse avoids excessive nonlinearities, and the APM mechanism is therefore not saturated. In fact, in order to avoid the deterioration of pulses, the nonlinear phase shift experienced by the pulse must remain under a maximum of 2π [203, 204]. However, when it is not the case, ring cavities may operate in another kind of regime, often referred to as the NLP regime [18]. Instead of sustaining a soliton, wave packets composed of a

picosecond envelope comprising femtosecond-scale oscillations circulate inside the cavity.

This regime has been recently studied in various cavity configurations which do not always support soliton-like mode-locking [205, 206]. Spectrally, the averaged noisy pattern corresponding to each of those wave-packets can be visualized as a smooth and wide spectrum. In the past two years, noiselike pulses have been studied from a different point of view, and are treated as optical rogue waves, which allows to a certain extent the comparison with large amplitude ocean waves [207]. Through this more fundamental approach, statistics based on numerical simulations have shown that mode-locked lasers are actually an interesting mechanism for the formation of optical rogue waves, resulting of nonlinear interaction and collisions of the propagating wave packets [208–210].

Experimentally, several groups have reported noiselike pulses of large bandwidths in various gain media and cavity configurations [151, 205, 206, 211–218]. Starting from 44 nm in 1997, the addition of nonlinear or dispersion compensated fiber, birefringence, FWM and SSFS have been reported to extend that spectrum beyond 100 nm FWHM. The record is currently hold by Vazquez-Zuniga et al. in a 22 m long cavity including a segment of HNLF in normal dispersion [20]. Their Raman-extended NLP regime stretched out the spectrum towards longer wavelengths by SRS, leading to a 135 nm flat SC.

Noiselike pulses are highly energetic and resistant to nonlinear effects [219], and hence have found various applications that take advantage of their broad spectrum, including optical data storage [220], temperature distribution measurements [221], the characterization of fiber Bragg gratings [222, 223], and SC generation [192, 212].

In this chapter, two cavity configurations are studied. The first one is a ring laser including a segment of chalcogenide As_2S_3 fiber, and the second one comprises a HNLF in normal dispersion. In the first configuration, both a noiselike and solitonic regime can be triggered, which permits an indirect measurement of the chromatic dispersion of the chalcogenide fiber. The second configuration takes advantage of SRS to generate broadband pulses at two wavelengths.

6.2 Mode-locked and noiselike pulses in a ring cavity comprising a segment of chalcogenide fiber

Previous reports of mode-locked fiber lasers using chalcogenide fiber include only one paper, a chalcogenide fiber ring laser where chalcogenide serves as a host for neodymium. It has a self-pulsing behavior at 1080 nm with 0.2 μs pulses, whose origins are related to a saturable-absorption effect in the doped fiber [224].

In this section, we present a new cavity using chalcogenide glass as the nonlinear medium for self-pulsation in the solitonic and noiselike regimes. The high nonlinearity provided by the chalcogenide glass enables the formation of pulses at low peak power. This is potentially much valuable in designs with a gain medium of low saturation power, which occurs when compactness is a primary requirement. In addition to its high nonlinearity, chalcogenide glass is also transparent in the MIR and thus a laser design similar to the one presented here could be used for the fabrication of MIR lasers. For example the chalcogenide fiber could be used not only for NPR, but also as a gain medium via FWM or the Raman effect. Another option consists of doping the chalcogenide glass (eg. Cr^{2+}/Fe^{2+}/Tb^{3+}) to provide gain [225, 226].

By adjusting the polarization states in the cavity, a NLP regime also appears, and provides broadband pulses exceeding 50 nm FWHM.

6.2.1 Experimental setup of the laser

Fig. 6.1 shows a schematic of the fiber ring laser. It comprises an EDFA, a segment of As_2S_3 fiber, two PCs, and a polarizer. A coupler O_1 extracts 1% of the power out of the loop for monitoring purposes. The As_2S_3 fiber has a length L_c = 19.5 cm with a fiber nonlinear parameter γ = 0.16 $W^{-1}\,m^{-1}$, a material dispersion coefficient $\beta_{2,\mathrm{AsS}}$ =522 $ps^2\,km^{-1}$, and a numerical aperture NA = 0.23. NPR takes place in that short segment of fiber having a γ parameter ~ 1000 times that of standard silica fiber. The As_2S_3 fiber is pigtailed to standard silica fibers using UV-cured epoxy, with a total insertion loss of 4.5 dB due to Fresnel reflection and mode mismatch. However the mode mismatch could be completely eliminated with an appropriate adjustment of chalcogenide fiber core radius. In this case, it is expected that the insertion loss could be reduced down to the Fresnel losses, that is 0.54 dB from $n_{\mathrm{AsS}} = 2.4$.

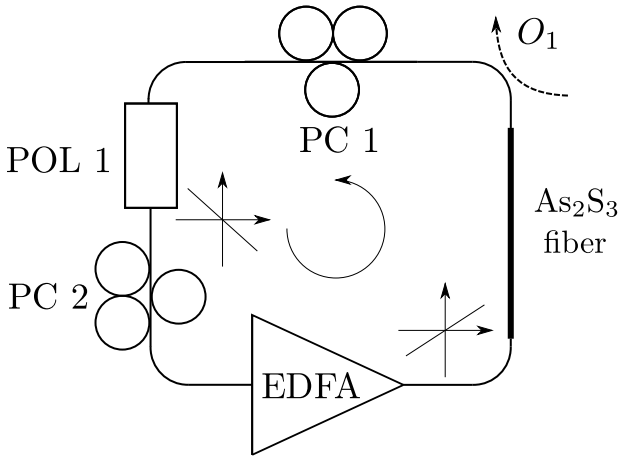

Figure 6.1 – *Schematic of the As_2S_3 fiber ring laser and its polarization states.*

The EDFA is composed of ∼10 m of erbium-doped fiber, with a material dispersion coefficient $\beta_{2,\text{edfa}} = 5\,\text{ps}^2\,\text{km}^{-1}$. The EDFA has a built-in isolator which conveniently ensure self-starting of the laser cavity [203]. The PCs are adjusted until self-pulsation occurs, in which case the round-trip losses for the CW light becomes higher than for the pulsed light. Fig. 6.2 illustrates the mechanism of NPR along the pulse profile, which after passing through a polarizer leads to pulse shortening.

6.2.2 Results

A proper adjustment of the PCs leads to self-pulsation, spawned by NPR. The repetition rate of the laser is 10.42 MHz, which corresponds to a cavity length $L_1 = 19.9$ m. Two different regimes are observed, each with their own spectral and temporal properties. The first regime has a typical solitonic spectral shape including sidebands, typical of fiber lasers with average anomalous-dispersion, and will be referred to as the solitonic regime. Appearing with a different PC adjustment, the second regime has a wider and flatter spectrum, without sidebands.

6.2.3 Solitonic regime

Fig. 6.3 shows the spectrum in the solitonic regime, centered at a wavelength of 1560 nm. Sharp sidebands are present, as a consequence of the spectrum superposition between solitons and dispersive waves. Sudden variations of both the dispersion coefficient and the nonlinearity as well as sudden variations of the pulse power due to an unperfect coupling prevent the soliton

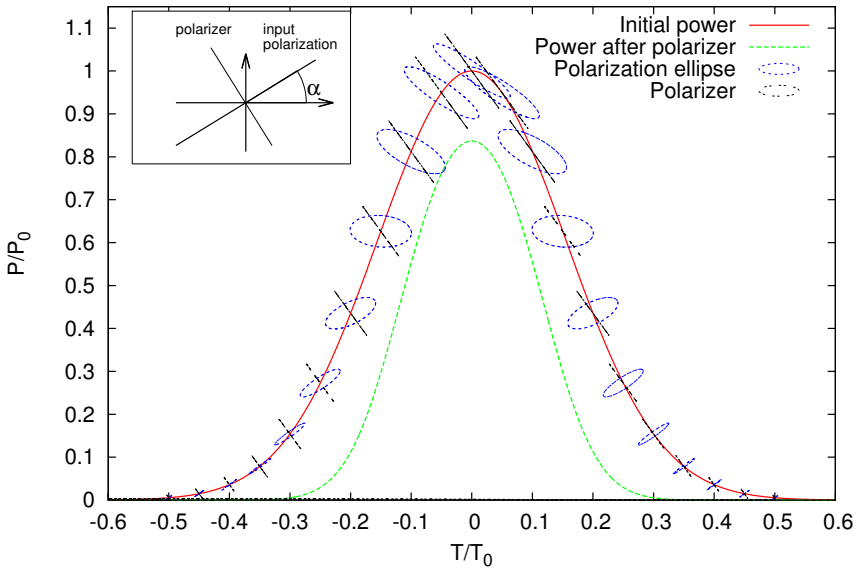

Figure 6.2 – *Illustration of the mechanism of NPR and filtering by the polarizer. (a) initial power profile with linear polarization at angle α. (b) Power through polarizer. (c) polarization state along the pulse profile, after NPR. (d) polarization axis of the polarizer at angle $\alpha + \pi/2$.*

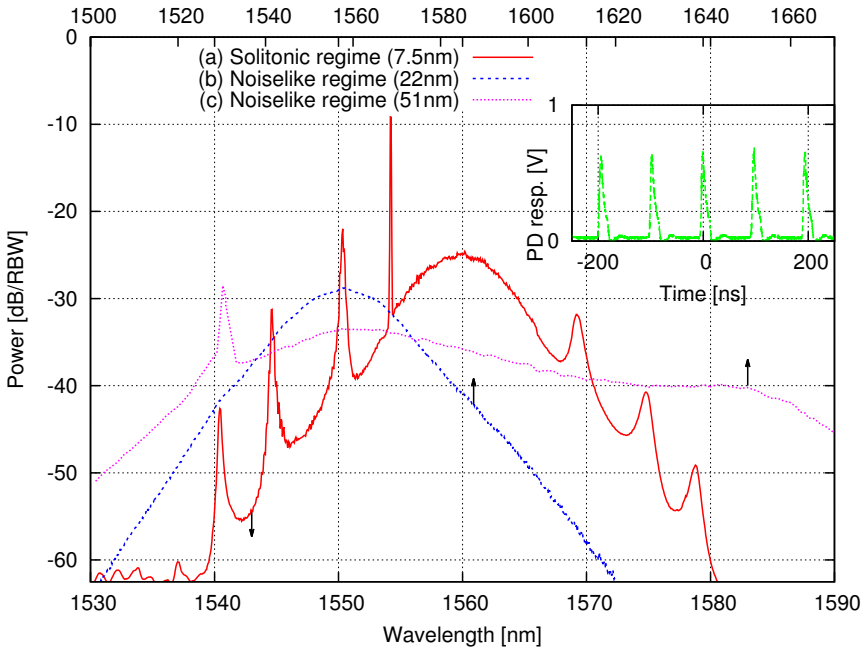

Figure 6.3 – *(a) Fiber laser spectrum operating in a solitonic regime. (b) and (c): operation in a regime of noiselike pulses. Subplot: Photodiode response at output* O_1.

from adapting adiabatically [227]. Apart from the peak at 1554 nm which corresponds to a co-propagating CW signal, the sidebands are relatively strong [228]. This is a good indication that the minimal pulse width has been reached, itself determined by a small average anomalous dispersion in the cavity. Linearly chirped $\sim$1 ps long pulses with an energy of E_s =37 pJ are measured with the frequency resolved optical gating device, as shown in Fig. 6.5. With sufficient dispersion compensation, the pulses could be recompressed down to 340 fs, while leaving no residual chirp.

From the spectrum of Fig. 6.3, both the average second- and third-order dispersion terms can be inferred. According to [202], the N^{th} sideband position in a solitonic regime is determined by the dispersion terms β_2 and β_3, the pulse width τ, the cavity length L and the frequency offset to the central pulse wavelength $\Delta\omega$:

$$N = -\frac{L\beta_2}{4\pi}\left[\Delta\omega_N^2 + \frac{4\ln^2\left(1+\sqrt{2}\right)}{\tau_0^2}\right] - \frac{L\beta_3}{12}\Delta\omega_N^3 \tag{6.1}$$

By solving Eq. (6.1) for each discernible N, the optimal parameters for the second- and third-order dispersion, plus the pulse width, are calculated using a nonlinear conjugate gradient algorithm. Applied to this setup, we obtain τ =326 fs, $\langle\beta_{2,\text{AsS+silica}}\rangle$ =−7.6 ps^2 km^{-1}, and β_3 =0.03 ps^3/km. Figure 6.4 compares the experimental results with the best fit obtained out of Eq. (6.1). It must be pointed out that a more accurate value of β_3 could be obtained by making a fit of several measurement with varying cavity lengths.

Moreover, the information carried by the sidebands can be exploited by comparison with a similar setup, except for the absence of the chalcogenide fiber. The average second-order dispersion term is readily obtained for that second cavity, and takes into account the dispersion in the EDFA, and in the silica fiber segments for a total of $\langle\beta_{2,\text{silica}}\rangle$ =−12.80 ps^2 km^{-1}. From Eq. (6.2), it is therefore straightforward to derive an expression for the second-order dispersion of the As_2S_3 fiber:

$$\langle\beta_{2,\text{silica}}\rangle L_2 + \langle\beta_{2,\text{AsS}}\rangle L_c = \langle\beta_{2,\text{AsS+silica}}\rangle L_1 \tag{6.2}$$

With L_2 =19.7 m the cavity length of the second cavity. In agreement with the expected values [229], we evaluated $\langle\beta_{2,\text{AsS}}\rangle$ = 517.3 ps^2 km^{-1}.

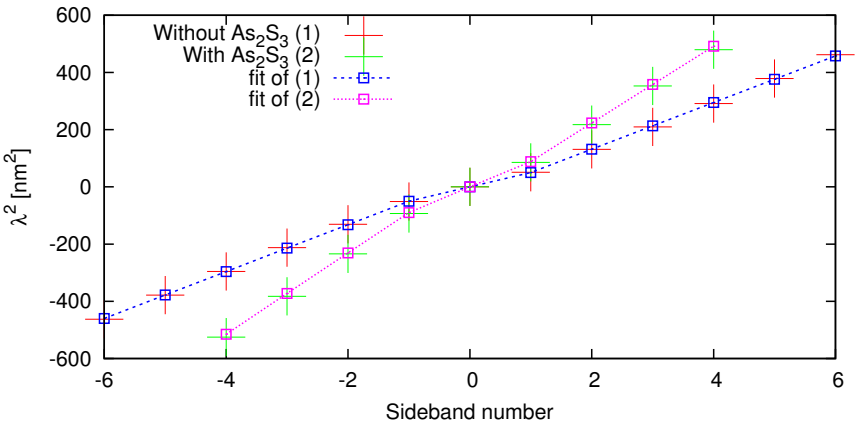

Figure 6.4 – *Sideband positions for both cavities. The second-order dispersion basically determines the slope of the squared wavelength offset to the pulse center. The small discrepancy visible at the first sidebands is due to the relatively short pulse duration τ_0 of equation Eq.* (6.1).

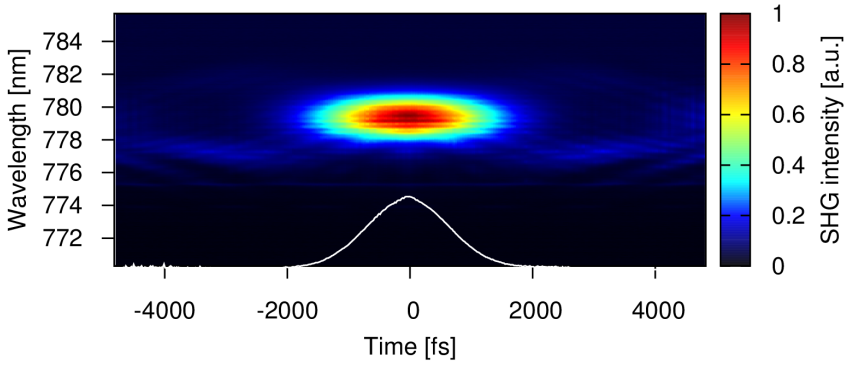

Figure 6.5 – *Spectrogram of a pulse observed at O_1 with a FROG.*

6.2.4 Noiselike pulse regime

The noiselike pulse regime provides a wide spectrum that stretches with respect to the PC tuning, as shown by the line (b) and (c) of Fig. 6.3. As it can be observed on the autocorrelation trace for this regime on Fig. 6.6, no structured pulse can be retrieved from that regime, but rather noise at a femtosecond scale inside a picosecond envelope [205]. The temporal envelope of these noiselike pulses are of 45 ps.

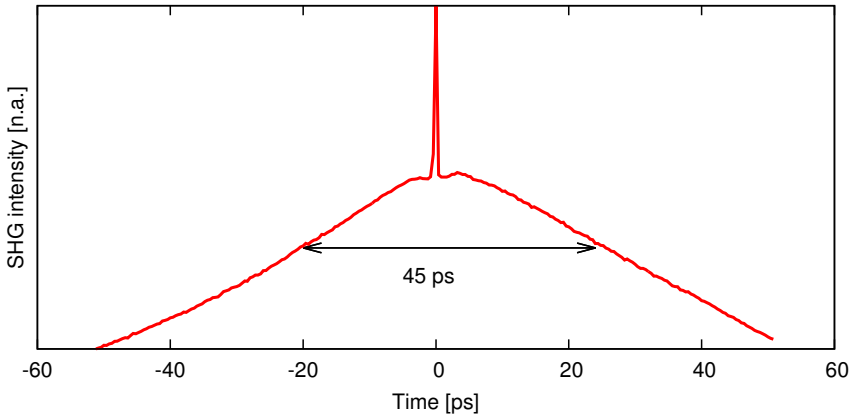

Figure 6.6 – *Autocorrelation of noiselike pulses.*

The large bandwidth observed is a consequence of this complex pulse pattern, while its smooth profile is due to the fact that the spectrum analyzer performs an averaging over many spectra of these noiselike pulses. The origins of this regime is still unclear [205].

However, the relatively high energy $E_n = 3$ nJ of these noiselike pulses of large bandwidths is interesting in application requiring low coherence.

6.2.5 Summary

Passive mode-locking via NPR was achieved in a chalcogenide fiber, leading to picosecond chirped pulses. Two different regimes could be observed. As expected in anomalous dispersion, a solitonic regime with sidebands was observed, providing information about the average dispersion in the cavity [202].

The information carried by these sidebands was used to derive an accurate value of the material dispersion coefficient $\langle \beta_{2,\mathrm{AsS}} \rangle$ in the chalcogenide fiber. Due to the low level of dispersion involved,

this can hardly be achieved with other methods that require significant power levels or require the single-mode condition [230, 231]. We note that the high normal dispersion of As_2S_3 compensates by 40% the average dispersion provided by the silica fiber portion of the ring cavity. Further optimization of the cavity by reduction of the silica fiber could lead to the generation of shorter pulses. The use of chalcogenide fiber, facilitating XPM during NPR also enables the generation of pulses at low pump power. However, this advantage is hidden by the large loss induced by the coupling to SMF fiber.

In the noiselike regime, the pulse bandwidth attains 51 nm. The addition of chalcogenide fiber increases this bandwidth significantly compared to the all-SMF-28 setups of Horowitz et al. [18] or Tang et al. [213]. However, this bandwidth are still much lower than the one obtained by Zhao et al. [214, 215] because no fiber of the setup is operating close its ZDW. Therefore, the effects of SSFS and XPM are less likely to transfer energy towards the long wavelengths. Nevertheless, the bandwidth achieved in this configuration is large when reminding the large cavity loss induced by the chalcogenide fiber.

6.3 Dual-wavelength noiselike pulse generation in a ring laser

In this section, the operation of a ring laser in noiselike regime is presented. The laser operates at two distinct wavelengths: the pump wavelength is in the C-band and takes advantage of erbium as gain medium, while the second wavelength of oscillation is triggered by SRS, in the U-band.

6.3.1 Introduction

Dual-wavelength operation regime was reported for the first and only time by Horowitz and Silberberg. [219]. This dual-wavelength oscillation was attributed to birefringence-induced loss modulation, and was demonstrated using a 450 m long silica cavity, with a spectral offset of 25 nm.

We present an all-fiber ring laser architecture sustaining dual-wavelength pulses in the NLP regime. The laser emits pulses at a wavelength of $\sim$1550 nm, the Raman pump (RP) pulses, from NPR in a cavity comprising an EDFA while pulses at a wavelength of $\sim$1650 nm, the Stokes pulses, are generated from a Raman effect. In [20], the addition of a HNLF increased the amount of SRS

experienced by the NLPs, therefore widely broadening their spectrum. By taking advantage of a nonlinear length $\sim$100$\times$ shorter than the one proposed in [20], we demonstrate that the action of SRS is reinforced, and instead spawns powerful pulses beyond 1650 nm, outside the amplification region or Er^{3+}-doped silica fibers. In a first regime, an efficient energy transfer from the RP signal to the Stokes signal is observed, such that the Stokes pulses exceed the RP pulses power by 2.5 dB. By single-shot spectral measurement, a technique described in Section 2.4.1.3, we verify the nature of the noiselike pulses.

In a second regime, a flattened dual-wavelength and broadband spectrum is generated, extending up to a wavelength of 1700 nm. This upper boundary exceeds those of any report among erbium-doped NLP lasers operating primarily in the C-band [18, 20, 211, 212, 219].

6.3.2 Experimental setup of the dual-wavelength laser

The experimental setup schematized in Fig. 6.7 consists of a ring cavity similar to the ones used for mode-locking by NPR [165]. The 1007 m long HNLF has a chromatic dispersion coefficient

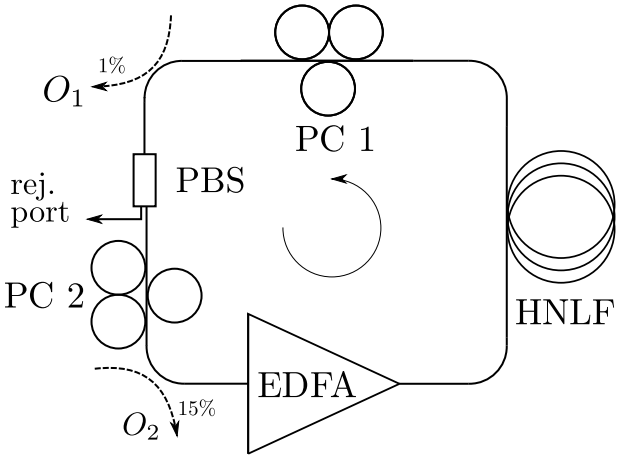

Figure 6.7 – *Ring cavity composed of a HNLF, an EDFA, two PCs, a polarization beam-splitter (PBS) and two output tap couplers $O_{1,2}$. EDFA: erbium-doped fiber amplifier, PC: polarization controller, PBS: polarization beam splitter.*

$D = -0.71\,\mathrm{ps\,nm^{-1}\,km^{-1}}$, a nonlinear waveguide coefficient $\gamma = 11.5\,\mathrm{W^{-1}\,km^{-1}}$ and a loss of 1.5 dB at a wavelength of 1550 nm. The EDFA, which contains an optical isolator, is pumped at 976 nm and has a length $\times$ chromatic dispersion product of $LD_{\mathrm{EDFA}} = 138\,\mathrm{ps\,nm^{-1}}$. The other components

of the cavity account for ∼20 m of silica single mode fiber, and therefore the average chromatic dispersion in the cavity is normal with a value of $LD_{\text{avg}} = -406\,\text{ps}\,\text{nm}^{-1}$. An optical spectrum analyzer and a photodiode are connected at the 1% and 15% output couplers $O_{1,2}$, respectively. The rejection port of the PBS is also used for monitoring purposes. It provides a linearly polarized laser output with a high output coupling ratio (OCR).

6.3.3 Results and discussion

Noiselike pulses are obtained by an adjustment of the two PCs. With an EDFA pump power of ∼100 mW, the sudden broadening of the initial continuous-wave regime indicates the presence of a burst of pulses also visible with a fast photodetector. A repetition rate of 194 kHz is observed at output O_2 for an average power of −5 dBm. Spectra are presented in Fig. 6.8, along with their time-domain behavior in the corresponding insets. In Fig. 6.8(a), the PCs are tuned to obtain a pulsed operation around 1550 nm. The spectral bandwidth of the RP signal is 10 nm. A weak signal generated from SRS, noted (i), is also observed. The RP pulses contain most of the power, and noiselike pulses are observed temporally and spectrally. With a further increase of the EDFA gain, both the RP signal and the Stokes signal are raised by a similar amount.

We believe that the red-most signal is sustained by a Raman gain supplied by the 1550 nm signal. Indeed, the wavelength separation Ω_1 is of 111 nm, which corresponds well to the 13.2 THz offset expected for a Stokes wave due to a SRS process. In trace (h), the PCs have been carefully adjusted to maximize the Stokes signal. The latter contains 1.5 times more energy than the RP signal and has a FWHM of 8.4 nm. A peak is also observed at a wavelength of 1464 nm. Its spectral separation of 95 nm with respect to the RP again has a consistent spectral offset for an anti-Stokes Raman peak. We note that the 50 dB difference between the Stokes and anti-Stokes lines is also expected because of a much less probable phase-matching of the anti-Stokes wave [38]. The presence of this peak confirms that the strong gain observed at the Stokes wavelength of the spectrum is due to a SRS process rather than a four-wave mixing, which, acting alone, would lead to a pair of new frequency components of similar amplitude. An exact measurement of the peak power of noiselike pulses is difficult to achieve due to their complex structure. However, the NLPs yields to a significant SRS process which exceeds the expected Raman threshold of $P_{\text{th}} = 16A_{\text{Eff}}/(g_R L_{\text{Eff}}) = 14.5\,\text{W}$, with $g_R = 6.5 \times 10^{-14}\,\text{m}\,\text{W}^{-1}$, $L_{\text{Eff}} = 850\,\text{m}$, and $A_{\text{Eff}} \sim 50\,\mu\text{m}^2$ for the HNLF [38]. This is a lower bound to the actual NLPs peak power. Figure 6.9 shows the typical

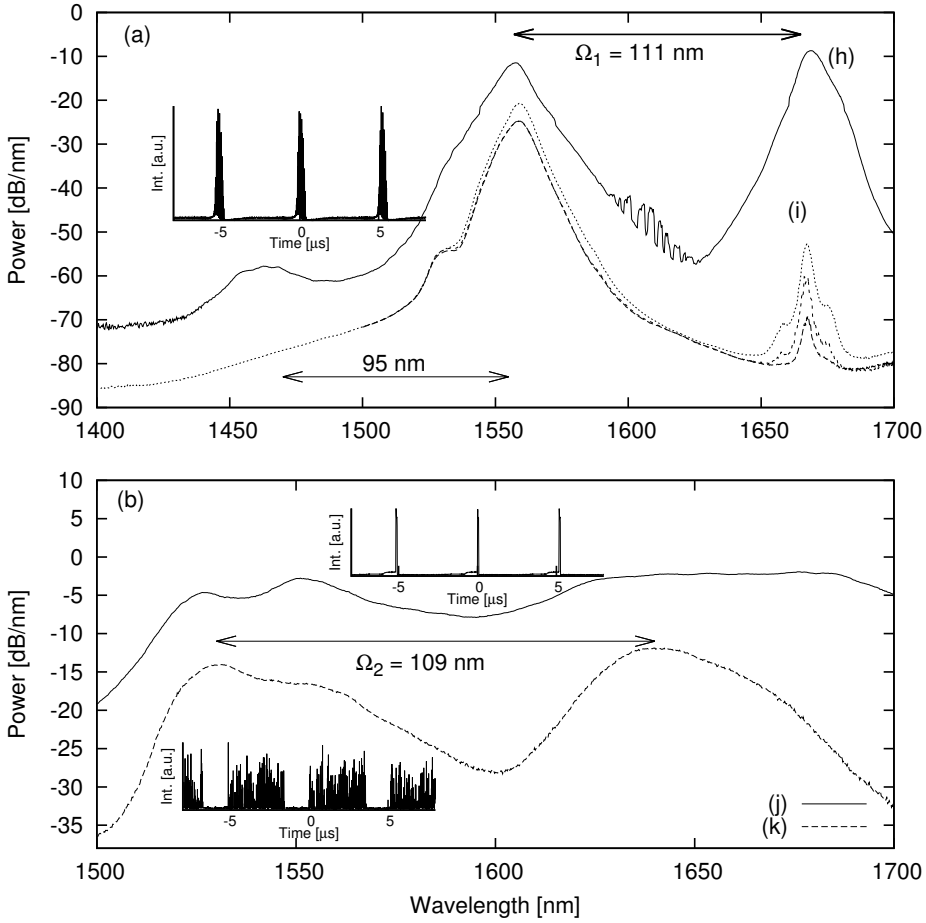

Figure 6.8 – *Dual-wavelength lasing at O_2: (a) at various EDFA pump powers. Inset: photodiode response of the RP pulses of trace (h). (b) Other PC configurations. The spectral offset between the pump and the Stokes pulses are denoted by $\Omega_{1,2}$. Insets: corresponding photodiode intensity response.*

FROG spectrogram of the RP NLPs of Fig. 6.8(a). The ratio between the autocorrelation peak and the shoulder of the pulse's autocorrelation is close to 2, which indicates the absence of structure in the pulse, as discussed for example in Refs. [18, 192].

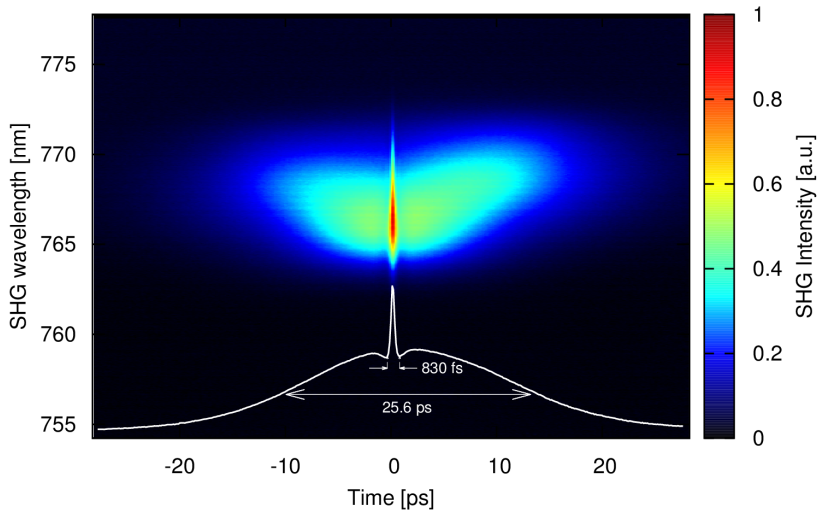

Figure 6.9 – *FROG spectrogram of a noiselike pulse and its autocorrelation width of 25.6 ps.*

6.3.4 Single-shot spectral measurements

Experimental single-shot measurements provide additional evidence for the presence of noise-like pulses at the RP and Stokes wavelengths. Following the technique described by Kelkar et al. [76] and applied to noiselike pulses for the first time by Runge et al. [19], we measure the spectrum of noiselike pulses in the time domain. In Fig. 6.10, a set of measurements are presented, and depict the large spectral variations that occur during the pulse propagation.

The temporal pulse profile of noiselike pulses exhibits constant fluctuations. The gain induced at the Stokes wavelength therefore depends on the fluctuations in the RP pulses.

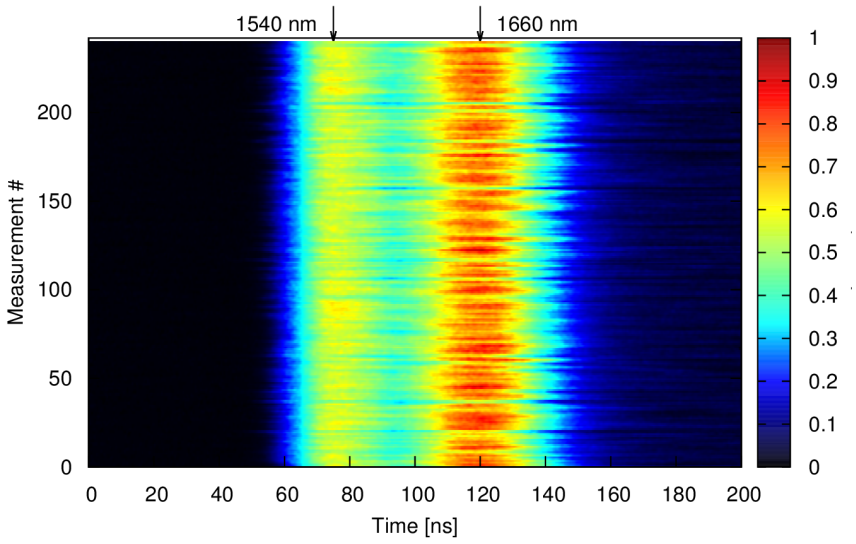

Figure 6.10 – *Single-shot measurements of the spectrum of the dual-wavelength source.*

6.3.5 Dynamics of the laser

In Fig. 6.8(b), other positionings of the PCs lead to two different broadband NLP regimes. The spectrum is shifted towards shorter wavelengths with respect to the spectrum shown in (a). As well, a spectral offset $\Omega_1 \simeq \Omega_2$ is observed. In (k), the bandwidth for the RP and the Stokes signals are of 34 nm and 32 nm respectively, reflecting that NLPs are also spawned at the Stokes wavelength. In this configuration, the average power of the Stokes pulses is 1.65 times the average power of the RP pulses. With a careful tuning of the PCs, the bandwidth of the RP and Stokes pulses is altered [217]. Stokes pulses with a bandwidth of 84 nm FWHM could be observed as depicted in trace (j), extending from 1616 nm to 1700 nm, while the RP pulses were of 46 nm FWHM. From this point, we focus on what is found to be the most stable regime, denoted (k) in Fig. 6.8(b), often the first one observed when pulsing starts. In Fig. 6.11(a), the output power at O_2 and the rejection port are presented as functions of the EDFA pump power. The rejection port presents an OCR of 50% at any EDFA pump power. In (b), an increase of the EDFA pump power leads to a spectral broadening of the RP pulses up to a pump power of 161 mW. After that point, we note that the Stokes pulses take advantage of the additional RP power, and undergo a spectral broadening as well. In this process, the autocorrelation width of the RP pulses does not significantly change. As opposed to the behavior observed in [20] where the existing NLPs consumed the excess of EDFA

pump power and temporally broaden with an increasing EDFA pump power, this rather suggests a transfer of the RP pulse power to new trains of NLPs and to the Stokes pulses via SRS.

The energy contained in each of the RP and Stokes pulses is depicted in Fig. 6.11(c) as the EDFA pump power is decreased. Due to the quasi-instantaneous Raman response [38], the Stokes pulses are sustained only if the RP pulses keep a sufficient peak power. In accordance with time-domain observations, the peak power of the RP pulses diminishes, which quickly lowers the Raman gain and affects both the energy and the spectral peak power of the Stokes pulses. In the time domain, two main regimes are observed at the repetition rate of the cavity, 194 kHz. First, "square-shaped" pulses, also seen in [20], are broadening with increasing EDFA pump power. A photodiode covering the range 1.2 µm to 2.6 µm indicates as expected that the Stokes pulses overlap the RP pulses. This was confirmed by alternatively filtering each in the spectral domain. Between the RP and Stokes pulses, the group velocity mismatch delay in the HNLF is of 4 ns. This delay is compensated by an asymmetrical gain and loss profile experienced by the slower Stokes pulses. Also, a chaotic regime presented in Fig. 6.12 indicates a $\sim$3.5 µs long burst which contains a set of impulses separated by $\sim$33 ns. A frequency analyzer indeed shows peaks at the fundamental frequency and at 30 MHz, regardless of the EDFA pump power. For this regime, decreasing the EDFA pump power decreases the burst duration, peak and average power of the pulses in the cavity. However, at least one powerful RP pulse is always present, providing a sufficient Raman gain to sustain Stokes pulses. As the power is reduced, it is observed that two wavelengths oscillate at the RP with an offset of 8 nm, and pulses slide along each other as observed previously in [219]. This behaviour is attributed to the significant birefringence of $\Delta n = 3.5 \times 10^{-7}$ in the HNLF, along with an additional polarization group delay induced by the PBS.

6.3.6 Summary

A dual-wavelength pulsed all-fiber laser based on NPR in NLP regime was presented. In presence of a HNLF with normal dispersion, pulses are observed at the RP frequency in the C-band, and at the first Stokes wavelength in the U-band. Although the fundamental cavity repetition rate is in the kHz range, an increase of the EDFA pump power extends the burst duration over the whole cavity period with little changes of the spectrum. A broadband continuum of 84 nm FWHM was observed, containing most of the spectral power and spanning from 1616 nm to 1700 nm, filling the gap between the erbium and thulium emission regions, and hardly accessible by other means.

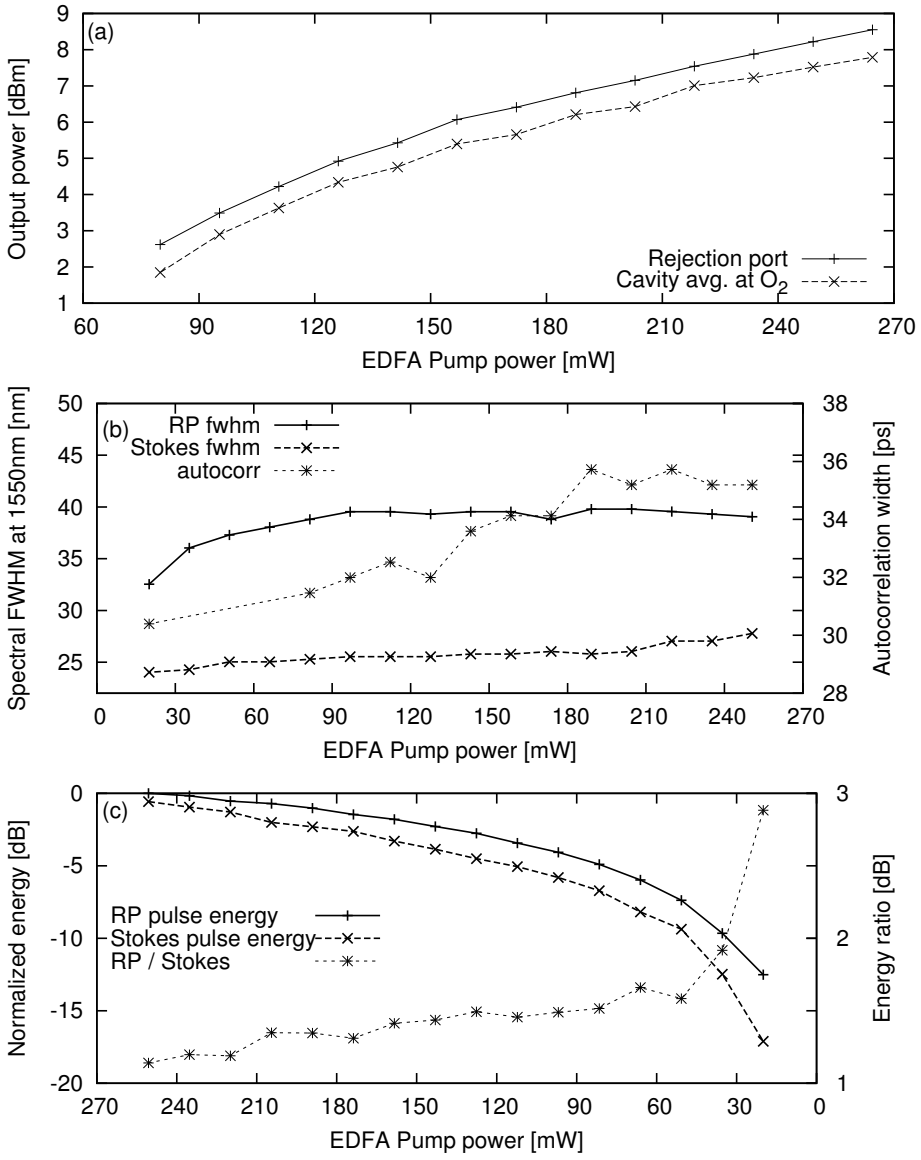

Figure 6.11 – *Effect of a variation of the EDFA pump power. (a) Power at the rejection port and in the cavity, observed from output coupler O_2. (b) Spectral width at the RP and Stokes pulses, and autocorrelation width for the RP pulses. (c) Pulses' spectral energy as the EDFA pump power is decreased.*

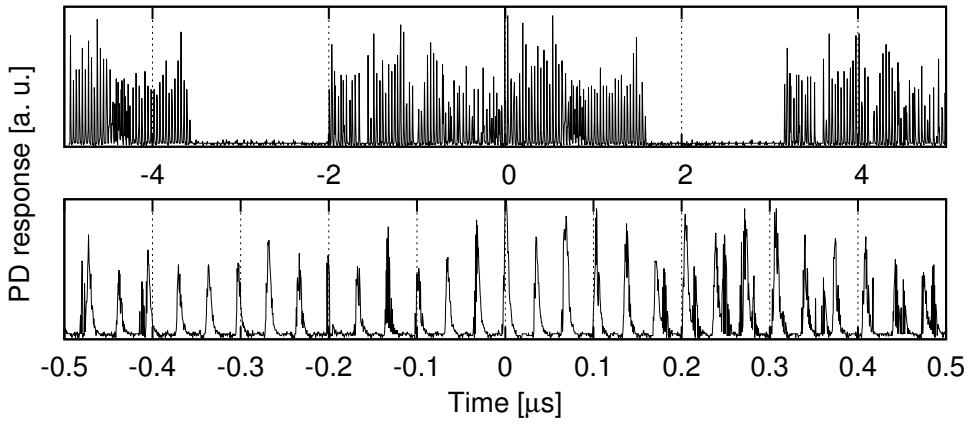

Figure 6.12 – *Time-domain behaviour at two different time scales. PD: photodiode.*

A large OCR of ∼50% was observed at the linearly-polarized output of the cavity.

6.4 Conclusion

In this chapter, we have presented two architectures leading to the generation of broadband pulses. In Section 6.2, the addition of a specialty fiber in a ring cavity was shown to be beneficial in reducing the average cavity chromatic dispersion. The large normal dispersion of chalcogenide fiber compensates the anomalous dispersion of other cavity components with only a short fiber length, thereby allowing the design of stretched-pulse lasers of high repetition rate, and hence femtosecond pulse duration. Due to its high nonlinearity, the addition of chalcogenide fiber theoretically enables the generation of pulses at low-peak power, and can be used as gain medium via SRS. Demonstrating this fact is currently hardly achievable due to the large losses at the chalcogenide-silica interfaces. However, this first demonstration of operation is a step towards the realization of such compact and efficient sources. Section 6.2.4 provides a first experimental report of NLP generation in this new cavity. The reinforced action of SRS, due to a Raman gain coefficient g_R $100\times$ higher than that of silica fibers [225], broadens the pulses over 51 nm FWHM, and provides a flat extension of the continuum towards the long wavelengths, up to 1650 nm. In Section 6.3, dual-wavelength noiselike pulses are reported in a 2 km long cavity with normal average dispersion. SRS transfers energy from the 1550 nm pump pulses towards a wavelength

of 1670 nm. An adequate tuning of the PCs leads to an efficient energy transfer, such that the Stokes pulses are twice as powerful as the pump pulses. The noiselike Stokes pulses can spread over 84 nm, beyond the wavelength of 1700 nm, which enables spectroscopy applications in a wavelength range with is in the gap between the erbium and thulium emission regions. Pumped in the C-band, this laser efficiently transfers power towards wavelengths longer wavelengths than that of any previous report [20, 215].

Conclusion

Throughout three different architectures, new broadband self-pulsating sources based on nonlinear effects have been reported. In a first approach, regenerative sources based on cascaded SPM-OF regenerators were studied and optimized for the generation of short and energetic pulses. Based on numerical simulations, a new cavity was presented. Pulses of 440 fs FWHM and with an energy of 3.5 pJ are observed in a setup whose efficiency is $30\times$ larger than previously reported.

Second, a new self-pulsating source was introduced. As for the SPM-OF sources, this new architecture features wavelength toggling. It is shown that, on the average, a flat continuum spreading over more than 400 nm is created as a result of nonlinear propagation in a HNLF with anomalous dispersion placed inside the laser cavity. In the time domain, an ultralong pulse train spreading over up to 400 ns is observed at a repetition rate of 100 kHz. Numerical simulations describe the source behavior, and shot-to-shot spectral measurement confirm the mechanism of SC generation.

Finally, noiselike pulses were generated in a cavity with large normal dispersion. Via SRS, dual-wavelength operation enables the generation of broadband pulses of 84 nm in the U-band, as well as an efficient power transfer from the pump wavelength to the first Stokes line.

These cavities were designed with standard optical components optimized for the C-band, as well as two HNLFs.

Open questions remain after these investigations. Sources based on SPM-OF regenerators have been implemented so that a single nonlinear medium could be used, paired with unidirectional EDFAs. Their study in a linear cavity, composed of Bragg gratings centered at two different wavelengths, could lead to a simplified setup. Such an architecture would fit on a chip, and easily enable the generation of broadband pulses for sensing applications. More generally, sources based

on cascaded regeneration have been designed in long cavities, and could benefit of other kinds of nonlinear media, including specialty fibers (chalcogenides, tellurite, etc.), therefore increasing their repetition rate and compactness.

The efficiency of SPM-OF sources was increased, but further research could lead to higher pulse energies. For example, similariton propagation, as suggested by Pitois et al., could replace one SPM-OF stage, and potentially decrease the number of rejected spectral components, because the spectrum of similaritons does not exhibit wide pedestals.

SPM-SSFS sources would also benefit of more investigation. In particular, their ability to generate and sustain SC-free pulses must be assessed. In this configuration, the energy transfer towards long wavelength is efficient and raises questions related to the optimization of energy towards the short wavelengths.

The stability of noiselike pulse sources could be improved with the use of an NALM, and the use of PM fibers, to decrease the polarization sensitivity of the setup. The generation of noiselike pulses at higher Stokes orders could also be explored, provided that an adequate nonlinear medium featuring similar group-velocity at the pump and Stokes wavelength is used.

Appendix A

Appendix

A.1 Numerical simulations

This section provides minimal code to simulate nonlinear pulse compression. In listings A.1 and A.2, an input pulse is propagated in a nonlinear fiber in normal dispersion, inducing spectral broadening by SPM. Then, the propagation in a purely dispersive fiber recompresses the pulses down to the a new subpicosecond pulse.

Listing A.1 – *Nonlinear pulse compression*

```
from sparam import Gparams
from bpf import BPF
from fiber import Fiber
from pulsed_laser import PulsedLaser

params = Gparams() # Defaults to 1550 nm
params.set_DTime(5e-15) # Time increment
params.set_NSamp(2**14) # 2**14 samples
pulsed_input = PulsedLaser(params,
                  profile='sech')
pulsed_input.set_fwhm(25e-12)
pulsed_input.set_P0(0.125) # 1 W peak power
hnlf = Fiber(params, L=15000, Nz=1000,
         name="Pulse_compression_1")
hnlf.set_gamma(0.10)
```

```
hnlf.set_beta2(1.e-27)
hnlf.set_method('rk')
hnlf.set_gpu('GPU')
hnlf2 = Fiber(params, L=1.08*15000, Nz=1,
      name="Pulse_compression_2")
hnlf2.set_beta2(-1.e-27)
pulsed_input.run()
hnlf.set_input('fiber_in',
  pulsed_input.get_output('pulsed_laser_out'))
hnlf.run()
hnlf.show()
hnlf2.set_input('fiber_in',
  hnlf.get_output('fiber_out'))
hnlf2.run()
hnlf2.show()
```

More conveniently, a text file containing all device parameters for the experimental setup can be used instead. This allows for the automatic generation of complex optical setups from a generator, which could for instance provide a graphical interface describing experiments by a series of connected devices. The code of Listing A.1 is therefore rewritten as:

Listing A.2 – *Nonlinear pulse compression, text based*

```
[params]
dtime = 5e-15
nsamp = 2**14
lambda_0 = 1550e-9

[hnlf]
length = 15e3
Nz = 1e3
beta_2 = 1e-27
gamma = 0.10
use_method = rk
use_gpu = GPU

[hnlf2]
length = 1.08*15000
```

```
Nz = 1
beta_2 = -1e-27
fiber_in = hnlf.fiber_out

[input_pulse]
type = PulsedLaser
P0 = 0.125
fwhm = 25e-12
shape = sech
seed = hnlf.fiber_in
```

Bibliography

[1] A. L. Schawlow and C. H. Townes. “Infrared and Optical Masers”. *Phys. Rev.* 112 (6 Dec. 1958), 1940–1949.

[2] A. H. Zewail et al. “Femtochemistry. Past, present, and future”. *Pure Appl. Chem.* 72.12 (2000), 2219–2231.

[3] W Denk, J. Strickler, and W. Webb. “Two-photon laser scanning fluorescence microscopy”. *Science* 248.4951 (1990), 73–76.

[4] T. Udem, R Holzwarth, and T. W. Hänsch. “Optical frequency metrology”. *Nature* 416.6877 (2002), 233–237.

[5] F.-Y. Lin and J.-M. Liu. “Chaotic lidar”. *IEEE J. Sel. Topics Quantum Electron.* 10.5 (2004), 991–997.

[6] R. R. Gattass and E. Mazur. “Femtosecond laser micromachining in transparent materials”. *Nat. Photonics* 2.4 (2008), 219–225.

[7] W. Knox. “Ultrafast technology in telecommunications”. *IEEE J. Sel. Topics Quantum Electron.* 6.6 (2000), 1273–1278.

[8] T. Ditmire, J Zweiback, V. Yanovsky, T. Cowan, G Hays, and K. Wharton. “Nuclear fusion from explosions of femtosecond laser-heated deuterium clusters”. *Nature* 398.6727 (1999), 489–492.

[9] D. E. Spence, P. N. Kean, and W. Sibbett. “60-fsec pulse generation from a self-mode-locked Ti:sapphire laser”. *Opt. Lett.* 16.1 (Jan. 1991), 42–44.

[10] A. Killi, J. Dörring, U. Morgner, M. Lederer, J. Frei, and D. Kopf. “High speed electro-optical cavity dumping of mode-locked laser oscillators”. *Opt. Express* 13.6 (Mar. 2005), 1916–1922.

[11] C. R. E. Baer, C. Kränkel, C. J. Saraceno, O. H. Heckl, M. Golling, R. Peters, K. Petermann, T. Südmeyer, G. Huber, and U. Keller. "Femtosecond thin-disk laser with 141 W of average power". *Opt. Lett.* 35.13 (July 2010), 2302–2304.

[12] E. U. Rafailov, M. A. Cataluna, W. Sibbett, N. D. Il'inskaya, Y. M. Zadiranov, A. E. Zhukov, V. M. Ustinov, D. A. Livshits, A. R. Kovsh, and N. N. Ledentsov. "High-power picosecond and femtosecond pulse generation from a two-section mode-locked quantum-dot laser". *Appl. Phys. Lett.* 87.8, 081107 (2005), –.

[13] K. Wilcox, A. Quarterman, H. Beere, D. Ritchie, and A. Tropper. "High Peak Power Femtosecond Pulse Passively Mode-Locked Vertical-External-Cavity Surface-Emitting Laser". *IEEE Photon. Technol. Lett.* 22.14 (2010), 1021–1023.

[14] S. Lefrançois, K. Kieu, Y. Deng, J. D. Kafka, and F. W. Wise. "Scaling of dissipative soliton fiber lasers to megawatt peak powers by use of large-area photonic crystal fiber". *Opt. Lett.* 35.10 (May 2010), 1569–1571.

[15] W. Sibbett, A. A. Lagatsky, and C. T. A. Brown. "The development and application of femtosecond laser systems". *Opt. Express* 20.7 (Mar. 2012), 6989–7001.

[16] K. Sun, M. Rochette, and L. R. Chen. "Output characterization of a self-pulsating and aperiodic optical fiber source based on cascaded regeneration". *Opt. Express* 17.12 (June 2009), 10419–10432.

[17] M. Rochette, L. R. Chen, K. Sun, and J. Hernandez-Cordero. "Multiwavelength and Tunable Self-Pulsating Fiber Cavity Based on Regenerative SPM Spectral Broadening and Filtering". *IEEE Photon. Technol. Lett.* 20.17 (Sept. 2008), 1497–1499.

[18] M. Horowitz, Y. Barad, and Y. Silberberg. "Noiselike pulses with a broadband spectrum generated from an erbium-doped fiber laser". *Opt. Lett.* 22.11 (June 1997), 799–801.

[19] A. F. J. Runge, C. Aguergaray, N. G. R. Broderick, and M. Erkintalo. "Coherence and shot-to-shot spectral fluctuations in noise-like ultrafast fiber lasers". *Opt. Lett.* 38.21 (Nov. 2013), 4327–4330.

[20] L. A. Vazquez-Zuniga and Y. Jeong. "Super-Broadband Noise-Like Pulse Erbium-Doped Fiber Ring Laser With a Highly Nonlinear Fiber for Raman Gain Enhancement". *IEEE Photon. Technol. Lett.* 24.17 (Sept. 2012), 1549–1551.

[21] T. North and M. Rochette. “Fabrication and characterization of a pulsed fiber ring laser based on As2S3”. *Opt. Lett.* 37.4 (Feb. 2012), 716–718.

[22] T. North and M. Rochette. “Broadband self-pulsating fiber laser based on soliton self-frequency shift and regenerative self-phase modulation”. *Opt. Lett.* 37.14 (July 2012), 2799–2801.

[23] T. North and M. Rochette. “Raman-induced noiselike pulses in a highly nonlinear and dispersive all-fiber ring laser”. *Opt. Lett.* 38.6 (Mar. 2013), 890–892.

[24] T. North and M. Rochette. “Analysis of Self-Pulsating Sources Based on Regenerative SPM: Ignition, Pulse Characteristics and Stability”. *IEEE/OSA J. Lightw. Technol.* 31.23 (2013), 3700–3706.

[25] T. North and M. Rochette. “Regenerative self-pulsating sources of large bandwidths”. *Opt. Lett.* 39.1 (Jan. 2014), 174–177.

[26] T. North, A. Al-kadry, and M. Rochette. “Analysis of self-pulsating sources based on cascaded regeneration and soliton self-frequency shifting”. *IEEE J. Sel. Topics Quantum Electron.* PP.99 (2014), 1–1.

[27] M. Gorjan, T. North, and M. Rochette. “Model of the amplified spontaneous emission generation in thulium-doped silica fibers”. *J. Opt. Soc. Am. B* 29.10 (Oct. 2012), 2886–2890.

[28] A. Velazquez-Benitez, R. Ahmad, T. North, M. Gorjan, J. Hernandez-Cordero, and M. Rochette. “All-Optical Broadband Variable Optical Attenuator Based on an As_2Se_3 Microwire”. *IEEE Photon. Technol. Lett.* 25.7 (Apr. 2013), 697–700.

[29] T. North and M. Rochette. “Subpicosecond As2S3 fiber ring laser”. In: *Photonics Conference (PHO), 2011 IEEE*. IEEE. 2011, 429–430.

[30] T. North and M. Rochette. “Source Laser Auto-Pulsante via Auto-Décalage Fréquentiel de Solitons et l’Auto-Modulation de Phase”. In: *Journées Nationales d’Optique Guidée (JNOG), 2012*. July 2012.

[31] T. North and M. Rochette. “Dual-wavelength noiselike pulse generation via polarization rotation and stimulated Raman scattering in an erbium-doped fiber ring laser”. In: *Proc. SPIE Photonics North 2013*. Vol. 8915. 2013, 891511–891511–6.

[32] K. Tamura, E. Ippen, H. Haus, and L. Nelson. “77-fs pulse generation from a stretched-pulse mode-locked all-fiber ring laser”. *Opt. Lett.* 18.13 (1993), 1080–1082.

[33] K. Kieu, J. Jones, and N. Peyghambarian. "Generation of sub-20fs pulses from an all-fiber carbon nanotube mode-locked laser system". In: *Conference on Lasers and Electro-Optics*. Optical Society of America. 2010.

[34] G. Keiser. *Optical fiber communications*. McGraw-Hill New York, 1983.

[35] D. Gloge. "Weakly Guiding Fibers". *Appl. Opt.* 10.10 (Oct. 1971), 2252–2258.

[36] A. Snyder and J. Love. *Optical waveguide theory*. Vol. 190. Springer, 1983.

[37] A. Weiner. *Ultrafast optics*. Vol. 72. Wiley, 2011.

[38] G. Agrawal. *Nonlinear fiber optics*. Optics and Photonics. Academic Press, 2007.

[39] E. F. Schubert, T. Gessmann, and J. K. Kim. *Light emitting diodes*. Wiley Online Library, 2005.

[40] W Sellmeier. "Zur Erklärung der abnormen Farbenfolge im Spectrum einiger Substanzen". *Ann. Phys. und Chemie* 219.6 (1871), 272–282.

[41] B. E. Saleh, M. C. Teich, and B. E. Saleh. *Fundamentals of photonics*. Vol. 22. Wiley New York, 1991.

[42] M. Bellini and T. W. Hänsch. "Phase-locked white-light continuum pulses: toward a universal optical frequency-comb synthesizer". *Opt. Lett.* 25.14 (July 2000), 1049–1051.

[43] J. Nicholson and M. Yan. "Cross-coherence measurements of supercontinua generated in highly-nonlinear, dispersion shifted fiber at 1550 nm". *Opt. Express* 12.4 (Feb. 2004), 679–688.

[44] P. A. Franken, A. E. Hill, C. W. Peters, and G. Weinreich. "Generation of Optical Harmonics". *Phys. Rev. Lett.* 7 (4 Aug. 1961), 118–119.

[45] F. Shimizu. "Frequency Broadening in Liquids by a Short Light Pulse". *Phys. Rev. Lett.* 19 (19 Nov. 1967), 1097–1100.

[46] R. H. Stolen and C. Lin. "Self-phase-modulation in silica optical fibers". *Phys. Rev. A* 17 (4 Apr. 1978), 1448–1453.

[47] G. Agrawal. *Lightwave Technology: Telecommunication Systems*. Wiley, 2005.

[48] I. N. Sisakyan and A. B. Shvartsburg. "Nonlinear dynamics of picosecond pulses in fiber-optic waveguides (review)". *Sov. J. Quantum Electron.* 14.9 (1984), p. 1146.

[49] M. N. Islam, L. F. Mollenauer, R. H. Stolen, J. R. Simpson, and H. T. Shang. "Cross-phase modulation in optical fibers". *Opt. Lett.* 12.8 (Aug. 1987), 625–627.

[50] R. L. Carman, R. Y. Chiao, and P. L. Kelley. "Observation of Degenerate Stimulated Four-Photon Interaction and Four-Wave Parametric Amplification". *Phys. Rev. Lett.* 17 (26 Dec. 1966), 1281–1283.

[51] R. H. Stolen. "Phase-matched-stimulated four-photon mixing in silica-fiber waveguides". *IEEE J. Quantum Electron.* 11.3 (1975), 100–103.

[52] A. Demircan and U. Bandelow. "Analysis of the interplay between soliton fission and modulation instability in supercontinuum generation". English. *Appl. Phys. B* 86 (1 2007), 31–39.

[53] J. M. Dudley, G. Genty, F. Dias, B. Kibler, and N. Akhmediev. "Modulation instability, Akhmediev Breathers and continuous wave supercontinuum generation". *Opt. Express* 17.24 (Nov. 2009), 21497–21508.

[54] A. Smekal. "Zur Quantentheorie der Dispersion". German. *Naturwissenschaften* 11.43 (1923), 873–875.

[55] C. Raman and K. Krishnan. "A new type of secondary radiation". *Nature* 121.3048 (1928), 501–502.

[56] N. Bloembergen. "The Stimulated Raman Effect". *Am. J. Phys* 35.11 (1967), 989–1023.

[57] A. Hasegawa and F. Tappert. "Transmission of stationary nonlinear optical pulses in dispersive dielectric fibers. I. Anomalous dispersion". *Appl. Phys. Lett.* 23.3 (1973), 142–144.

[58] J. Dudley, A. Peacock, and G. Millot. "The cancellation of nonlinear and dispersive phase components on the fundamental optical fiber soliton: a pedagogical note". *Opt. Commun.* 193.1–6 (2001), 253–259.

[59] A. M. Weiner, J. P. Heritage, R. J. Hawkins, R. N. Thurston, E. M. Kirschner, D. E. Leaird, and W. J. Tomlinson. "Experimental Observation of the Fundamental Dark Soliton in Optical Fibers". *Phys. Rev. Lett.* 61 (21 Nov. 1988), 2445–2448.

[60] N. Akhmediev, V. Eleonskii, and N. Kulagin. "Exact first-order solutions of the nonlinear Schrödinger equation". English. *Theor. Math. Phys.* 72.2 (1987), 809–818.

[61] N. Akhmediev, J. Soto-Crespo, and A. Ankiewicz. "Extreme waves that appear from nowhere: On the nature of rogue waves". *Phys. Lett. A* 373.25 (2009), 2137–2145.

[62] K. Hammani, B. Wetzel, B. Kibler, J. Fatome, C. Finot, G. Millot, N. Akhmediev, and J. M. Dudley. "Spectral dynamics of modulation instability described using Akhmediev breather theory". *Opt. Lett.* 36.11 (June 2011), 2140–2142.

[63] Kibler B., Fatome J., Finot C., Millot G., Genty G., Wetzel B., Akhmediev N., Dias F., and Dudley J. M. "Observation of Kuznetsov-Ma soliton dynamics in optical fibre". *Sci. Rep.* 2 (June 2012).

[64] Kibler B., Fatome J., Finot C., Millot G., Dias F., Genty G., Akhmediev N., and Dudley J. M. "The Peregrine soliton in nonlinear fibre optics". *Nat Phys* 6.10 (Oct. 2010), 790–795.

[65] J. Fatome, B. Kibler, and C. Finot. "High-quality optical pulse train generator based on solitons on finite background". *Opt. Lett.* 38.10 (May 2013), 1663–1665.

[66] S. K. Turitsyn, B. G. Bale, and M. P. Fedoruk. "Dispersion-managed solitons in fibre systems and lasers". *Phys. Rep.* 521.4 (2012), 135–203.

[67] J. Gordon. "Theory of the soliton self-frequency shift". *Opt. Lett.* 11.10 (1986), 662–664.

[68] H. W. Mocker and R. J. Collins. "Mode competition and self-locking effects in a Q-Switched ruby laser". *Appl. Phys. Lett.* 7.10 (1965), 270–273.

[69] L. Barry, P. Bollond, J. M Dudley, J. Harvey, and R. Leonhardt. "Autocorrelation of ultrashort pulses at 1.5μm based on nonlinear response of silicon photodiodes". *Electron. Lett.* 32.20 (1996), 1922–1923.

[70] J. K. Ranka, A. L. Gaeta, A. Baltuska, M. S. Pshenichnikov, and D. A. Wiersma. "Autocorrelation measurement of 6-fs pulses based on the two-photon-induced photocurrent in a GaAsP photodiode". *Opt. Lett.* 22.17 (Sept. 1997), 1344–1346.

[71] J.-C. M. Diels, J. J. Fontaine, I. C. McMichael, and F. Simoni. "Control and measurement of ultrashort pulse shapes (in amplitude and phase) with femtosecond accuracy". *Appl. Opt.* 24.9 (May 1985), 1270–1282.

[72] P. O'Shea, M. Kimmel, X. Gu, and R. Trebino. "Highly simplified device for ultrashort-pulse measurement". *Opt. Lett.* 26.12 (June 2001), 932–934.

[73] R. Trebino and D. J. Kane. “Using phase retrieval to measure the intensity and phase of ultrashort pulses: frequency-resolved optical gating”. *J. Opt. Soc. Am. A* 5 (May 1993), 1101–1111.

[74] D. Kane. “Real-time measurement of ultrashort laser pulses using principal component generalized projections”. *IEEE J. Sel. Topics Quantum Electron.* 4.2 (Mar. 1998), 278–284.

[75] J. W. Nicholson, F. G. Omenetto, D. J. Funk, and A. J. Taylor. “Evolving FROGS: phase retrieval from frequency-resolved optical gating measurements by use of genetic algorithms”. *Opt. Lett.* 24.7 (Apr. 1999), 490–492.

[76] P. Kelkar, F. Coppinger, A. S. Bhushan, and B. Jalali. “Time-domain optical sensing”. *Electron. Lett.* 35.19 (1999), 1661–1662.

[77] B. Wetzel, A. Stefani, L. Larger, P. A. Lacourt, J. M. Merolla, T. Sylvestre, A. Kudlinski, A. Mussot, G. Genty, F. Dias, et al. “Real-time full bandwidth measurement of spectral noise in supercontinuum generation”. *Sci. Rep.* 2 (2012).

[78] L. E. Hargrove, R. L. Fork, and M. A. Pollack. “Locking of HeNe laser modes induced by synchronous intracavity modulation”. *Appl. Phys. Lett.* 5.1 (1964), 4–5.

[79] I. Alcock, A. Ferguson, D. Hanna, and A. Tropper. “Mode-locking of a neodymium-doped monomode fibre laser”. *Electron. Lett.* 22.5 (1986), 268–269.

[80] M. Becker, D. Kuizenga, and A. Siegman. “Harmonic mode locking of the Nd:YAG laser”. *IEEE J. Quantum Electron.* 8.8 (Aug. 1972), 687–693.

[81] P. Smith. “Mode-locking of lasers”. *Proc. IEEE* 58.9 (1970), 1342–1357.

[82] H. Haus. “Mode-locking of lasers”. *IEEE J. Sel. Topics Quantum Electron.* 6.6 (2000), 1173–1185.

[83] E. P. Ippen, H. A. Haus, and L. Y. Liu. “Additive pulse mode locking”. *J. Opt. Soc. Am. B* 6.9 (Sept. 1989), 1736–1745.

[84] N. J. Doran and D. Wood. “Nonlinear-optical loop mirror”. *Opt. Lett.* 13.1 (Jan. 1988), 56–58.

[85] M. E. Fermann, F. Haberl, M. Hofer, and H. Hochreiter. “Nonlinear amplifying loop mirror”. *Opt. Lett.* 15.13 (July 1990), 752–754.

[86] C. Aguergaray, N. Broderick, M. Erkintalo, J. Chen, and V. Kruglov. "Mode-locked femtosecond all-normal all-PM Yb-doped fiber laser using a nonlinear amplifying loop mirror". *Opt. Express* 20.10 (2012), 10545–10551.

[87] L Dahlström. "Passive mode-locking and Q-switching of high power lasers by means of the optical Kerr effect". *Opt. Commun.* 5.3 (1972), 157–162.

[88] R. Stolen, J. Botineau, and A. Ashkin. "Intensity discrimination of optical pulses with birefringent fibers". *Opt. Lett.* 7.10 (1982), 512–514.

[89] M. Hofer, M. E. Fermann, F. Haberl, M. H. Ober, and A. J. Schmidt. "Mode locking with cross-phase and self-phase modulation". *Opt. Lett.* 16.7 (Apr. 1991), 502–504.

[90] C. Mou, H. Wang, B. G. Bale, K. Zhou, L. Zhang, and I. Bennion. "All-fiber passively mode-locked femtosecond laser using a 45°-tilted fiber grating polarization element". *Opt. Express* 18.18 (Aug. 2010), 18906–18911.

[91] G. A. Askaryan. "Effects of the gradient of a strong electromagnetic beam on electrons and atoms". *Sov. Phys. JETP* 15.0 (1962), 1088–1090.

[92] R. Y. Chiao, E. Garmire, and C. H. Townes. "Self-Trapping of Optical Beams". *Phys. Rev. Lett.* 13 (15 Oct. 1964), 479–482.

[93] P. L. Kelley. "Self-Focusing of Optical Beams". *Phys. Rev. Lett.* 15 (26 Dec. 1965), 1005–1008.

[94] S. Akhmanov, A. Sukhorukov, and R. Khokhlov. "Self-focusing and self-trapping of intense light beams in a nonlinear medium". *Sov. Phys. JETP* 23.1966 (1966), 1025–1033.

[95] J. Marburger. "Self-focusing: Theory". *Prog. Quantum Electron.* 4, Part 1.0 (1975), 35–110.

[96] Y. Shen. "Self-focusing: Experimental". *Prog. Quantum Electron.* 4, Part 1.0 (1975), 1–34.

[97] M. Piché, N. McCarthy, and F. Salin. In: *Digest of Annual Meeting of the Optical Society of America (Optical Society of America, Washington, D.C., 1990)*. Vol. MB8. OSA. 1990.

[98] T. Brabec, C. Spielmann, P. F. Curley, and F. Krausz. "Kerr lens mode locking". *Opt. Lett.* 17.18 (Sept. 1992), 1292–1294.

[99] M. Piché and F. Salin. "Self-mode locking of solid-state lasers without apertures". *Opt. Lett.* 18.13 (July 1993), 1041–1043.

[100] I. P. Christov, V. D. Stoev, M. M. Murnane, and H. C. Kapteyn. "Sub-10-fs operation of Kerr-lens mode-locked lasers". *Opt. Lett.* 21.18 (Sept. 1996), 1493–1495.

[101] C. Hauri, W. Kornelis, F. Helbing, A. Heinrich, A. Couairon, A. Mysyrowicz, J. Biegert, and U. Keller. "Generation of intense, carrier-envelope phase-locked few-cycle laser pulses through filamentation". English. *Appl. Phys. B* 79.6 (2004), 673–677.

[102] D. E. Laban, W. C. Wallace, R. D. Glover, R. T. Sang, and D. Kielpinski. "Self-focusing in air with phase-stabilized few-cycle light pulses". *Opt. Lett.* 35.10 (May 2010), 1653–1655.

[103] R. L. Fork, B. I. Greene, and C. V. Shank. "Generation of optical pulses shorter than 0.1 psec by colliding pulse mode locking". *Appl. Phys. Lett.* 38.9 (1981), 671–672.

[104] C.-C. Chen, Y.-W. Kiang, and C. Yang. "Colliding-pulse mode-locked semiconductor laser with a multimode-interference waveguide amplifier". *Opt. Commun.* 177.1–6 (2000), 363–368.

[105] G. Tandoi, J. Javaloyes, E. Avrutin, C. Ironside, and J. Marsh. "Subpicosecond Colliding Pulse Mode Locking at 126 GHz in Monolithic GaAs/AlGaAs Quantum Well Lasers: Experiments and Theory". *IEEE J. Sel. Topics Quantum Electron.* 19.4 (2013), 1100608–1100608.

[106] V. Lugovoi and A. Prokhorov. "Possibility of generating ultrashort light pulses in lasers with small luminscence line width of the medium". *Sov. Phys. JETP* 15 (1972), 49–51.

[107] V. Lugovoi. "Theory of mode locking at coherent Brillouin interaction". *IEEE J. Quantum Electron.* 19.4 (1983), 764–769.

[108] B. S. Kawasaki, D. C. Johnson, Y. Fujii, and K. O. Hill. "Bandwidth-limited operation of a mode-locked Brillouin parametric oscillator". *Appl. Phys. Lett.* 32.7 (1978), 429–431.

[109] P. Del'Haye, A Schliesser, O Arcizet, T Wilken, R Holzwarth, and T. Kippenberg. "Optical frequency comb generation from a monolithic microresonator". *Nature* 450.7173 (2007), 1214–1217.

[110] T. J. Kippenberg, R. Holzwarth, and S. A. Diddams. "Microresonator-Based Optical Frequency Combs". *Science* 332.6029 (2011), 555–559.

[111] S. Loranger, V. L. Iezzi, and R. Kashyap. "Demonstration of an ultra-high frequency picosecond pulse generator using an SBS frequency comb and self phase-locking". *Opt. Express* 20.17 (Aug. 2012), 19455–19462.

[112] A. Kobyakov, M. Sauer, and D. Chowdhury. "Stimulated Brillouin scattering in optical fibers". *Advances in Optics and Photonics* 2.1 (2010), 1–59.

[113] U. Keller, K. Weingarten, F. Kartner, D. Kopf, B. Braun, I. Jung, R. Fluck, C. Honninger, N. Matuschek, and J. A. der Au. "Semiconductor saturable absorber mirrors (SESAM's) for femtosecond to nanosecond pulse generation in solid-state lasers". *IEEE J. Sel. Topics Quantum Electron.* 2.3 (1996), 435–453.

[114] E. Ippen, C. Shank, and A. Dienes. "Passive mode locking of the cw dye laser". *Appl. Phys. Lett.* 21.8 (1972), 348–350.

[115] S. Y. Set, H. Yaguchi, Y. Tanaka, and M. Jablonski. "Laser Mode Locking Using a Saturable Absorber Incorporating Carbon Nanotubes". *J. Lightwave Technol.* 22.1 (Jan. 2004), p. 51.

[116] T. Schibli, K. Minoshima, H. Kataura, E. Itoga, N. Minami, S. Kazaoui, K. Miyashita, M. Tokumoto, and Y. Sakakibara. "Ultrashort pulse-generation by saturable absorber mirrors based on polymer-embedded carbon nanotubes". *Opt. Express* 13.20 (Oct. 2005), 8025–8031.

[117] K. Kieu and M. Mansuripur. "Femtosecond laser pulse generation with a fiber taper embedded in carbon nanotube/polymer composite". *Opt. Lett.* 32.15 (2007), 2242–2244.

[118] Z. Sun, T. Hasan, F. Torrisi, D. Popa, G. Privitera, F. Wang, F. Bonaccorso, D. M. Basko, and A. C. Ferrari. "Graphene Mode-Locked Ultrafast Laser". *ACS Nano* 4.2 (2010), 803–810.

[119] Z. Sun, T. Hasan, and A. Ferrari. "Ultrafast lasers mode-locked by nanotubes and graphene". *Physica-Section E* 44.6 (2012), p. 1082.

[120] J. N. Kutz, B. C. Collings, K. Bergman, S. Tsuda, S. T. Cundiff, W. H. Knox, P. Holmes, and M. Weinstein. "Mode-locking pulse dynamics in a fiber laser with a saturable Bragg reflector". *J. Opt. Soc. Am. B* 14.10 (Oct. 1997), 2681–2690.

[121] K. Stankov and J. Jethwa. "A new mode-locking technique using a nonlinear mirror". *Opt. Commun.* 66.1 (1988), 41–46.

[122] G. Stegeman, D. Hagan, and L. Torner. "$\chi^{(2)}$ cascading phenomena and their applications to all-optical signal processing, mode-locking, pulse compression and solitons". English. *Opt. Quant. Electron.* 28.12 (1996), 1691–1740.

[123] K. Stankov. "A mirror with an intensity-dependent reflection coefficient". English. *Appl. Phys. B* 45.3 (1988), 191–195.

[124] K. Stankov. “Mode locking by a frequency-doubling crystal: generation of transform-limited ultrashort light pulses”. *Opt. Lett.* 14.7 (Apr. 1989), 359–361.

[125] K. A. Stankov. “25 ps pulses from a Nd:YAG laser mode locked by a frequency doubling beta-BaB_2O_4 crystal”. *Appl. Phys. Lett.* 58.20 (1991), 2203–2204.

[126] Z. Lu, Q. Wu, Q. Li, and Z. Yu. “Generation of Steady-state Ultrashort Laser Pulses Based on a Novel Nonlinear Michelson Interferometer”. *J. Mod. Opt.* 40.9 (1993), 1681–1685.

[127] K. Stankov and V. Tzolov. “Nonlinear mirror based on Raman interactions”. *Appl. Phys. B* 52.2 (1991), 96–101.

[128] V Kabelka and A. Masalov. “Dispersion limitations to short pulse generation with the parametric nonlinear mirror”. *Opt. Commun.* 114.5–6 (1995), 458–462.

[129] R. DeSalvo, D. J. Hagan, M. Sheik-Bahae, G. Stegeman, E. W. V. Stryland, and H. Vanherzeele. “Self-focusing and self-defocusing by cascaded second-order effects in KTP”. *Opt. Lett.* 17.1 (Jan. 1992), 28–30.

[130] D. Pierrottet, B. Berman, M. Vannini, and D. McGraw. “Parametric lens”. *Opt. Lett.* 18.4 (Feb. 1993), 263–265.

[131] M. Zavelani-Rossi, G. Cerullo, and V. Magni. “Mode locking by cascading of second-order nonlinearities”. *IEEE J. Quantum Electron.* 34.1 (1998), 61–70.

[132] G. Cerullo, S. D. Silvestri, A. Monguzzi, D. Segala, and V. Magni. “Self-starting mode locking of a cw Nd:YAG laser using cascaded second-order nonlinearities”. *Opt. Lett.* 20.7 (Apr. 1995), 746–748.

[133] V Magni and M Zavelani-Rossi. “Nd:YVO4 laser mode locked by cascading of second order nonlinearities”. *Opt. Commun.* 152.1–3 (1998), 45–48.

[134] I. Buchvarov, S. Saltiel, C. Iglev, and K. Koynov. “Intensity dependent change of the polarization state as a result of non-linear phase shift in type II frequency doubling crystals”. *Opt. Commun.* 141.3-4 (1997), 173–179.

[135] V Couderc, F Louradour, and A Barthélémy. “2.8 ps pulses from a mode-locked diode pumped Nd:YVO4 laser using quadratic polarization switching”. *Opt. Commun.* 166.1–6 (1999), 103–111.

[136] F. Louradour, A. Mugnier, A. Albert, V. Couderc, and A. Barthelemy. "Numerical study of quadratic polarization switching mode locking applied to femtosecond pulse generation". *Opt. Commun.* 188.5–6 (2001), 333–344.

[137] D. J. Spence and R. P. Mildren. "Mode locking using stimulated Raman scattering". *Opt. Express* 15.13 (June 2007), 8170–8175.

[138] D. J. Spence, Y. Zhao, S. D. Jackson, and R. P. Mildren. "An investigation into Raman mode locking of fiber lasers". *Opt. Express* 16.8 (Apr. 2008), 5277–5289.

[139] S. Tsuda, W. H. Knox, E. A. de Souza, W. Y. Jan, and J. E. Cunningham. "Low-loss intracavity AlAs/AlGaAs saturable Bragg reflector for femtosecond mode locking in solid-state lasers". *Opt. Lett.* 20.12 (June 1995), 1406–1408.

[140] O. E. Martinez, R. L. Fork, and J. P. Gordon. "Theory of passively mode-locked lasers including self-phase modulation and group-velocity dispersion". *Opt. Lett.* 9.5 (May 1984), 156–158.

[141] R. L. Fork, O. E. Martinez, and J. P. Gordon. "Negative dispersion using pairs of prisms". *Opt. Lett.* 9.5 (May 1984), 150–152.

[142] H. A. Haus, J. G. Fujimoto, and E. P. Ippen. "Structures for additive pulse mode locking". *J. Opt. Soc. Am. B* 8.10 (Oct. 1991), 2068–2076.

[143] S. Kelly. "Characteristic sideband instability of periodically amplified average soliton". *Electron. Lett.* 28.8 (1992), 806–807.

[144] L. M. Zhao, D. Y. Tang, and J. Wu. "Gain-guided soliton in a positive group-dispersion fiber laser". *Opt. Lett.* 31.12 (June 2006), 1788–1790.

[145] L. M. Zhao, D. Y. Tang, H. Zhang, T. H. Cheng, H. Y. Tam, and C. Lu. "Dynamics of gain-guided solitons in an all-normal-dispersion fiber laser". *Opt. Lett.* 32.13 (July 2007), 1806–1808.

[146] D. Anderson, M. Desaix, M. Karlsson, M. Lisak, and M. L. Quiroga-Teixeiro. "Wave-breaking-free pulses in nonlinear-optical fibers". *J. Opt. Soc. Am. B* 10.7 (July 1993), 1185–1190.

[147] J. Dudley, A. Peacock, V. Kruglov, B. Thomsen, J. Harvey, M. Fermann, G. Sucha, and D. Harter. "Generation and interaction of parabolic pulses in high gain fiber amplifiers and oscillators". In: *Optical Fiber Communication Conference and International Conference on Quantum Information*. Optical Society of America, 2001, WP4.

[148] F. O. Ilday, J. R. Buckley, W. G. Clark, and F. W. Wise. "Self-Similar Evolution of Parabolic Pulses in a Laser". *Phys. Rev. Lett.* 92 (21 May 2004), p. 213902.

[149] S. Pitois, C. Finot, L. Provost, and D. Richardson. "Generation of localized pulses from incoherent wave in optical fiber lines made of concatenated Mamyshev regenerators". *J. Opt. Soc. Am. B* 25.9 (2008), 1537–1547.

[150] D. Y. Tang, L. M. Zhao, B. Zhao, and A. Q. Liu. "Mechanism of multisoliton formation and soliton energy quantization in passively mode-locked fiber lasers". *Phys. Rev. A* 72 (4 Oct. 2005), p. 043816.

[151] L. M. Zhao, D. Y. Tang, J. Wu, X. Q. Fu, and S. C. Wen. "Noise-like pulse in a gain-guided soliton fiber laser". *Opt. Express* 15.5 (Mar. 2007), 2145–2150.

[152] P. Mamyshev. "All-optical data regeneration based on self-phase modulation effect". In: *Optical Communication, 1998. 24th European Conference on*. Vol. 1. IEEE. 1998, 475–476.

[153] M. Rochette, L. Fu, V. Ta"eed, D. Moss, and B. Eggleton. "2R optical regeneration: an all-optical solution for BER improvement". *IEEE J. Sel. Topics Quantum Electron.* 12.4 (2006), 736–744.

[154] L. Fu, M. Rochette, V. Ta'eed, D. Moss, and B. Eggleton. "Investigation of self-phase modulation based optical regeneration in single mode As2Se3 chalcogenide glass fiber". *Opt. Express* 13.19 (2005), 7637–7644.

[155] A. Striegler and B. Schmauss. "Analysis and optimization of SPM-based 2R signal regeneration at 40 gb/s". *IEEE/OSA J. Lightw. Technol.* 24.7 (2006), 2835–2843.

[156] L. A. Provost, C. Finot, P. Petropoulos, K. Mukasa, and D. J. Richardson. "Design scaling rules for 2R-optical self-phase modulation-based regenerators". *Opt. Express* 15.8 (Apr. 2007), 5100–5113.

[157] P. Baveja, D. Maywar, and G. Agrawal. "Optimization of All-Optical 2R Regenerators Operating at 40 Gb/s: Role of Dispersion". *IEEE/OSA J. Lightw. Technol.* 27.17 (Sept. 2009), 3831–3836.

[158] S. Pitois, C. Finot, and L. Provost. "Asymptotic properties of incoherent waves propagating in an all-optical regenerators line". *Opt. Lett.* 32.22 (2007), 3263–3265.

[159] M. Hercher. "Single-mode operation of a Q-Switched ruby laser". *Appl. Phys. Lett.* 7.2 (1965), 39–41.

[160] A. J. DeMaria, D. A. Stetser, and H. Heynau. "Self mode-locking of lasers with saturable absorbers". *Appl. Phys. Lett.* 8.7 (1966), 174–176.

[161] K. Sala, M. Richardson, and N. R. Isenor. "Passive mode locking of lasers with the optical Kerr effect modulator". *IEEE J. Quantum Electron.* 13.11 (1977), 915–924.

[162] Y. Silberberg, P. W. Smith, D. J. Eilenberger, D. A. B. Miller, A. C. Gossard, and W. Wiegmann. "Passive mode locking of a semiconductor diode laser". *Opt. Lett.* 9.11 (Nov. 1984), 507–509.

[163] N. Whitaker, H. Houh, H. Avramopoulos, and T. F. Morse. "All-optical Phase-locked Oscillator". In: *Lasers and Electro-Optics Society Annual Meeting, 1990. LEOS '90. Conference Proceedings., IEEE.* 1990, 93–95.

[164] I. I. N. Duling. "All-fiber ring soliton laser mode locked with a nonlinear mirror". *Opt. Lett.* 16.8 (Apr. 1991), 539–541.

[165] V. Matsas, T. Newson, and M. Zervas. "Self-starting passively mode-locked fibre ring laser exploiting nonlinear polarisation switching". *Opt. Commun.* 92.1-3 (1992), 61–66.

[166] G. Cerullo, M. B. Danailov, S. D. Silvestri, P. Laporta, V. Magni, D. Segala, and S. Taccheo. "A diode-pumped nonlinear mirror mode-locked Nd:YAG laser". *Appl. Phys. Lett.* 65.19 (1994), 2392–2394.

[167] J. Hult. "A fourth-order Runge–Kutta in the interaction picture method for simulating supercontinuum generation in optical fibers". *J. Lightwave Technol.* 25.12 (2007), 3770–3775.

[168] I. A. Yarutkina, O. V. Shtyrina, M. P. Fedoruk, and S. K. Turitsyn. "Numerical modeling of fiber lasers with long and ultra-long ring cavity". *Opt. Express* 21.10 (May 2013), 12942–12950.

[169] R. Caplan. “NLSEmagic: Nonlinear Schrödinger equation multi-dimensional Matlab-based GPU-accelerated integrators using compact high-order schemes”. *Comput. Phys. Commun.* 184.4 (2013), 1250–1271.

[170] H. Bauke and C. H. Keitel. “Accelerating the Fourier split operator method via graphics processing units”. *Comput. Phys. Commun.* 182.12 (2011), 2454–2463.

[171] S. Hellerbrand and N. Hanik. “Fast Implementation of the Split-Step Fourier Method Using a Graphics Processing Unit”. In: *Optical Fiber Communication Conference*. Optical Society of America, 2010, OTuD7.

[172] M. Baregheh, V. Mezentsev, and H. Schmitz. “Multi-threaded Parallel Numerical Modelling of Femtosecond Pulse propagation in Laser Machining”. In: *CLEO/Europe and EQEC 2011 Conference Digest*. Optical Society of America, 2011, CF_P1.

[173] A. A. Amorim, M. V. Tognetti, P. Oliveira, J. L. Silva, L. M. Bernardo, F. X. Kärtner, and H. M. Crespo. “Sub-two-cycle pulses by soliton self-compression in highly nonlinear photonic crystal fibers”. *Opt. Lett.* 34.24 (Dec. 2009), 3851–3853.

[174] B. Opanchuk. “Reikna, the pure Python GPGPU library”. http://reikna.publicfields.net/.

[175] A. Klöckner, N. Pinto, Y. Lee, B. Catanzaro, P. Ivanov, and A. Fasih. “PyCUDA and PyOpenCL: A scripting-based approach to GPU run-time code generation”. *Parallel Comput.* 38.3 (2012), 157–174.

[176] F. Alted, I. Vilata, S. Prater, V. Mas, T. Hedley, et al. *PyTables: Hierarchical Datasets in Python*. 2002.

[177] S. van der Walt, S. Colbert, and G. Varoquaux. “The NumPy Array: A Structure for Efficient Numerical Computation”. *Computing in Science Engineering* 13.2 (2011), 22–30.

[178] P. Peterson. “F2PY: a tool for connecting Fortran and Python programs”. *Int. J. Comput. Sci. Eng.* 4.4 (2009), 296–305.

[179] F. Pérez and B. E. Granger. “IPython: a System for Interactive Scientific Computing”. *Comput. Sci. Eng.* 9.3 (May 2007), 21–29.

[180] A. Heidt. “Efficient Adaptive Step Size Method for the Simulation of Supercontinuum Generation in Optical Fibers”. *IEEE/OSA J. Lightw. Technol.* 27.18 (Sept. 2009), 3984–3991.

[181] The HDF Group. "Hierarchical data format version 5, 2000-2010".

[182] M. Frigo and S. Johnson. "The Design and Implementation of FFTW3". *Proc. IEEE* 93.2 (2005), 216–231.

[183] F. Alted. "Why Modern CPUs Are Starving and What Can Be Done about It". *Computing in Science Engineering* 12.2 (2010), 68–71.

[184] R. Tarjan. "Depth-First Search and Linear Graph Algorithms". *SIAM J. Comput.* 1.2 (1972), 146–160.

[185] T.-H. Her, G. Raybon, and C. Headley. "Optimization of pulse regeneration at 40 Gb/s based on spectral filtering of self-phase modulation in fiber". *IEEE Photon. Technol. Lett.* 16.1 (2004), 200–202.

[186] W. J. Tomlinson, R. H. Stolen, and C. V. Shank. "Compression of optical pulses chirped by self-phase modulation in fibers". *J. Opt. Soc. Am. B* 1.2 (Apr. 1984), 139–149.

[187] A. Siegman. *Lasers*. Univ. Science Books, 1986.

[188] F. Harris. "On the use of windows for harmonic analysis with the discrete Fourier transform". *Proc. IEEE* 66.1 (Jan. 1978), 51–83.

[189] S. Ghafoor and P. Petropoulos. "Effect of dispersion slope of highly nonlinear fibre on the performance of Self Phase Modulation based 2R-optical regenerator". In: *Computer Technology and Development (ICCTD), 2010 2nd International Conference on*. 2010, 144–148.

[190] J. Nicholson, A. Abeeluck, C. Headley, M. Yan, and C. Jørgensen. "Pulsed and continuous-wave supercontinuum generation in highly nonlinear, dispersion-shifted fibers". English. *Appl. Phys. B* 77.2-3 (2003), 211–218.

[191] Y. Takushima. "High average power, depolarized super-continuum generation using a 1.55-μm ASE noise source". *Opt. Express* 13.15 (July 2005), 5871–5877.

[192] J. Hernandez-Garcia, O. Pottiez, J. Estudillo-Ayala, and R. Rojas-Laguna. "Numerical analysis of a broadband spectrum generated in a standard fiber by noise-like pulses from a passively mode-locked fiber laser". *Opt. Commun.* 285.7 (2012), 1915–1919.

[193] K. Tai, A. Hasegawa, and N. Bekki. "Fission of optical solitons induced by stimulated Raman effect". *Opt. Lett.* 13.5 (1988), 392–394.

[194] J. Lee, Y. Takushima, and K. Kikuchi. "Continuous-wave supercontinuum laser based on an erbium-doped fiber ring cavity incorporating a highly nonlinear optical fiber". *Opt. Lett.* 30.19 (2005), 2599–2601.

[195] S. Chi and S. Wen. "Raman cross talk of soliton collision in a lossless fiber". *Opt. Lett.* 14.21 (Nov. 1989), 1216–1218.

[196] M. N. Islam, G. Sucha, I. Bar-Joseph, M. Wegener, J. P. Gordon, and D. S. Chemla. "Femtosecond distributed soliton spectrum in fibers". *J. Opt. Soc. Am. B* 6.6 (June 1989), 1149–1158.

[197] M. H. Frosz, O. Bang, and A. Bjarklev. "Soliton collision and Raman gain regimes in continuous-wave pumped supercontinuum generation". *Opt. Express* 14.20 (Oct. 2006), 9391–9407.

[198] J. M. Dudley, G. Genty, and S. Coen. "Supercontinuum generation in photonic crystal fiber". *Rev. Mod. Phys.* 78 (4 Oct. 2006), 1135–1184.

[199] D. Solli, C Ropers, P Koonath, and B Jalali. "Optical rogue waves". *Nature* 450.7172 (2007), 1054–1057.

[200] V. Matsas, T. Newson, D. Richardson, and D. Payne. "Selfstarting passively mode-locked fibre ring soliton laser exploiting nonlinear polarisation rotation". *Electron. Lett.* 28.15 (1992), 1391–1393.

[201] L. Nelson, D. Jones, K. Tamura, H. Haus, and E. Ippen. "Ultrashort-pulse fiber ring lasers". *Appl. Phys. B: Lasers Opt.* 65.2 (1997), 277–294.

[202] M. Dennis and I. I. Duling. "Experimental study of sideband generation in femtosecond fiber lasers". *IEEE J. Quantum Electron.* 30.6 (1994), 1469–1477.

[203] H. Haus, E. Ippen, and K. Tamura. "Additive-pulse modelocking in fiber lasers". *IEEE J. Quantum Electron.* 30.1 (1994), 200–208.

[204] G. Sucha, D. Chemla, and S. Bolton. "Effects of cavity topology on the nonlinear dynamics of additive-pulse mode-locked lasers". *J. Opt. Soc. Am. B* 15.12 (1998), 2847–2853.

[205] S. Kobtsev, S. Kukarin, S. Smirnov, S. Turitsyn, and A. Latkin. "Generation of double-scale femto/pico-second optical lumps in mode-locked fiber lasers". *Opt. Express* 17.23 (2009), 20707–20713.

[206] S. Kobtsev, S. Kukarin, and Y. Fedotov. "Ultra-low repetition rate mode-locked fiber laser with high-energy pulses". *Opt. Express* 16.26 (Dec. 2008), 21936–21941.

[207] N Akhmediev, J. M. Dudley, D. R. Solli, and S. K. Turitsyn. "Recent progress in investigating optical rogue waves". *J. Opt.* 15.6 (2013), p. 060201.

[208] J. M. Soto-Crespo, P. Grelu, and N. Akhmediev. "Dissipative rogue waves: Extreme pulses generated by passively mode-locked lasers". *Phys. Rev. E* 84 (1 July 2011), p. 016604.

[209] A. Zaviyalov, O. Egorov, R. Iliew, and F. Lederer. "Rogue waves in mode-locked fiber lasers". *Phys. Rev. A* 85 (1 Jan. 2012), p. 013828.

[210] C. Lecaplain, P. Grelu, J. M. Soto-Crespo, and N. Akhmediev. "Dissipative Rogue Waves Generated by Chaotic Pulse Bunching in a Mode-Locked Laser". *Phys. Rev. Lett.* 108 (23 June 2012), p. 233901.

[211] J. Kang. "Broadband quasi-stationary pulses in mode-locked fiber ring laser". *Opt. Commun.* 182.4-6 (2000), 433–436.

[212] Y. Takushima, K. Yasunaka, Y. Ozeki, and K. Kikuchi. "87 nm bandwidth noise-like pulse generation from erbium-doped fibre laser". *Electron. Lett.* 41.7 (Mar. 2005), 399–400.

[213] D. Tang, L. Zhao, and B. Zhao. "Soliton collapse and bunched noise-like pulse generation in a passively mode-locked fiber ring laser". *Opt. Express* 13.7 (Apr. 2005), 2289–2294.

[214] L. Zhao and D. Tang. "Generation of 15-nJ bunched noise-like pulses with 93-nm bandwidth in an erbium-doped fiber ring laser". *Appl. Phys. B* 83.4 (2006), p. 553.

[215] L. Zhao, D. Tang, T. Cheng, H. Tam, and C. Lu. "120 nm Bandwidth noise-like pulse generation in an erbium-doped fiber laser". *Opt. Commun.* 281.1 (2008), 157–161.

[216] D. Lei, H. Yang, H. Dong, S. Wen, H. Xu, and J. Zhang. "Effect of birefringence on the bandwidth of noise-like pulse in an erbium-doped fiber laser". *J. Mod. Opt.* 56.4 (2009), 572–576.

[217] O. Pottiez, R. Grajales-Coutiño, B. Ibarra-Escamilla, E. A. Kuzin, and J. C. Hernández-García. "Adjustable noiselike pulses from a figure-eight fiber laser". *Appl. Opt.* 50.25 (Sept. 2011), E24–E31.

[218] A. Boucon, B. Barviau, J. Fatome, C. Finot, T. Sylvestre, M. Lee, P. Grelu, and G. Millot. "Noise-like pulses generated at high harmonics in a partially-mode-locked km-long Raman fiber laser". *Appl. Phys. B: Lasers Opt.* 106 (2 2012), 283–287.

[219] M. Horowitz and Y. Silberberg. "Control of noiselike pulse generation in erbium-doped fiber lasers". *IEEE Photon. Technol. Lett.* 10.10 (Oct. 1998), 1389–1391.

[220] S. Keren, E. Brand, Y. Levi, B. Levit, and M. Horowitz. "Data storage in optical fibers and reconstruction by use of low-coherence spectral interferometry". *Opt. Lett.* 27.2 (Jan. 2002), 125–127.

[221] V. Goloborodko, S. Keren, A. Rosenthal, B. Levit, and M. Horowitz. "Measuring Temperature Profiles in High-Power Optical Fiber Components". *Appl. Opt.* 42.13 (May 2003), 2284–2288.

[222] S. Keren and M. Horowitz. "Interrogation of fiber gratings by use of low-coherence spectral interferometry of noiselike pulses". *Opt. Lett.* 26.6 (Mar. 2001), 328–330.

[223] S. Keren, A. Rosenthal, and M. Horowitz. "Measuring the structure of highly reflecting fiber Bragg gratings". *IEEE Photon. Technol. Lett.* 15.4 (Apr. 2003), 575–577.

[224] T. Schweizer, B. Samson, R. Moore, D. Hewak, and D. Payne. "Rare-earth doped chalcogenide glass fibre laser". *Electron. Lett.* 33.5 (1997), 414–416.

[225] J. Sanghera, L. B. Shaw, and I. Aggarwal. "Chalcogenide glass-fiber-based mid-IR sources and applications". *IEEE J. Sel. Topics Quantum Electron.* 15.1 (2009), 114–119.

[226] S. Mirov, V. Fedorov, I. Moskalev, D. Martyshkin, and C. Kim. "Progress in Cr2+ and Fe2+ doped mid-IR laser materials". *Laser & Photonics Reviews* 4.1 (2010), 21–41.

[227] H. Haus, K. Tamura, L. Nelson, and E. Ippen. "Stretched-pulse additive pulse mode-locking in fiber ring lasers: theory and experiment". *IEEE J. Quantum Electron.* 31.3 (1995), 591–598.

[228] M. E. Fermann, M. J. Andrejco, M. L. Stock, Y. Silberberg, and A. M. Weiner. "Passive mode locking in erbium fiber lasers with negative group delay". *Appl. Phys. Lett.* 62.9 (1993), 910–912.

[229] C. Xiong, E. Magi, F. Luan, A. Tuniz, S. Dekker, J. Sanghera, L. Shaw, I. Aggarwal, and B. Eggleton. "Characterization of picosecond pulse nonlinear propagation in chalcogenide As_2S_3 fiber". *Appl. Opt.* 48.29 (2009), 5467–5474.

[230] H.-T. Shang. “Chromatic dispersion measurement by white-light interferometry on metre-length single-mode optical fibres”. *Electron. Lett.* 17.17 (Nov. 1981), 603–605.

[231] J. Lee and D. Kim. “Versatile chromatic dispersion measurement of a single mode fiber using spectral white light interferometry”. *Opt. Express* 14.24 (2006), 11608–11615.